Automated Aboveground Carbon Estimation of Forests with Remote Sensing

by

Piper Gordon
BSEng, University of Victoria, 2010

A Thesis Submitted in Partial Fulfillment
of the Requirements for the Degree of

MASTER OF SCIENCE

in the Department of Computer Science

Supervisory Committee

Automated Aboveground Carbon Estimation of Forests with Remote Sensing

by

Piper Gordon
BSEng, University of Victoria, 2010

Supervisory Committee

Dr. David G. Goodenough, (Department of Computer Science)
Co-Supervisor

Dr. Wendy Myrvold, (Department of Computer Science)
Co-Supervisor

Dr. K. Olaf Niemann, (Department of Geography)
Outside Member

Abstract

Supervisory Committee
Dr. David G. Goodenough, (Department of Computer Science)
Co-Supervisor
Dr. Wendy Myrvold, (Department of Computer Science)
Co-Supervisor
Dr. K. Olaf Niemann, (Department of Geography)
Outside Member

Canada's forests are believed to contain 86 gigatons of carbon, stored above and below ground [1]. These forests are large in area, making them difficult to monitor using conventional means [1]. Understanding the carbon cycle and the role of forests as carbon sinks is crucial in the investigation and mitigation of climate change to address national obligations [2]. One economical solution for monitoring the carbon content of Canada's forests is the development of an automated computer system which uses multisource remotely sensed data to estimate the aboveground carbon of trees. The process involves data fusion of remotely sensed hyperspectral data for tree species information and lidar (light detection and ranging) and radar (radio detection and ranging) for tree height. The size and dimensionality of the data necessitate the efficient use of computing resources for analysis. The outcome is a useful carbon measuring system. The three research questions are: (1) How do we map with remote sensing aboveground carbon in the forests? (2) How do we determine the accuracies of these aboveground carbon maps? (3) How can an automated system be designed for creating aboveground carbon maps?

Table of Contents

List of Tables

List of Figures

Glossary

AFT – (Advanced Forest Technologies) a research group at the Pacific Forestry Centre of Natural Resources Canada.

AISA – (Airborne imaging spectrometer for applications) For the purposes of this report AISA refers to the AISA Dual hyperspectral sensor manufactured by Specim owned by UVic, mounted on a Terra Remote Sensing aircraft [3]. The images taken with this sensor were originally 2x2m spatial resolution. There are a total of 492 bands ranging from 395.16nm to 2503.09nm.

bands – a band can represent a small or large range of wavelengths. Hyperspectral sensors sample narrow bands spectrally at certain intervals (every 10nm, for example). The values for each of the hundreds of bands form a smooth spectrum for any given physical location.

Bidirectional Reflectance Distribution Function – (BRDF) Describes the phenomenon that the same objects will appear differently when images are taken with different view angles and with different illumination angles. BRDF equations are used to correct for these effects; they give reflectance based on the viewing and illumination geometry. Properties of the target object affect BRDF, as does the wavelength of light [4, 5].

CHM – (Canopy Height Model) a height image for the distance from the ground to the forest canopy.

Current Foliage – new foliage grown within the current year

DBH – (Diameter at Breast Height) the measurement of tree diameter at 1.3m from the ground.

ENVI – (Environment for Visualizing Images) a software package based on IDL tools. ENVI is equipped with a host of useful functions for processing hyperspectral imagery. ENVI is made and marketed by Exelis (www.exelisvis.com/envi/).

Flightlines – hyperspectral data from a single pass over an area with a sensor. Aircraft pass over target areas in a linear path with a sensor. The imagery taken when the aircraft is turning is usually not used. The adjacent, semi-straight paths between the turns form an image of the area, usually overlapping each other on their edges. These are the flightlines.

Geocorrection – the process by which data collected by an aircraft is fit to geographic coordinates of the ground, taking into account the pitch, roll and yaw of the craft [6].

Hyperspectral – Over 20 bands of spectral data: often hundreds of bands. Hyperspectral sensing is also referred to as imaging spectroscopy.

Interleave: Band Interleaved by Pixel, Band Sequential, Band Interleaved by Line – (BIP, BSQ, and BIL). These are the three formats which order data differently. The format of the file is important to consider when performing operations within an IDL program. The data can be ordered sequentially by band (each pixel in the first band then onto the second band), by pixel (for the first pixel each band's value is given, then for the second pixel, etc.) and by line (for each row of the data, the first band's values are given, then the second and so on).

IDL – (interactive data language) The language upon which ENVI is based. It is similar to C.

Lidar – (Light Detection and Ranging) is an active optical remote sensing technology that illuminates a target with a laser and then measures properties of the reflected light to find range or other information of a distant target.

Mask – a binary image the same spatial size as the image it 'masks'. Each pixel is either on or off (1 or 0). When applied to a file a mask blocks out the information behind the off pixels (sets their value to zero).

Mosaic (mosaicking) – from the 'Mosaic' widget in ENVI, when two or more image files are joined to make a new file which includes both of their data. For the purposes of this paper, mosaicking is always done with georeferencing, so the imagery aligns properly to show where it is relative to the other data. For example, the flightlines over an area can be mosaicked to form a picture of the entire area covered by the sensor.

MNF – (Minimum Noise Fraction) a method for removing noise from multi-dimensional image data, implemented in ENVI.

Multispectral – An optical sensor with usually fewer than 15 bands of data.

NIR – (Near Infrared) in this thesis describes light with wavelengths from 750nm to 1100nm.

Non-Current foliage – foliage more than a year old.

Oven-dry – The process through which biomass is dried, at 100º C until there is no significant change in mass due to water evaporation [7].

P value – The p value is the probability that additional observations will be at least as extreme as previous ones if the null hypothesis is true (for example, if there is no relationship between measurements)[8]. Typically, if the p-value is less than 0.05 it is considered an indicator of statistical significance and the null hypothesis is rejected [8].

PLS – (Partial Least Squares) A statistical technique which is routinely used for classification and discrimination, though it was not designed for those purposes [9]. Unlike least squares regression which measures errors as the squared distance from the

data points to the predictive function, PLS regression projects the observed and predicted variables into a new space and finds the direction in the X space that explains the maximum variance direction in the Y space [10]. For the forestry applications described, PLS regression finds a set of factors between measured spectral data and corresponding ground measurements. These factors are used to predict ground properties from spectral data.

R or Pearson coefficient or correlation coefficient – A value between -1 and 1, inclusive, which describes the strength of the linear relationship of two quantitative attributes of a data set (X and Y) and the direction, where negative numbers indicate an inverse relationship. An r value of 0 means that there is no linear relationship between the variables and a value of 1 or -1 means that all sample points lie on a straight line when graphed with the axes X and Y: for any Y value, the X value can be predicted perfectly and vice versa [11]. The calculation of r follows in equation 1 [12].

$$\mathrm{R} = \frac{\sum_{i=1}^{n} (X_i - \overline{X})(Y_i - \overline{Y})}{\sqrt{\sum_{i=1}^{n} (X_i - \overline{X}) \sum_{i=1}^{n} (Y_i - \overline{Y})}}. \quad (1)$$

where X and Y are attributes, X_i and Y_i are measurements of their respective attributes, and $\overline{X}$ and $\overline{Y}$ are the mean values for each attribute.

R^2 or coefficient of determination – The squared correlation coefficient (a value between 0 and 1, inclusive) gives the proportion of common variance between two variables, X and Y [13]. The coefficient of determination can be calculated for a best fit

line through a set of sample points to give the proportion of variability explained by the model [14].

Radar – (Radio Detection and Ranging) Here radar refers to an active sensor which measures the echoes of signals, typically in the wavelength range from 1cm to 1 m; these measurements describe geometric and dielectric properties of the target as well as its ability to depolarize radar waves, if polarized radar is used [15].

RSEng – (Remote Sensing Software Engineering) A group in the Computer Science Department at the University of Victoria concerned with the field of remote sensing. It is one of the Department of Computer Science faculty groups, under the umbrella of the Software Engineering and Systems research group.

SAR – (Synthetic aperture radar) SAR is the use of relative velocity measurement of the aircraft or spacecraft platform to achieve high resolution radar as if with a very large antennae [15]. Conventional SAR gives the location of a target with respect to the flight track direction (along the path of the platform) and the cross track direction (the distance from the SAR to the target). [16]

Scenes – parts of a flightline, cut to select the hyperspectral data in smaller more manageable pieces.

SDM – (Stem Density Model) A map showing or data describing the number of tree stems per area, often in stems per hectare.

Specific gravity – The ratio of the density of a material compared to that of water (for liquids and solids) or air (for gases).

SWIR - (Short Wave Infrared) the region in the electromagnetic spectrum from 900nm to 2500nm.

Acknowledgments

I would like to acknowledge my supervisor, Dr. David Goodenough for all of his help and mentorship. I am much obliged to my co-supervisor Dr. Wendy Myrvold and to Dr. K. Olaf Niemann: thank you for being on my committee. I would also like to thank the staff and faculty of the University of Victoria (UVic), and the staff at the Pacific Forestry Centre (PFC), where I conducted much of my research.

The help of co-op work student, Thomas Ziebarth, from January through April must be acknowledged. He ran many, many classifications for Figure 19 and 20, and processed countless biomass maps as we were refining the process.

Computer programs and scripts written by Ash Richardson, Tian Han and Geordie Hobart were used in the process and some were integrated into the system.

This research would not have been possible without hyperspectral and lidar data from the Department of Geography at UVic, and hyperspectral data from the National Aeronautics and Space Administration (NASA), over the study areas. Field work was performed and analysed by the PFC employees and students and faculty of UVic. The Capital Regional District (CRD) of Victoria provided forest information and high spatial resolution photographs for the Greater Victoria Watershed District.

Finally, I express my gratitude to all of the scientists, mathematicians, physicists, engineers and silviculturists who have improved remote sensing techniques for forest management and greatly helped my understanding of these concepts through their publications.

Dedication

I dedicate this work to my family.

1 Introduction

1.1 Trees and Carbon

Photosynthesis is the process through which trees convert carbon dioxide, water and sunlight into oxygen and the sugar they use to grow, described by this equation 2 [17]:

$$CO_2 + 2H_2O + \text{light energy} = CH_2O + O_2 + H_2O \quad (2)$$

where CH_2O is a carbohydrate.

When consumed by a tree, the carbon from the CO_2 is stored in the biomass of the tree until the tree decays or is burned. Plants also respire which releases carbon dioxide back into the atmosphere; half of the carbon dioxide that plants acquire each year is lost in respiration. Still, hundreds of gigatons of carbon are stored in the biomass of plants and trees, and thousands of gigatons are stored in the soil with help from plants and trees [18]. See Figure 1 for a diagram of the fast carbon cycle. Roughly half of the oven-dried biomass of a living tree is carbon [1, 19, 20]. Thus, forests can be a significant carbon sink and carbon store.

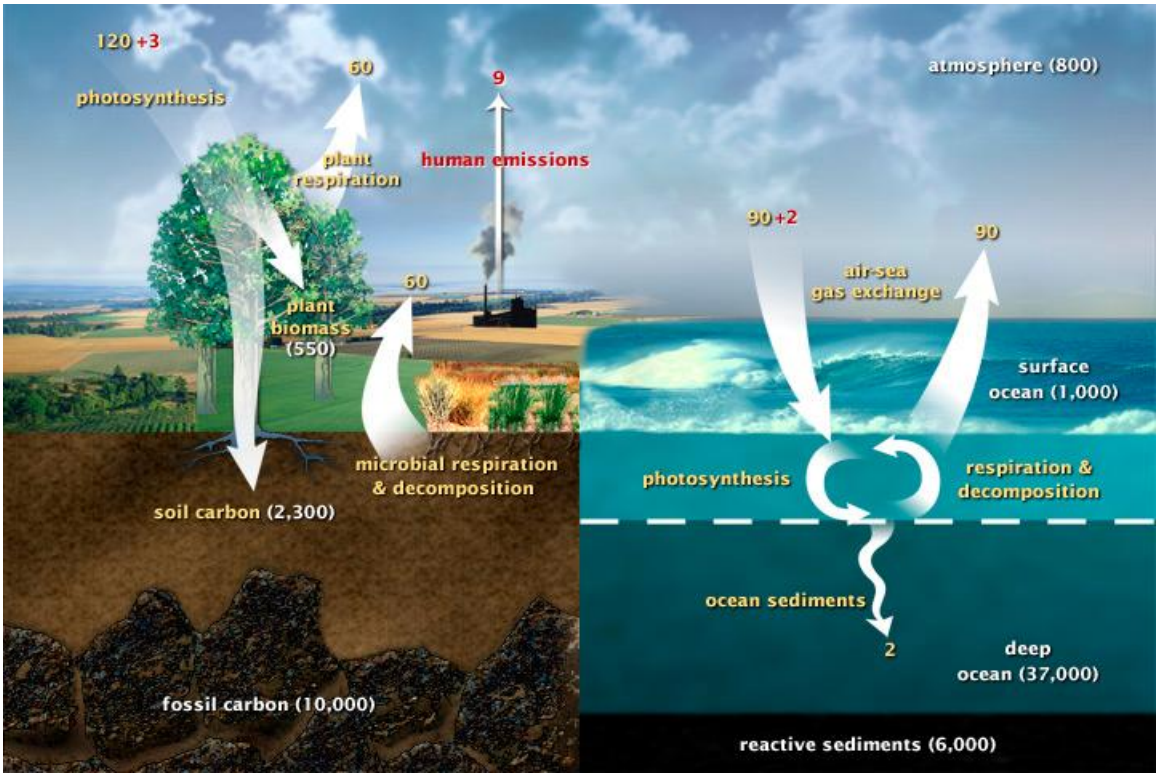

Figure 1: The fast carbon cycle. Natural fluxes of carbon are in yellow, stored carbon in white and human contributions are in red. All numbers are gigatons of carbon per year [18].

While our understanding of the forests' involvement in the carbon cycle and climate change is not complete, it is known to be important [21, 22]. From year to year more research is published to support forests as a carbon sink and deforestation as a carbon source which contributes to the volume of greenhouse gasses in the atmosphere and climate change. Recent analysis of forest data from 1990 to 2007, led to an estimate of a net global forest sink of 1.1 ± 0.8 gigatons (or petagrams) of carbon per year [23]. Current effects of climate change include the acidification of the oceans as they absorb surplus carbon from the atmosphere [24] and the loss of habitat for species as their environment shifts faster than they can adapt [25].

Atmospheric carbon dioxide in the atmosphere (CO_2) was measured at 385 parts per million (ppm) in 2008 and "is rising fast" [26]. Carbon dioxide concentrations in late 2011 are higher than at any time in the past 650,000 years [27]. The volume of CO_2, a greenhouse gas (GHG), entering the atmosphere has increased by 25% over the last century [28]. Even small amounts of GHG have a profound effect on Earth's temperature: without the greenhouse effect, Earth's mean temperature would be -18˚ C, instead of 15˚ C [27].

Strategies for mitigation of climate change include planting trees specifically for carbon sequestration [29] or using mechanical artificial trees to do the same [30, 31]. There is literature comparing the carbon storing capabilities across tree ages and species [32, 33] and on the most suitable trees to plant for urban carbon capture [34-36]. New trees can sequester considerable carbon as they grow, but the vast carbon storage of old, established forest stands cannot be ignored [33]. Forest management, on a national and global scale, must be well informed and have access to all the tools necessary to ensuring a continued net carbon sink.

For Canada and certainly for the world, the volume of forest data gathered from satellites alone is far too great for manual inspection. Intelligent computer systems must be enlisted to assist in forest management. Hundreds of algorithms exist for automated detection [37], clustering [38], identification [39, 40], classification, and analysis [158]. As research in pattern recognition continues, better classification algorithms are developed for particular purposes. For example, a method was recently developed to discriminate the native Hawaiian Acacia koa tree from other vegetation [41]. Utilizing these algorithms, tools have been formulated to estimate vegetation cover and biomass.

1.2 Remote Sensing Sensors and Products

Remote sensing, the collection of information about a subject without direct contact with that subject, is ideal for acquiring chemistry and height information from large and inaccessible forests without extensive field work. Reflected radiation with various wavelength ranges along the electromagnetic spectrum is useful for extracting forest information: VNIR (visible and near infrared) from 400nm to 900nm and SWIR (short wave infrared) from 900nm to 2500nm [42] for chemistry, blasts of non-visible light (1060nm) for a height reading with lidar, and radar with 1 cm to longer wavelengths (68 cm) for forest structure information.

Types of sensors include lidar, radar, synthetic aperture radar (SAR), multispectral and hyperspectral. As mentioned above, lidar measures height with pulses of radiation. Types of lidar will be described in section 2.3.

Radar sensing systems emit radiation at a specific wavelength, sideways and down to the target surface, as opposed to straight down (nadir); radio wavelengths can penetrate dense clouds, and because radar is an active sensor, it can operate during the day or at night. Precipitation and storms can degrade the quality of radar imaging: obscuring echoes and attenuation due to rain drop size and total liquid water content, respectively, are both inversely related to wavelength [15]. The system measures the response from the waves after they have reflected off of the target (the backscatter). The intensity of the echoes, shown in the brightness of the image, is proportional to the target's geometry (surface roughness relative to the radar's wavelength and angle compared to the radar signal incidence angle, for example) and how it absorbs and dissipates the signal, which is strongly related to conductivity and thus moisture content [15, 43]. Radar signals can be polarized to further discriminate between ground cover types, as most surfaces tend to

depolarize the wave, to different degrees [15]. Usually linear polarization for horizontal and vertical electric fields, or circular polarization, is used [44]. Polarization is done by orienting the electric field with respect to the antenna. When the electric field is perpendicular to the direction of flight, the electric field and the signal are vertically linear polarized and for parallel polarization would have to be received with an antenna in the same direction [44]. Radar systems may transmit and receive one or both types of polarized waves, in any combination [15].

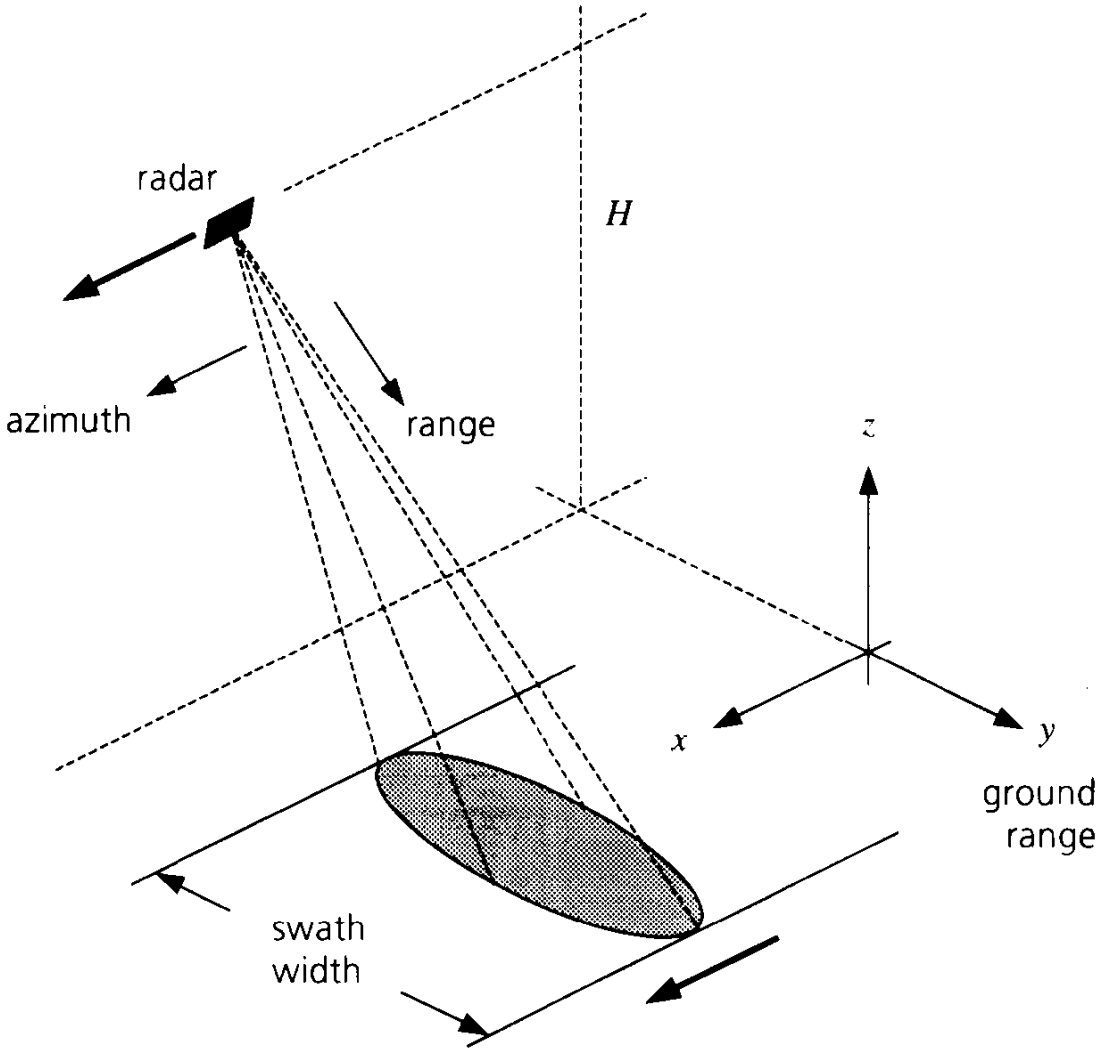

Figure 2: Side-looking radar imaging geometry [43]. There is H, the altitude of the radar, in the z direction and azimuth (the flight direction) is the same as x.

The radar-carrying platform moves forward (the azimuth direction [43]) far more slowly than the range scanning is performed (at close to light speed), wherein radar pulses are transmitted and the reflections are received [45]. The result is a two dimensional image (range and azimuth) of the radar brightness of the ground. See Figure 2 for a diagram of radar geometry.

SAR is radar which emits multiple waves timed with the movement of the platform to synthesize a very large receiving antenna: one which would be impractical or impossible as a payload for an aircraft or satellite [15, 43, 45]. As the radar moves, the response signals are stored in an array in memory. Then a processor uses signal processing algorithms to synthesize the effects of a physical antenna from the virtual data [45]. The waves must be phase-coherent [45], which allows for Doppler estimation and the ability to differentiate small differences in velocity [46]. Resolution (the minimum separation between two side-by-side targets such that they appear discretely) of SAR is approximately half of the antenna length [43, 45]. The backscatters of the objects (or reflectors) in each pixel area sum up coherently for the brightness of that pixel; however, the individual facets of many distributed reflectors can cause mutual interference of the coherent radar signals [45]. This leads to ‘speckle’ effects which can be reduced by averaging [16, 43, 45, 47].

Passive sensors rely on the sun or their target for illumination [15]. Solar radiation is reflected by matter on the ground and is collected by the sensor and measured at varying wavelengths. At certain wavelengths the light and the particles of matter interact, changing the reflectance. This phenomenon allows scientists or computer programs to

distinguish different ground cover types. All of the reflectance values, across the measured wavelengths, form a spectral signature for a particular area on the ground.

Multispectral and hyperspectral sensors are passive sensors; they measure the reflectance commonly between 300nm and 2500nm, wavelengths at which more radiation from the sun penetrates the atmosphere. This range covers the visible section of the spectrum, the NIR (near infrared) and the SWIR. The specific wavelengths at which the measurements are taken are called bands or channels. Multispectral sensors typically sense reflectance for a low number of bands (5 to 15), while hyperspectral sensors measure values for hundreds of different wavelengths. Hyperspectral data for a flat, square patch of ground can be imagined as an image cube. There are the two physical dimensions (assuming a flat picture) and a third dimension of reflectance values through the measured spectrum as shown in Figure 3, commonly referred to as a ‘hypercube’.

In forestry and other large-scale applications, popular remote sensing platforms include airplanes and satellites. Sensors mounted on spaceborne platforms have the opportunity to cover larger areas. There is generally a trade-off between swath width and spatial resolution. For mapping applications on a landscape level, as opposed to individual trees, a wide field of view for a large swath width may be more important than a small pixel size. Planning, construction, testing and launch of a satellite into orbit is an expensive [48] and risky process. Once the satellite is in orbit and has been calibrated, data may stream forth in terabytes. Such volumes require storehouses and powerful computation to glean useable information. Satellites collect and transmit data through their working lifetimes, which are often planned to be five years (Landsat 4 and 7, GOES 10-12 and Radarsat-1), but can be longer or shorter. Some nations have made their data freely

available such as MODIS (Moderate Resolution Imaging Spectroradiometer) by the USA [49]. Ordering an airplane to fly over the area of interest incurs considerable expense for each flight, depending on the transit distance and the type of plane. The data products from airborne sensors are generally higher resolution and can require smaller corrections for atmospheric absorption compared to satellites. The choice of platform largely depends on the application and budget.

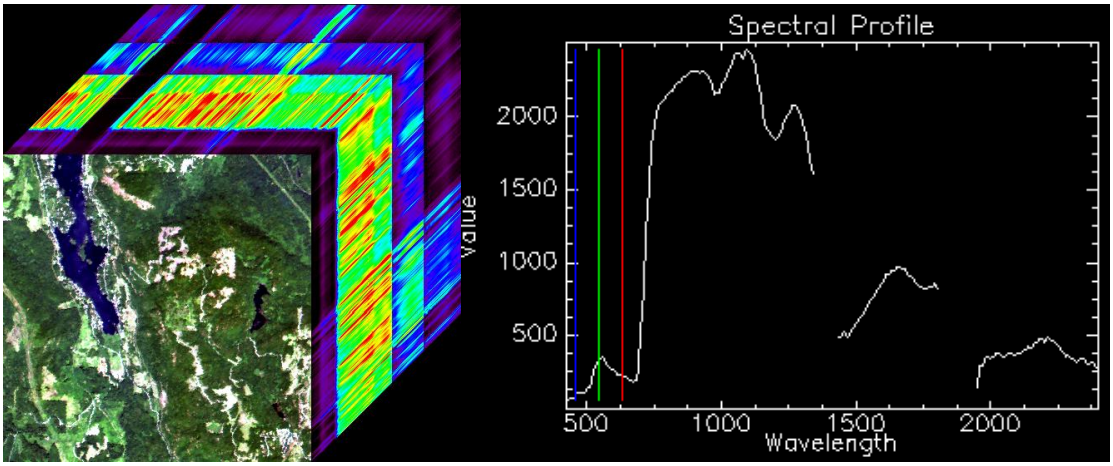

Figure 3: A hypercube or cube of hyperspectral data. This is AVIRIS data from 2001 of the Greater Victoria Watershed District (GVWD). Two dimensions represent a flat image of the ground (dark blue lake, white exposed land and green vegetation) while the third dimension is the reflectance information. Bands at the following wavelengths make up the colour image of the ground: red 635.19, green 461.04nm, and blue 548.09nm. One point of spectral data is shown on the right, for a particular physical location on the Eastern side of the image in a forest stand. The breaks in the spectrum are due to removed reflectance bands which had been affected by high atmospheric absorption.

Satellites and airplanes on remotes sensing missions often carry more than one instrument, collecting different types of data for the same spot on Earth, which can be used in concert to infer more information about the study area. This is referred to as *data fusion*. Keeping with a forest example, an optical sensor may be flown with a lidar sensor over a stand of trees [40]. The resulting data will include reflectance data of the area as

well as the height information. Together these data forms a three dimensional picture of the forest, as in Figure 4.

Figure 4: Image from UVic's Specim AISA (airborne imaging spectrometer for applications) sensor draped over a lidar digital surface model. Colour composite is Red: 640nm, Green: 550nm and Blue: 460nm.

The data format resulting from remote sensing will depend upon the sensor type. There are commonalities across sensors, though, including the need for *geocorrection*: to link the pieces of data with the correct geographical locations. Knowledge of the movement of the plane or satellite is crucial for geocorrection. Correction for atmospheric absorption or *atmospheric correction* is a common step for multispectral and hyperspectral data. Software is often employed for correction and interpretation of the data to physical units.

Computer programs are also frequently used for the visualization and for further processing of the corrected remotely sensed data to detect and map classes of interest.

1.3 Reducing Emissions from Deforestation and Forest Degradation in Developing Countries (REDD+)

In May of 2010, there were 58 countries in the REDD+ partnership. In November-December 2010, REDD+ was adopted by the State Parties of the United Nations Framework Convention on Climate Change (UNFCCC) during a climate change conference: the 16th Conference of Parties or COP16, in Cancun, Mexico. This agreement is a continuation of what RED (focussed on deforestation) and REDD (added forest degradation) had been, which is to reduce greenhouse gas emissions from forests to mitigate climate change, with an emphasis on sustainable management of forests and the conservation and increase of forest carbon stocks [50]. Actions are planned for 2011 and 2012, taking into account feedback from RED and REDD experiences [51]. The REDD+ initiative is an international, global-scale undertaking which can be helped enormously by remote sensing tools. Participants and stakeholders require that their investments in forest preservation are being honoured as per their agreements. A fundamental challenge lies in the definition of forest, which differs from country to country: in Australia the National Forest Inventory's definition requires trees exceeding 2 metres and a crown cover of at least 20 per cent [52]. Every member country in the European Union (EU) has a different forest definition but for inventory purposes the EU expects a minimum area of 0.5 ha and 20% canopy closure or 10% for Mediterranean forests [53, 54]. With existing sensors on satellite and airborne platforms, images of forests can be acquired efficiently and objectively.

A simple overview of the REDD+ framework is depicted in Figure 5.

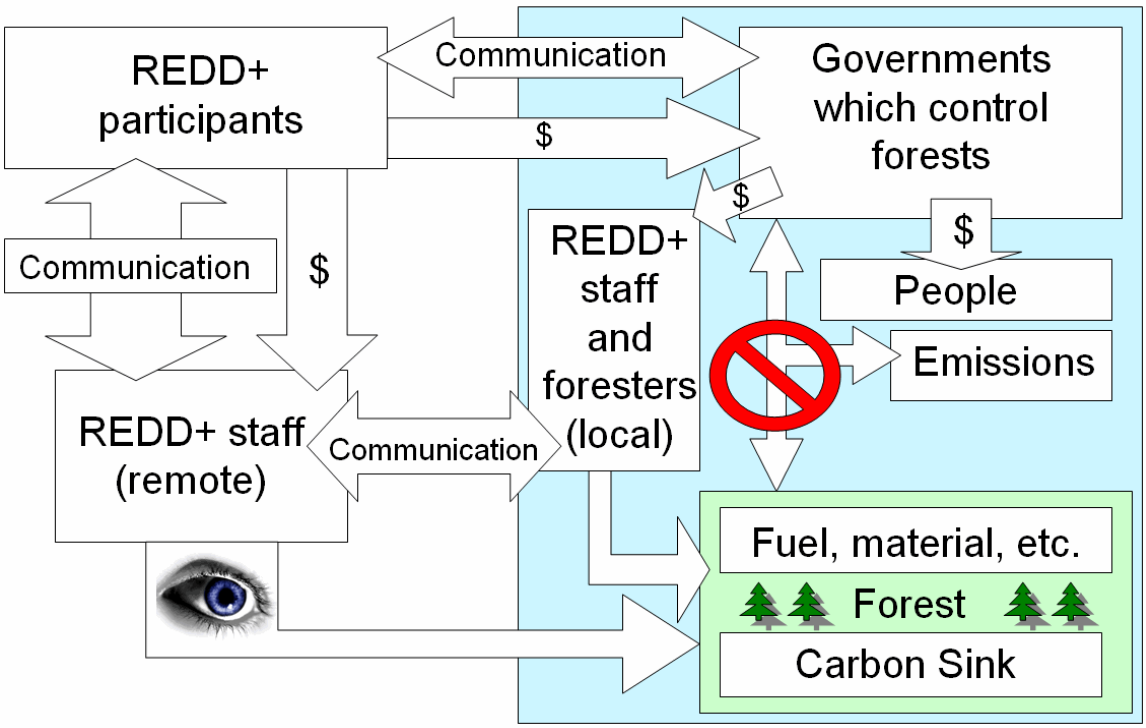

Figure 5: A simplified model of how REDD+ operates. Forests are monitored locally and remotely to ensure their sustainable use [50].

1.4 Existing Solutions

The USDA (United States Department of Agriculture) Forest Service and the USGS (United States Geological Survey) have a number of software and web-based tools for forest management and carbon estimation available on their websites. Some of these tools base their calculations on forest information from the National Forest Inventory and Analysis databases (FIDO, Carbon Calculation Tool 4.0 [55]); others use models to simulate forest characteristics and behaviour (TWIGS [56], ACORn, LANDIS, NED, i-Tree and UFORE). The tools do not use remote sensing data directly, except for i-Tree's Canopy tool, which utilizes Google Maps' aerial photography.

In Canada, the Canadian Forest Service reports carbon through NFCMARS (National Forest Monitoring, Accounting and Reporting System). The managed forest (230 million

hectares in 2006 according to NFCMARS) is reported upon on an annual basis. CBM-CFS2 (Carbon Budget Model of the Canadian Forest Sector Version 2) is a simulation tool for estimating forest carbon for Canada [57, 58]. Remote sensing is being integrated into the carbon accounting activity through change mapping. A computing system called KPACS (Kyoto Protocol Automated Classification System) was developed in UVic's Computer Science department to compute Kyoto Protocol products from remotely sensed Landsat imagery. The results can validate CBM-CFS2 simulations [2].

Large scale, remote sensing forest cover mapping processes [59] and systems [49] exist. Forest cover, being the area which meets the definition of treed, only specifies the footprint, not the volume and biomass of the forest. Change over time in that area can be detected and reported as deforestation, but harvest through thinning goes undetected for low resolutions, such as with the SAR technique in [60].

Scientists can acquire physical structural information with SAR and other radar/lidar techniques; however, there are ground-cover types which can be distinguished by features in the optical spectral range, which radar would not detect. Forest management is one such application. Aboveground carbon estimates will be more accurate with the incorporation of hyperspectral data for classification of forest type and species.

1.5 Research Questions

As technology progresses and research expands our understanding of the carbon cycle, it becomes possible to make improvements upon the existing systems and processes for estimating forest carbon. The questions to drive this research are as follows: (1) How do we map with remote sensing aboveground carbon in the forests? (2) How do we

determine the accuracies of these aboveground carbon maps? (3) How an automated system can be designed for creating aboveground carbon maps?

The first research question has answers in existing solutions and in the comparison and improvement of their methodology. To respond to the second question, the accuracy of existing and potential systems will be investigated. Tests of accuracy will be developed and applied to aid the improvement of a carbon estimation tool. To satisfy the last question, a practical system for producing aboveground carbon maps will be described and implemented, taking into account high accuracy and usability.

Computers and computer systems have been present throughout much of the history of terrestrial remote sensing. Software tools and algorithms are necessary to make sense of the very large and often complex datasets acquired from satellites and airborne sensors. The application of remote sensing for forest carbon estimation will require extensive computational assistance. This thesis will examine the design and accuracy of a software system which takes remotely sensed data and produces an aboveground carbon map.

2 Remote Sensing Data for Carbon Estimation

2.1 Overview

Aboveground carbon estimation for forests requires information about the volume of the trees above ground level. This information can be used to create a map of how much carbon is stored in the trees. Much of this information can be acquired remotely. See Figure 6 for a block diagram of the basic procedure used to get from remote sensing data acquisition to carbon map.

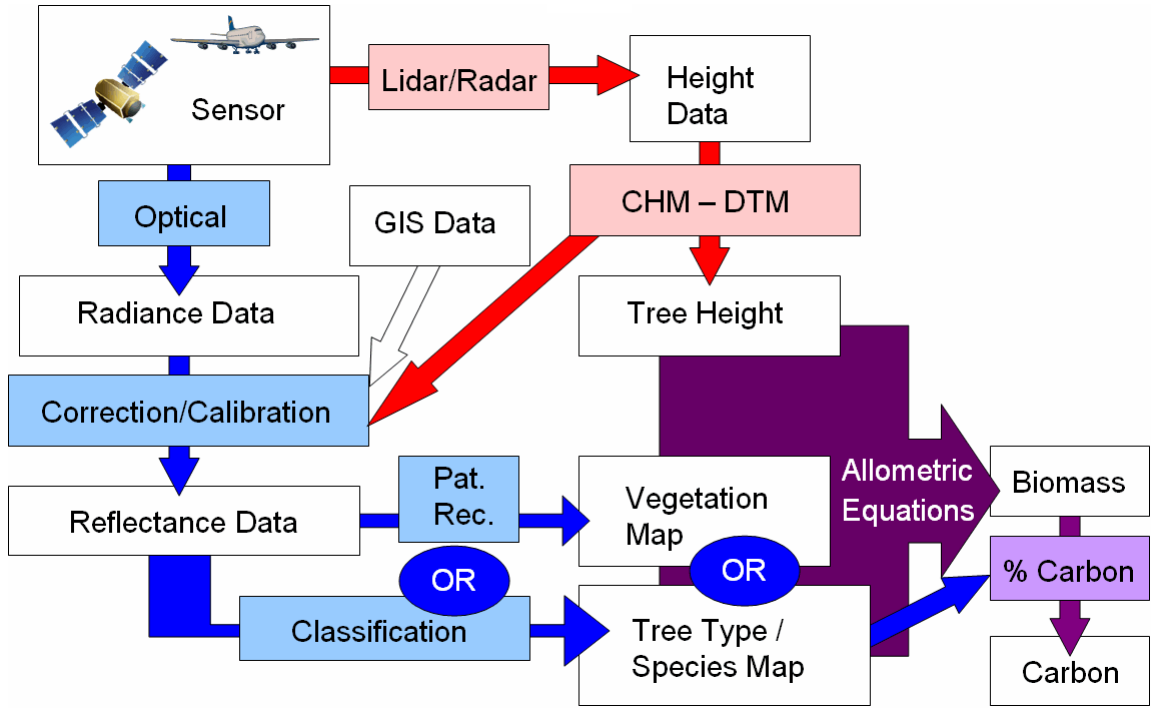

Figure 6: A flow chart of the processing of radar or lidar and optical data to create aboveground carbon maps. Here Pat. Rec. is an abbreviation for pattern recognition, CHM denotes a canopy height model and DTM means digital terrain model.

2.2 Tree Height

Tree height is measured so that the DBH (diameter at breast height, measured at 1.3m above the ground) and volume of the tree, assuming a tapered cylinder, can be estimated. With information on tree species and parameters like tree height and diameter, the biomass of the tree may be looked up in yield tables [7, 61, 62] or calculated through

allometric equations (discussed in further detail in section 4.1). The volume of a tree may also be calculated using height and other parameters. From volume and tree density by species, biomass can be estimated. Wood generally has a specific gravity of approximately 0.5, meaning that the oven-dried biomass is as heavy as 0.5 times an equal volume of water [63]. The measurement of tree height can be done from airborne lidar, airborne and spaceborne interferometric SAR, from stereo photography, and from shadow measurements.

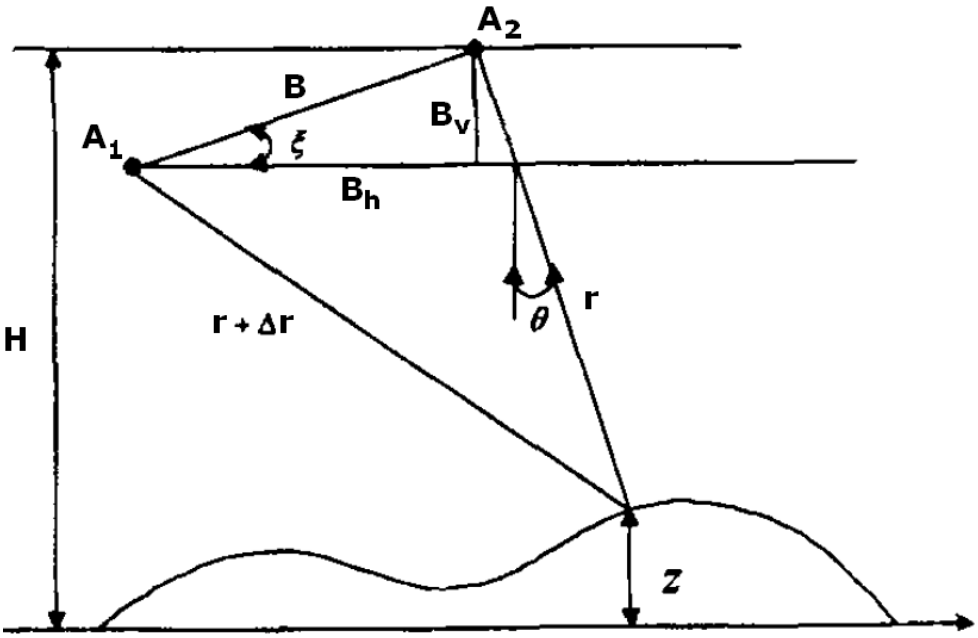

Figure 7: The geometry of InSAR, where Z is the height of an object, and A_1 and A_2 are two receivers separated by a baseline, B. [64]

Interferometric synthetic aperture radar (InSAR) is another method which can measure tree characteristics for the calculation of biomass and carbon. It was developed in the 80's based on SAR (see section 1.2 Remote Sensing) and the geometry in Figure 7. The location (including information such as height, H) and relationship between the receivers (the baseline length, B, and angle, ξ) are known, and distance values (r and $r+\Delta r$) are

calculated when radar returns are measured at the receivers. Then equation 3 [64] can be used to find the height of the object:

$$z = H - r[\cos\xi\sqrt{1 - \sin^2(\theta - \xi)} - sin\xi\sin(\theta - \xi)] \quad \textbf{(3)}$$

The SRTM (Shuttle Radar Topography Mission) of 2000 covered 80% of the Earth's land mass with C-band (5.6 cm wavelength) InSAR and this data has been made available to the public[65, 66]. The SRTM is illustrated in Figure 8; it has measured canopy height for red pine stands with an RMSE of 4m [65]. High correlation coefficients (r was 0.97 with an RMSE of 1.2 m) were achieved between lidar mean height and InSAR height predictions (SRTM heights minus a DEM from the National Elevation Dataset) for the stand level in the eastern United States [67]. X-band (3.1 cm wavelength) and C-band InSAR from SRTM has generally underestimated canopy height by two thirds to one half [68]. Adjusted InSAR data could be used to extrapolate lidar height measurements to the larger areas covered by spaceborne radar [67]. X-band InSAR height measurements from SRTM were strongly related to forest parameters, including volume and biomass, in a study of spruce forest in Norway [68].

There are limitations to measuring height and biomass of forest with InSAR: SAR microwaves will penetrate into the canopy to the center of the backscatter, making InSAR height measurements lower than the true tree height, though only by a few metres if using X-band [68]. X-band InSAR alone may not be able to distinguish forest stands of less than 4 metres in height, and its relationship to biomass saturates at 200t/ha when using the techniques in [68].

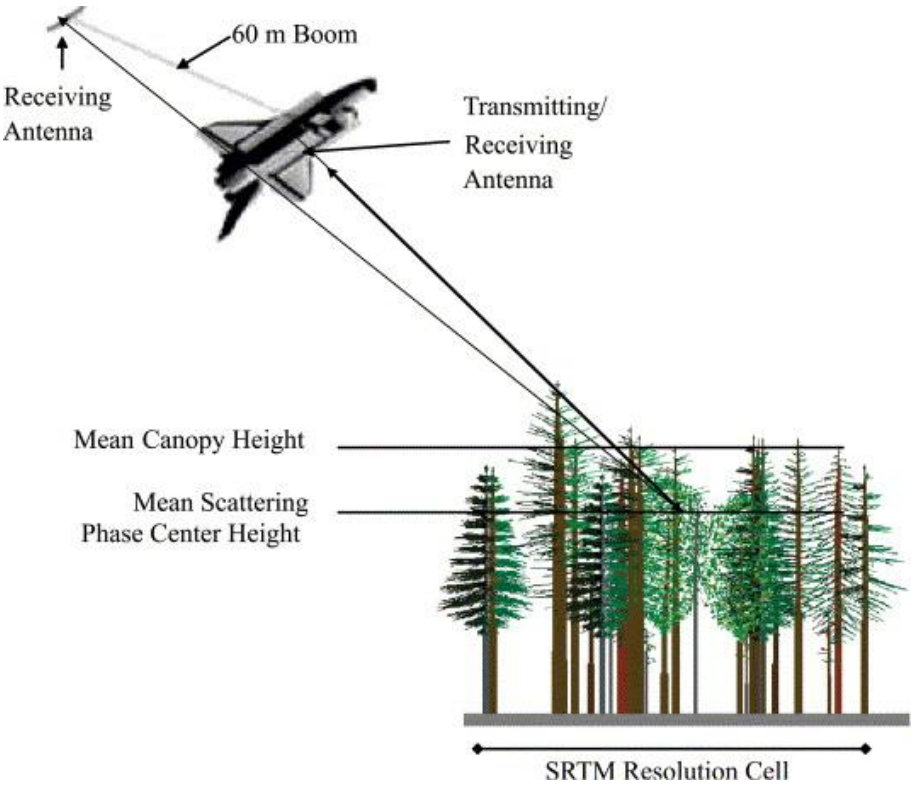

Figure 8: The SRTM was the first spaceborne fixed-baseline InSAR. It had a 60m boom separating the two receiving antennae. Shown is the mean canopy height and the "scattering phase center height", which is notably lower than the true canopy height. [65]

Lidar and SAR were compared for biomass calculations in [69] for a site in Scotland. The SAR data were from a fully polarimetric image from the TerraSAR-X satellite and the quad-pol PALSAR (phased array type L-band SAR) on the ALOS satellite. The high resolution lidar allowed a detailed study of the relationships between stand density, height and biomass; it also incorporated small trees into the biomass calculations which SAR missed [69]. The SAR data were found to have the potential for biomass estimation over a large area, but this was limited due to lower resolution and saturation in high biomass density in this case (over 60t/ha for TerraSAR-X and over 150t/ha for ALOS PALSAR caused saturation) [69]. In another study which compared lidar, SAR and InSAR, a linear lidar model was able to explain 83% of biomass variability in the test site

in the south-western United States of ponderosa pine plantation forests. SAR and InSAR could capture only 30% of the variability with a higher prediction error: 52.5 t/ha compared to lidar's 26 t/ha [70].

Tree height can be measured with shadows from optical data. Using precise knowledge of the sun's angle at the time of the acquisition and trigonometry will give a height for the tree casting the shadow. This method suffers from many limitations including close spacing of the trees in the image. Only trees close to the edge of the forest or trees in isolation can be measured with shadows and the height of the rest of the stand must be modelled based on these edge trees. Also, the spatial resolution of the imagery will force an error margin on any length measurement made from the data. Other limitations are shown in Figure 9.

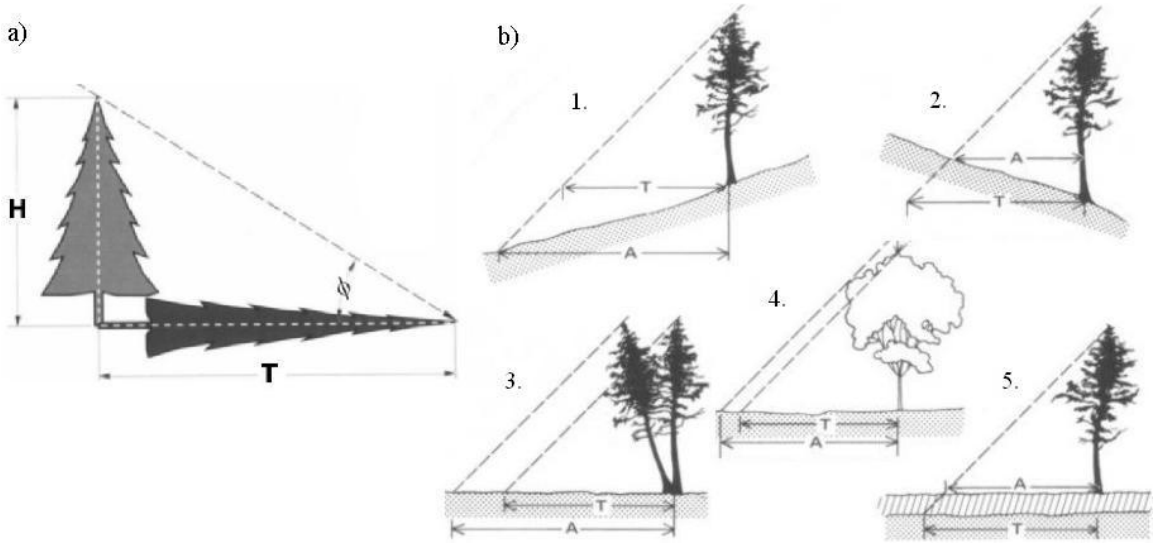

Figure 9: (a) How tree height, H, is measured from shadow length, T; and (b) common difficulties when the actual shadow length, A, is not the expected shadow length, T. (1) and (2) show slopes of the ground which can result in incorrect height calculations. (3) shows a leaning tree. (4) shows a tree with a large canopy which will cast a larger shadow. (5) shows a tree with a bent stem. [71]

Finally, tree height can be estimated by stereoscopy, which is simultaneous or near-simultaneous optical images of the area from two angles. Equation 4 [71] gives the height of the object of interest, H_o, (a tree) using the height of the platforms, H_p, absolute parallax, aP, and differential parallax, dP, illustrated in Figure 10.

$$H_o = H_p \times dP / (aP + dP) \quad \textbf{(4)}$$

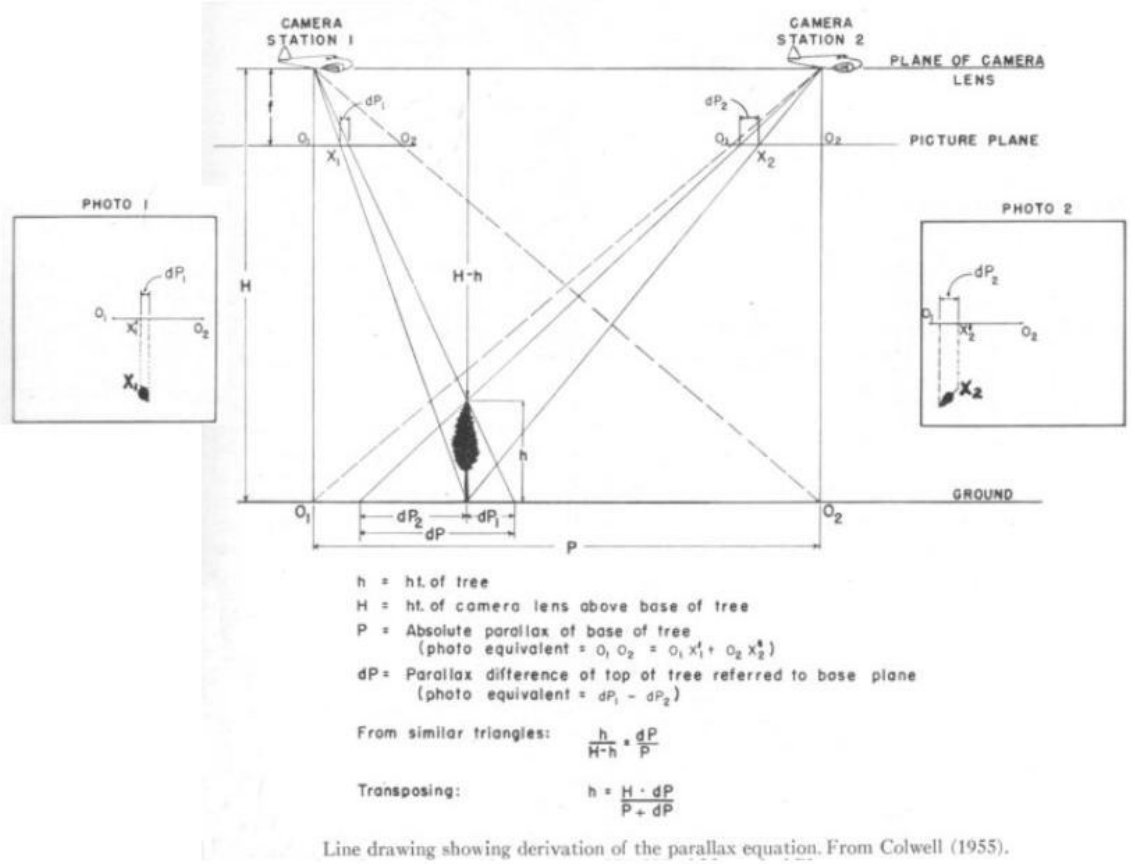

Line drawing showing derivation of the parallax equation. From Colwell (1955).

Figure 10: Illustration of the derivation of the parallax equation for finding tree height [71].

An experiment, generating a DEM (digital elevation model) from SPOT-5 satellite along-track stereo images over an 80km by 60km area, gave height accuracies compared to a high-quality reference DTM (digital terrain model) which ranged from within 16.7m (mountainous terrain) to within 4.4m (flat and moderate terrain), but compared to check

points which were measured by human operators from the images had RMSE (root mean squared error) values of 1.9m for height, 2.3m for northing and 2.7m for easting [72]. Typical tree heights in the study sites are 13.87m for Rithet and 14.54m for D4S2.

For stereoscopic tree height calculations, the images must have precise geographic alignment and individual trees or tree-stands must be identifiable in both images to make the measurements and calculations. The resolution required for identifying individual trees must be smaller than the tree crowns that are to be recognized. Johnson's criteria outlines the minimum number of pixels across the smallest dimension of a target for discrimination as 2 pixels for detection, 2.8 pixels for knowledge of orientation, 8 for recognition or 12.8 for identification [73]. Research done on human recognition of mines in sonar images concluded that 6-10 pixels across the smallest dimension would allow for target recognition with misidentifications below 5% [74]. While human vision is still more successful at object recognition [75], to do manual tree identification and matching over a large area is a tedious task. There are algorithms which allow computers to find tree tops with relatively high accuracies, which will be discussed in section 2.5.

2.3 Light Detection and Ranging (Lidar)

Lidar uses laser energy in radar fashion. An example application would be to observe atmospheric or terrestrial backscattering as a function of range [76]. In its basic form, lidar sends out pulses of collimated energy (parallel rays) to the target and the backscattered energy is collected by a lens or reflector system and detected by a photomultiplier [76]. A scanning mirror directs the pulses back and forth as the platform moves forward along the flightline [77]. A GPS (global positioning system) is used to track the co-ordinates of the laser source and an IMU (inertial measurement unit)

measures the orientation parameters of the scanner to calculate the direction of the pulse [77-78]. With the ranging data accurately measured and time-tagged by an ultra-accurate clock, the position in the horizontal and vertical planes of the return pulses can be calculated [77]. The simplified function for distance is given in equation 5, where c is the speed of light, t_0 is the time at which the pulse was emitted and t_r is the time the response was measured.

$$\text{Range} = c \times (t_r - t_0) / 2 \quad \textbf{(5)}$$

Data point density depends on the number of pulses transmitted per unit time, the scan angle of the instrument, the elevation of the aircraft above ground level, and the forward speed of the aircraft [77]. The majority of the commercial systems can collect between 20,000 and 75,000 records per second [77]. The horizontal (x and y) and the vertical (z) directions are shown in the far left of Figure 11.

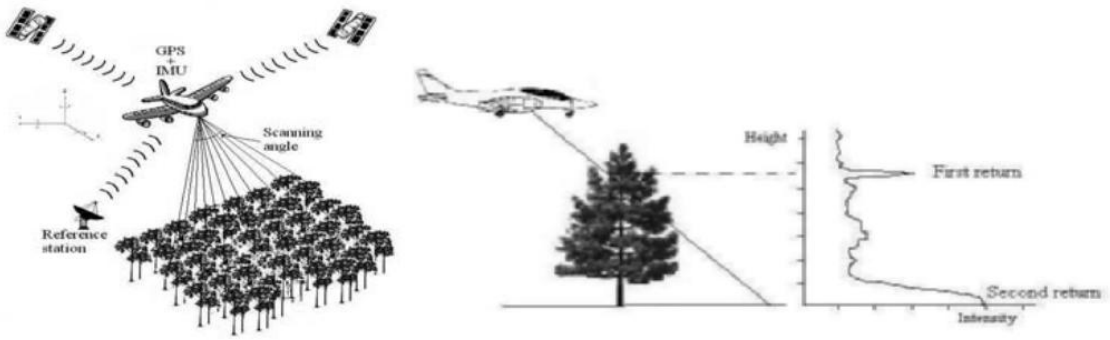

Figure 11: Airborne lidar using GPS is shown on the left. On the far right intensity of the returning signal is plotted against height. The strongest returns represent a height near the top of the tree (first return) and the height of the ground (second return). [79]

The lidar flown with the University of Victoria's (UVic) hyperspectral sensor, the airborne imaging spectrometer for applications (AISA), uses light pulses at a wavelength of 1064 nm, which is the most common wavelength for terrestrial lidar sensors [80].

Commonly employed wavelengths in earlier lidar systems [76] include 694.3nm for ruby lasers and 1060nm for neodymium lasers. Lidar sensors often use near-infrared wavelengths for its strong reflectance off of vegetation and human-made surfaces [78, 80] and high transmittance through the atmosphere [80]. The reflectance of these pulses is measured and timed to determine distance. The last response is the pulse as it is reflected off of the ground, which creates a map of the surface which is sometimes referred to as the BEM (bare earth model) or DTM. The first response data will represent the tree canopy in the case of forest remote sensing and is called the DSM (digital surface model). Figure 12 shows an example of lidar responses in an area with sparse trees. Subtracting the first response height and the last response height will give the tree height, or CHM (canopy height model), as in equation 6.

$$DSM - DTM = CHM \quad \textbf{(6)}$$

Lidar pulses may strike multiple surfaces and reflect portions of the energy in different directions and at different times. Lidar systems measure these responses depending on type: profiling lidar only measures one return for each pulse [80], discrete-return lidar systems use short laser pulses and measure one or more (multiple-return lidar) returns based on the intensity of the signal [78, 80], before filtering to isolate the last return (from the ground) [81]; and continuous or waveform lidar records all of the returns for each pulse, continuously measuring [78].

Profiling lidar sends pulses down at nadir to provide surface elevation data [78]. Pointing near nadir can prevent ranging errors in airborne lidar [70]. There are also scanning lidar systems which use optics to change the angle of the exiting beam, covering a greater area in one pass. This angle information is used in determining the physical

location of the surface reflection points. High-angle pulses and topography can interfere with the quality of the return [78]. A scan angle within 18˚ of nadir is recommended by [81] and within 12˚ by [80] to avoid distortion. Profiling sensors are the simplest design and generally only record one return at coarse sample densities in a narrow swath [80].

Figure 12: A vertical cross section plane of a lidar point cloud acquired from a hilly Acacia koa woodland in Hawaii in February of 2010. The white points are the last return. The lidar was flown on a Jet Ranger helicopter at approximately 685m altitude. The emitted light had a wavelength of 1064nm. The pulse rate was 260 KHz, and the spatial footprint was approximately 14cm [41].

It is costly to have lidar flown by plane and this is reflected in studies which choose only small areas of detailed coverage [82] or to acquire lidar simultaneously with hyperspectral imagery [40, 83]. Two references, [77, 79], give a cost of £5 ($12.26 CAD, in September 2002, when the data was acquired) per hectare for lidar coverage of a

17.5m^2 area and a 20m^2 with an Optech ALTM2033 device which measured 3-4 returns per m^2. In [70], lidar is described as being sensitive to the pitch and roll of the aircraft, causing gaps in the data; thus other studies choose to average the height data to get the height of a whole stand of trees [84].

Alternatively, spaceborne lidar, mounted on a satellite platform such as NASA's ICESat (Ice, Cloud, and land Elevation Satellite), which was launched January 12, 2003, is mainly used for ice and atmospheric observation [85, 86]. Experiments which have used spaceborne lidar for forestry applications [87, 88] concluded that atmospheric noise interfered with analysis and large spacing between measurements posed a limitation for its use on small scales.

The lidar on ICESat, called GLAS (Geoscience Laser Altimeter System), had a 65m footprint which was spaced every 172m. The data covered only 2.4% of the Earth's forest surface, yet [89] used GLAS measurements for a global map of forest height with help from a multispectral sensor, MODIS (Moderate Resolution Imaging Spectroradiometer) and through interpolation with models. ICESat was decommissioned in 2010, but a second satellite, ICESat 2 has funding [48] and is slated for launch in 2016 [19].

2.4 Lidar Accuracy

Thanks to advances in GPS and IMUs (inertial measurement units), lidar has accuracies on the order of 15-20cm RMSE vertically and 20-30 cm horizontally [77]. For a study site in central Spain of Scots pine (*Pinus sylvestris*), vertical RMSE (root mean square error) obtained with a TopoSys II lidar for the DTM in open areas and for the DCHM (digital canopy height model) were 0.30 m and 1.3 m, respectively, which is

acceptable [90]. An error of 12% or lower for the height of large trees is considered to be a good accuracy for lidar [91].

Lidar has been shown to underestimate the heights of trees: in [92], terrestrial and airborne lidar gave measurements that were 1.1m and 1.2m shorter than the traditional methods, respectively. In the case of this study the airborne lidar, a discrete pulse return lidar by Optech Inc. (ALTM 2050) only measured 96% of the manually measured heights of the red pines (*Pinus resinosa*) [92].

On average, airborne TopoSys-1 lidar underestimated height by 0.97m when compared with the field measurements in 50ha of state-owned forest, located in Kalkkinen, southern Finland [93]. The corresponding height underestimations were 0.80 m for Norway spruce (*Picea abies*), 1.20 m for Scots pine (*Pinus sylvestris*), and 0.91 m for birches (*Betula*) [93].

A study of broadleaved trees found a mean of -0.91m for sample shrub canopies and -1.27m for sample tree canopies, compared to ground measurements [94]. The sampling density in relation to canopy surface roughness is considered important in regard to these inaccuracies [94].

Lidar gave Douglas-fir heights within 6% (with a mean of 3%) and R ~= 0.8 near Shawnigan Lake on Vancouver Island with an Optech ALTM 1020 [95]. Mean height of laser canopy heights of the Douglas-fir was 3.1 m lower than the mean field height [95]. Another Douglas-fir study using a Lightwave Model 110 Terrain Scanning Lidar found the lidar underestimates the ground measured tree height (plot height averages from 24.4 – 26.2m) by an average of 1.32m [96]. A comparison between the predictions from

Optech ALTM 2033 lidar and field observations (354 trees, predominantly Sitka spruce, in 10 plots) confirmed that the ALS underpredicted individual tree heights by 7–8% [77].

Canopy height was consistently underestimated for Optech ALTM 1210 lidar measurements of ash (*Fraxinus excelsior*), oak (*Quercus robur*), and field maple (*Acer campestre*), though r coefficients were high: 0.76 for trees (n = 39) and 0.90 for shrubs (n = 43), respectively [61]. Height errors increased as a function of canopy height [61].

It is suggested that lidar frequently misses the tops of trees; dense forest obscures the true ground level, skewing the tree heights; small-crowned trees are often skipped; and other trees have multiple returns which result in false, additional tree tops [77]. These errors can be reduced by increasing the density of measurements to 6–10 returns per individual tree canopy or using recovery models [97]. A study of over 1000 trees in Oregon, USA, using an Optech 3100 lidar system with 7.52 returns per m^2 only had an underestimation of 0.59m for conifers, 0.29m for leafy deciduous and 0.58m for leafless deciduous [98].

2.5 Automatic Delineation of Canopies and Tree Tops

Manual inspection of imagery or height data to find the apex of trees or to separate adjacent canopies is too labour intensive for large scale areas. Instead, computer programs can do the job. Algorithms for ITC (individual tree crown) identification fall into two main categories: bottom up, such as valley-following methods, and top down, like the watershed method [91].

The local maxima approach was successful in a study in Finland of 682 trees, predominantly Norway spruce, in 10 plots with stem densities ranging from 425 to 1656 stems/ha [93]. The proportion of detected trees was only 39.5% of all trees; however, the

proportion of detected dominant trees was 83.0% [93]. In one of the samples, all dominant trees were found, and the lowest proportion of detected dominant trees was 63.4% [93].

Gougeon's ITC algorithm [37], developed for use on high resolution orthophotography and spectral imagery, operates on the assumption that the image is brighter in the tree crown than in the area between tree crowns [99]. It starts at a local minima (darkest pixel or lowest point in a CHM), follows the valley (dark outlines) until a complete delineation of a crown is done [79]. In a second pass, crown clusters are refined into individual crowns, favouring counter-clockwise turns [79]. A jump factor allows crowns to be split from one indentation to another, pointing inward at a similar angle [79]. Gougeon's ITC algorithm was developed for use in dense conifer stands in Canada where there are shaded gaps between trees [99], but has been applied in Japanese plantations [91], Scottish woodlands [79] and dense Australian forests [100] for evaluation. Qualitatively, Gougeon's algorithm produces good results in terms of correspondence with ground information and what can be seen visually on the imagery of old growth conifer (200-800 years), 26–45 m in height with densities from 340–380 stems/ha, as well as denser (750-2751 stems/ha) young conifer trees with heights 10-14m [99, 101]. Quantitatively, the algorithm yielded 80-90% correspondence with ground data for location of trees in a test site of even aged (55 years old) Douglas-fir plots of varying densities (300, 500, and 725 stems/ha) on the west coast of Canada, when applied to multispectral images and high density lidar (≤70cm resolution) [96].

Three ITC methods, including Gougeon's, were compared in a study site in Scotland of Sitka spruce trees in plots ranging from 344 to 580 stems/ha in density, on a lidar-derived

canopy height model [79]. In Weinacker's algorithm [102] maxima are found for tree tops; then a pouring algorithm starts from the tree tops and sets a lower height threshold for the crowns. Afterwards, the crowns which are unusually shaped are reassessed with rules regarding the expected size and shape of a tree crown in proximity to the tree top. Popescu's algorithm [103] uses an n × n window and also a circular one. It requires minimum and maximum crown diameter values and a user-provided relationship between tree height and crown size. Results of the comparison follow: Popescu's algorithm was found to be better than Weinacker's and Gougeon's for determination of number of stems and tree height in the study; the algorithm by Gougeon was the most suitable to estimate individual crown diameter (RMSE of 1.81m) and stem diameter (RMSE of 7.05cm) with equation 10; finally, the algorithm by Weinacker was the most suitable to estimate stand basal area (RMSE 24.3%) and volume (RMSE 29.4%) [79]. All methods underestimated forest parameters but were as accurate as field methodology for estimating heights [79].

Another tree top finding algorithm is described in [39]; it requires a user-defined radius, which is used in a circular local maxima filter. When the edges of a canopy are found, the lidar points inside are removed from the rest of the process. The result is a vector file for the canopy areas and the tree tops. 83% accuracy was achieved in one of the study plots, with a maximum root mean squared error of 1.14 (meters from actual location) [39]. This algorithm was used in [104, 105] to generate tree top locations for biomass calculations.

Classifications on individual trees' canopies have been run, after crown identification, for an overall accuracy of 78% using four bands (visible blue, green, red and NIR)[91]. The resolution of the imagery was 50cm and the crown delineation required some manual

intervention for irregularly shaped crowns [91], which would be impractical on a large scale. A spatial resolution approximately an order of magnitude less than the average crown diameter in the scene provides good results for crown identification and tree top location [100].

2.6 Tree Species

While coniferous (softwood) and deciduous trees (hardwood) can be distinguished with lower spectral resolution [106, 107] or through structural analysis [108, 109], differentiation of tree species requires high spectral resolution sensors [41, 104, 105] or very high spatial resolution photography [91] and botanical experts or an abundance of training data.

The dominant species in the GVWD study areas are Douglas-fir (*Pseudotsuga menziesii*) followed by Lodgepole Pine (*Pinus contorta*) and Western Hemlock (*Tsuga heterophylla*) [104, 105, 110]. The dominant understory is salal (*Gaultheria shallon*), a native evergreen shrub with broad, waxy leaves [111, 112]. A picture taken in September of 2000 for during field work in the GVWD is shown in Figure 13.

Figure 13: Large conifers and salal bushes at plot number 9 during EVEOSD (Evaluation and Validation of Earth Observing-1 for Sustainable Development) field work. The foliage of 10 Douglas-fir trees from each plot was sampled for chemistry.

Douglas-fir is one of the premier timber trees in the world due to high productivity and superior wood quality; it covers approximately 4.5 million hectares in Canada [113]. It reaches up to 126m in height and 5m in diameter[113] and can reach an aboveground volume up to 5460 m^3/ha in old growth stands [114]. Naturally regenerating, unmanaged Douglas-fir on a good site would be expected to produce 174 m^3/ha after 50 years or 643 m^3/ha if closely managed (thinned and fertilized) [113]. Closer planting density has been linked to increased DBH and higher survival rates for saplings, though this trend does reverse as the trees pass 20 years of age [115]. Because good cone crops only occur in Douglas-fir at intervals of 6-7 years, planting has allowed for much faster reforestation [113].

Lodgepole pine is the most widespread conifer in western North America, though in the coastal regions it is largely confined to marginal sites [116]. Lodgepole pine tend to be small trees which seldom reach large sizes or great ages; however, a 100-year-old, 32m tree has been observed on Vancouver Island [116]. The other 100-year-old lodgepole pines on the same site were under 5m in height [116]. Unusually large diameters and heights for the coastal trees are 86cm and 36m, respectively [116]. The bark and wood properties are highly variable, and coastal wood is denser (specific gravity of 0.58) and has more pitch than trees in the interior [116].

Western Hemlock is an important commercial softwood species, with the largest and fastest-growing stands found in humid coastal regions such as in British Columbia [117]. In good growing conditions it can reach almost a metre in diameter and 69m in height [117]. Western hemlock trees produce long, symmetric boles with relatively thin bark with deep fissures[117]. It produces some seed every year and heavy crops at least every

8 years, which germinate well on a diverse range of material, with adequate moisture [117]. Its average specific gravity is 0.42 [117]. Western Hemlock is a primary late-successional species that usually aggregates in gaps in the Douglas-fir canopy [117-118].

Other minor components in the GVWD include Western White Pine (*Pinus monticola*), Western Red Cedar (Thuja plicata) and Red Alder (*Alnus rubra*) [118]. Red Alder is a characteristic associate of Western Hemlock and Douglas-fir; it is found patch-wise and as single trees amongst stands of these conifers [119]. Concern for long-term site productivity has popularized the co-cultivation of Douglas-fir and Red Alder, a nitrogen-fixing angiosperm [113].

Red Alder is a fast-growing hardwood species that is widely planted in the Pacific Northwest, USA [120]. These trees have smooth, tapering boles and short, dome-shaped crowns [119]. The specific gravity of the wood at breast height (0.40) does not vary significantly among the provenances on the Pacific coast [121]. Red alder requires an abundant supply of soil moisture, does not live much longer than 100 years or grow much larger than 76cm in diameter or 40 metres in height [119].

3 Study Areas and Data Collection

The two study sites are located on Vancouver Island in the GVWD (Greater Victoria Watershed District). The GVWD is located about 30km northwest of Victoria, British Columbia and is approximately 350 km^2 in size [122]. It is a temperate, coastal rainforest [104] and mainly coniferous [122], with 90% of the trees being Douglas-fir [123]. The watershed contains forest stands of various age classes due to logging and reforesting over the last century; it includes some of the oldest, unmanaged stands of Douglas-fir in the southern Vancouver Island [105, 123]. Terrain in the Rithet flightline is rugged with elevations between 150 and 500 metres and slopes up to 45 degrees [105]. The average elevation of the GVWD is approximately 400 metres above sea level [123]. Details on the terrain and soil characteristics in the VWS (Victoria Watershed, South) which were collected in the 1990's can be found in Table 8 [124].

Two sets of hyperspectral data from these areas, as well as other data for the region, will be the focus of the biomass investigations and used for testing of the system developed in this thesis: D4S2 (District 4, Scene 2) and the Rithet Creek area, shown in Figure 14.

Figure 14: The Rithet Creek region, left, and the D4S2 flightline, right with black border, both as colour composites of AVIRIS bands (R: 635.67nm G: 548.24nm B: 461.32) shown over 2010 satellite imagery at an effective altitude of 25.9km through Google Earth Pro.

Data from two hyperspectral sensors were collected over both of these areas: airborne visible/infrared imaging spectrometer (AVIRIS), which is a NASA owned sensor, and an airborne imaging spectrometer for applications (AISA) owned by the University of Victoria.

The AISA flightlines do not offer complete coverage over D4S2. One flight over the Rithet area was conducted at 10:35am PST, July 25th of 2007 with a Terra Remote Sensing (TRSI) aircraft, gathering hyperspectral data with an AISA sensor and lidar first

and last return (with approximately 1.2 returns per square metre). The five flightlines of AISA and lidar over D4S2 were collected on July 27th in 2006 [104]. The AISA field of view was 22°, and at 1700m altitude, the data has two metre pixels. The lidar field of view was 44° and was gridded to two metre pixels as well. According to the lidar CHM over the D4S2 and Rithet areas, the majority of the trees are less than 10m in height. More statistics for the forest in the study areas from the lidar CHM, processed by an algorithm by Loos and Niemann [39] to locate tree tops, are in Table 1. Atmospheric correction of the hyperspectral data was done with ATCOR 4 (atmospheric and topographic correction for wide field of view airborne optical scanner data) using a flat terrain model [104]. The data was geocorrected to the lidar canopy surface model using Caligeo software by Spectral Imaging Ltd. The AISA hyperspectral instrument is comprised of two spectrometers: one which images in the visible/near infrared wavelengths (VNIR: 400–1000nm), with a full-width at half-maximum (FWHM) of 2.3nm, and the other in the shortwave infrared (SWIR: 1000–2500nm) with a FWHM of 5.6nm [3]. The AISA data have a wavelength range of 395nm - 2503nm, with 492 discrete, contiguous spectral bands [105].

Table 1: Forest information from lidar CHM and tree top locating algorithm. Forest is defined here as trees which are 2m in height or greater.

Tree Statistic	Rithet Area	D4S2 Area
Number of trees	89985	133900
Average height	13.87m	14.54m
Maximum height	61.41m	65.53m
Minimum height, chosen	2.00m	2.00m
Average stem density	223.4 stems/ha	123.1 stems/ha

The AVIRIS data was acquired by NASA using a Twin Otter aircraft on August 12, 2002, and provided for the EVEOSD (Evaluation and Validation of Earth Observing-1 for Sustainable Development), a project led by Dr. David G. Goodenough of Natural

Resources Canada. The spectral range spanned is 400-2500nm, with 224 channels at 10nm intervals. The geocorrection and orthorectification was done using a 25m DEM (digital elevation model) which was part of British Columbia's TRIM (Terrain Resource Inventory and Mapping) data [105]. The resulting hyperspectral data have a spatial resolution of four metres: each pixel of the image represents an area of $16m^2$. An atmospheric correction was performed using FLAASH (Fast Line-of-sight Atmospheric Analysis of Spectral Hypercubes), a tool in the ENVI software suite (discussed in more detail in section 6.4)[105]. An atmospheric calibration using a linear force-fit function was applied to match the spectra to ground measurements taken simultaneously during acquisition [125].

The CRD (capital regional district) has provided 20cm ortho-photography over much of the GVWD and forest inventory information in vector files, covering much of the two study areas. The inventory was updated as recently as 2005 [105]. From this information, which includes leading tree species, average height estimates and slope measurements, a VDYP (Variable Density Yield Prediction) program was run to give biomass estimates for part of D4S2.

4 Analysis Methods to Create Aboveground Carbon Maps

An aboveground carbon map shows aboveground carbon distribution over a geographical location. For forests, the carbon quantities correspond to a particular tree or stand of trees, depending on the resolution of input data and the requirements of the end user. These carbon values are a portion of the biomass values. While the percentage of carbon in wood varies species to species [7], carbon is approximately half of the oven-dried biomass [1, 19, 20, 126]. Biomass can be estimated with *allometric* equations, which relate the growth of parts of an organism [127] and some examples can be seen in Table 2 for selected species found in the GVWD study area. The equations, discussed in more detail in section 4.1, derive tree volume or biomass from measurements of tree height and DBH.

The equation for Douglas-fir was developed for a DBH range from 5cm-54cm [128]. For the development of the western hemlock equation, the smallest DBH was 3.1cm and shortest height was 3.5m. The largest DBH was 70.5cm, and the tallest tree was 43.7m. The age range was from 11yrs to 253yrs [129]. The equation may not be valid for trees with height under 3.5m or with small DBH (< 3cm). The lodgepole pine equation is presented in [130] alongside a lookup table for oven-dry biomass for trees which range in DBH and height from 4cm-26cm and 4m-38m, respectively. The set of red alder trees used to develop the equation for biomass in [129] had a minimum DBH of 5.8cm, height of 6.1m and age of 5yrs. The maximum DBH was 33.3cm, height was 23.8m and age was 48yrs [129]. The biomass equations will work best for trees which are within the ranges given.

Table 2: Biomass equations for four tree species. Diameter at breast height (DBH) is in centimetres, height (H) is in metres and biomass is in kilograms. SEM is the Standard Error of the Mean and SEE is the Standard Error of the Estimate.

Tree Species	N	R^2	SEM (kg)	SEE (kg)	Equation for oven-dried AGB (kg) from height, H (m) and DBH (cm)	Source
Douglas-fir	60	0.97	-	0.279	$0.0808 \times DBH^{2.5282}$	[128]
Western hemlock	70	0.98	75.35	88.95	$29.8 + 155.8 \times (DBH \div 100)^2 \times H$	[129]
Lodgepole pine	149	0.98	-	5.24	$1.8962 + 0.02183 \times DBH^2 \times H$	[130]
Red alder	41	0.99	15.38	11.86	$4.8 + 206.5 \times (DBH \div 100)^2 \times H$	[129]

The more that is known about the site the more precisely the biomass can be estimated. This depends on the sensors used and a priori knowledge of the area. The hardwood versus softwood distinction can be made with multispectral data [131] and also with structural information through high spatial resolution radar or lidar. High spectral resolution (hyperspectral data) allows for the separation of forest into species classes (for example Douglas-fir and White Spruce) [132]. The wavelengths of light used by hyperspectral sensors interact with vegetation on a chemical level [133]. The resulting spectrum of information can distinguish tree species as in Figure 15.

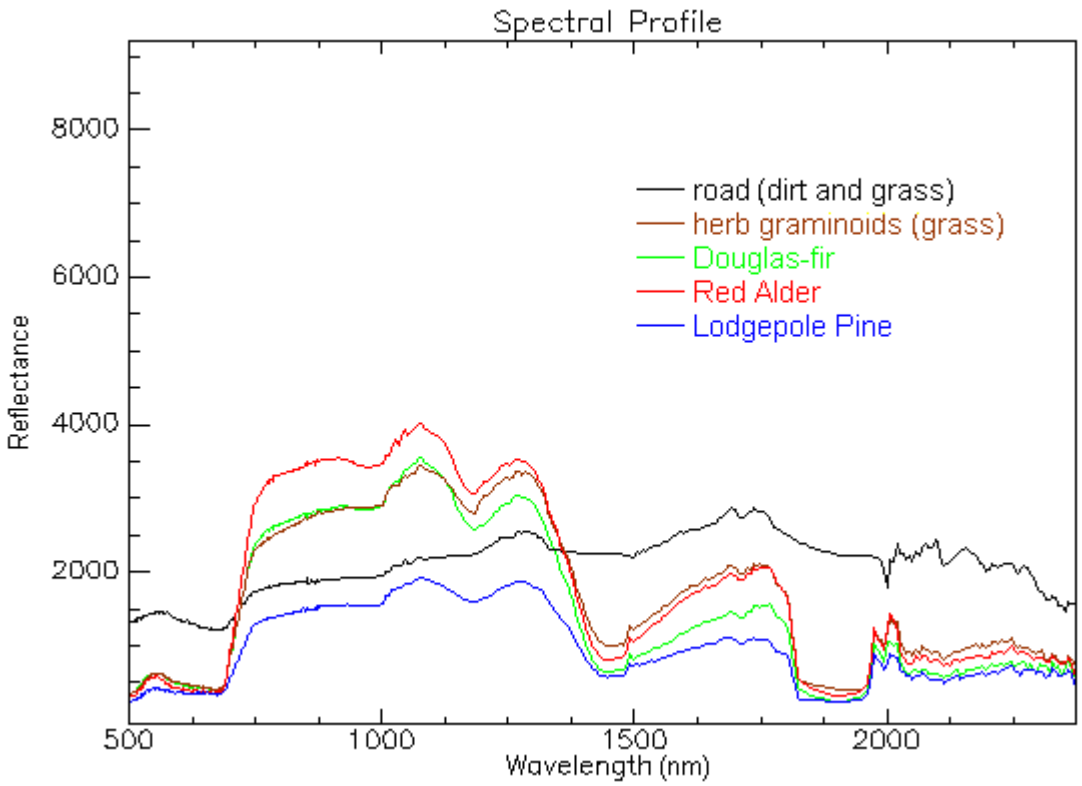

Figure 15: The reflectance spectra of different types of ground cover including three tree species. The data were aquired with AISA, a hyperspectral sensor with 492 spectral bands, in 2006 over the Greater Victoria Watershed District.

Classification algorithms are discussed in detail in section 4.4. When the remotely sensed data is classified into tree types (conifer, deciduous and mixed), a map of forest type can be generated. The different classified areas will require different equations for biomass and carbon, according to species. The different classes would be separated and the equations applied separately before combining all of the species' biomass and/or carbon results.

If a pixel contains more than one type of tree, it may be possible to determine the composite tree types, or other land cover classes within the pixel. Spectral unmixing is a tool used to identify and quantify fractional components of the signal of a pixel; it is explained in more detail in section 4.5.

4.1 Derivation of Allometric Equations

Allometric biomass equations relate tree or stand biomass to more easily measured attributes such as height and DBH [134]. DBH is, for consistency, taken at 1.3m or 4.5ft from the ground on the uphill side of the tree [7, 135]. Small deviations from this standard are possible, such as in [118] where DBH measurements were taken at 1.4m, or at 1.37m in [134]. The single metric most commonly used for tree allometry is diameter [136], possibly because DBH measurements typically have less than 3% error [135]. Some of the equations in Table 2 as well as allometrics in [137] only use DBH for calculating biomass.

Height can be found in a number of ways from remote sensing data; however, DBH is more difficult to measure remotely. DBH can be estimated based on tree height and crown size with RMSE of 21.78% [79]. Work has been done to improve upon basic lidar height data for biomass estimations with strategies to extract crown dimension and other tree characteristics [138]. Utilization of full waveform lidar has improved biomass estimation; however, high resolution of the lidar and wide tree spacing is necessary to use these techniques for accurate results [139]. Also, waveform lidar was considered by [61] to be at a research stage and still unavailable for commercial and operational use.

There are studies that estimate biomass from height alone. One study of three sites, one of which is similar to the study site of this thesis (a temperate, coniferous forest in Oregon with Douglas-fir as the dominant and Western hemlock as second most important), achieved good correlation (R^2 = 84%, $P < 0.0001$) with equation 7 [140]. This general equation achieved an R^2 of 0.55 when its predictions were compared to biomass measurements for the Bartlett Experimental Forest in this study[109], which also applied a relationship found between biomass and the height at which 50% of the waveform

energy occurs (RH50) from lidar. This relationship yielded predictions with an R^2 of 0.61 [109].

$$\text{Aboveground Biomass (t/ha)} = 0.378 \times MCH^2 \quad \textbf{(7)}$$

where MCH is the mean canopy height (m)

Another height-biomass relationship is proposed in equation 8 [141] to find wood biomass for the trunk and branches with diameters > 7cm. It is said to perform best for fully stocked single species, even-aged forest systems [142].

$$\text{Standing Usable Wood Biomass (t/ha)} = 0.801 \times H^{1.748} \quad \textbf{(8)}$$

where H is top height of the 100 tallest trees per hectare

Estimating the total volume is the first step toward estimating the dry weight and carbon content of a tree [63]. Often wood in trees is characterized according to total volume of merchantable wood [20], which accounts for approximately 50% of the total volume, depending on size, species and merchantability standards [62]. There is, however a growing interest in estimation of total biomass and carbon [63].

A traditional mensurational approach is to cut the tree into pieces and determine the weight and volume of each piece [136]. This "destructive sampling" is the best way to get accurate measurements of biomass, as it is the most direct. Variations in the density of the tree stem are documented in [143], meaning that taking 'cores' from trees (less destructive than cutting down the entire tree) may not give representative results. Allometric estimation is preferable over destructive methods, as disturbance is avoided and the investigation of larger study areas is possible [144]. Thus many studies [134-137, 143-145] extrapolate the relationships which are discovered in a minimal amount of destructive sampling, for application over larger areas.

Excurrent means that most of the tree growth is in the main stem or bole or trunk, as opposed to in the branches; it describes a tree where the trunk is single and undivided, as in conifers [146]. The volume of softwood species in classic *excurrent* form can be closely approximated by text book mensurational methods [7]. As they typically have monopodial growth, strong apical dominance, and consistently tapered boles, most conifers yield allometric equations that accurately predict biomass [136].

Uncertainty, in biomass and carbon stocks largely results due to lack of species-specific allometric equations for each species [137]. There are many environmental variables which can effect tree growth, such as soil quality [147], elevation and drainage [148]. See Appendix A for tables in which some of these variables are documented for sites in the GVWD [118, 124]. Yet, in [135] the best performing general equation found was only marginally inferior to the species–site-specific equations. This was for 14 woodland species, mostly eucalypts, in Australia.

Allometric equations were developed in [134] for the following different components of *Pinus massoniana* trees in southern China: stem, branch, needle and root. Equations were developed using DBH, basal diameter (diameter at the ground), height, and combinations of these measurements, from the 197 destructively sampled trees across 20 site locations. Table 3 [134] shows, for each component of the trees, the percent of total tree biomass that it contains and the adjusted R^2 values for the fitness of two of the regressions that were done. The DBH equations performed better than those based on height alone. Not shown in the table is the high correlation between DBH and height ($R^2 = 0.849$, $p < 0.0001$) [134].

Table 3: Breakdown of tree components and fitness of the allometric equations for Pinus massoniana trees in study by Xiang et al. (2011).

Component	% of total tree biomass, range	Adjusted R^2 for height as independent variable of equation	Adjusted R^2 for DBH as independent variables of equation
Stem	28.85 to 89.96%	0.8793	0.9453
Branches	5 to 33.54%	0.6470	0.8544
Needles	0.02 to 35.7%	0.5125	0.7026
Roots	3.37 to 32.43%	0.7568	0.9022

Biomass predictions for large woody components such as boles and coarse roots tends to be better than for components such as foliage which is especially susceptible to weather, herbivores, and inter-plant competition [136]. The correlation coefficients in Table 3 demonstrate this tendency.

Equation 9:

$$DBH(cm) = -0.8565 + 0.546H(m) + 0.0226H(m)^2 \quad \textbf{(9)}$$

where DBH is in cm and H is height in metres, estimates DBH from height for conifer tree species based on thousands of trees measured in this research [118, 124]. The data used was from the plots in the southern Greater Victoria Watershed District, the primary study site for this thesis paper. Detailed tables of site characteristics and tree measurement statistics are located in Appendix A. Tian Han, Alex Song and Jackie Gour created the scatterplot of DBH versus height shown in Figure 16. This is how the regression was done and the equations were formed. The R^2 values are displayed underneath the equations for the trees in plot 5 from [118, 124] with five coniferous species. However, information was provided for plots 2, 5, 6, 12, 13 and 15, which contain 5417 more trees and 3875 more Douglas-fir trees (64% of the trees sampled in all the plots were Douglas-fir, but only 31% of plot 5 is Douglas-fir). With all trees for all of

these plots, the R^2 value for the purple line becomes 0.90 compared to 0.84 for the orange line. For only the Douglas-fir trees, across all of the plots, the R^2 of the orange and purple lines are both 0.84. Because individual tree allometrics vary (as in the cloud of points in Figure 16), the best results of estimating tree components are at stand or watershed scales [135, 143].

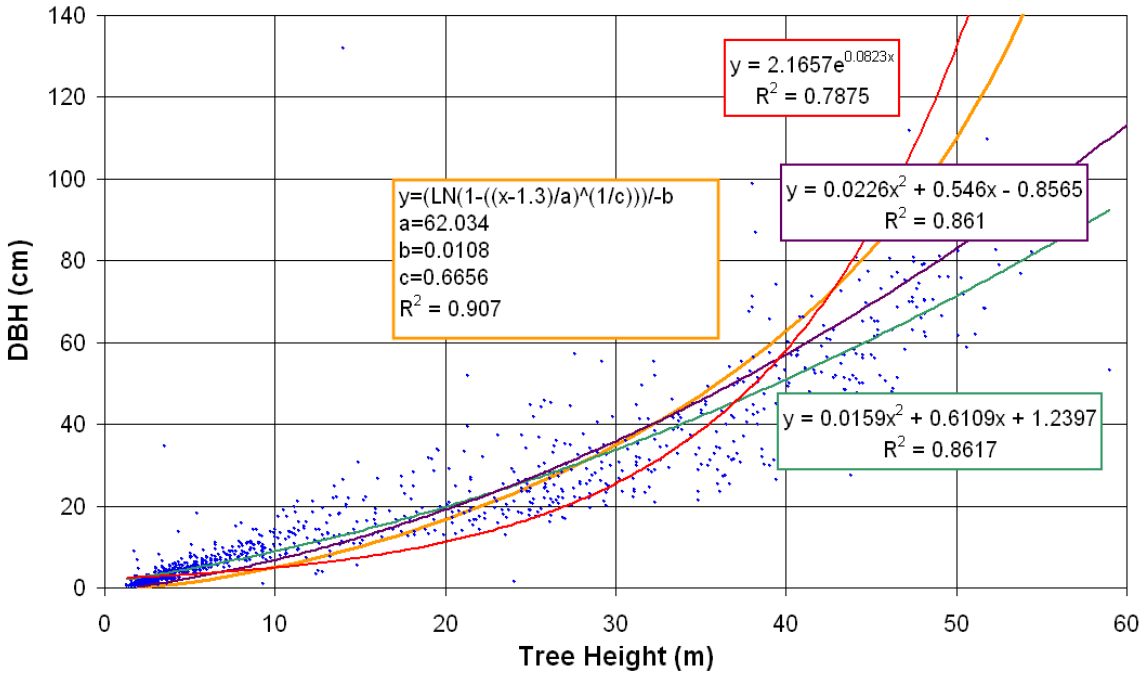

Figure 16: All trees in Plot 5 of southern GVWD. Best fit lines and two locally developed allometric equations (orange and purple) are plotted: red is the best fit exponential; teal is the best fit polynomial. In the equations, y is DBH in cm and x is the tree's height in m.

Another derivation of DBH from height is below in equation 10:

$$DBH(cm) = 3.3236 \times L(m) + 0.8521 \times H(m) + 3.8540 \quad \textbf{(10)}$$

for a plantation of Sitka spruce (*Picea sitchensis*) trees, where L is the crown diameter, assuming a circle, and H is height [79]. The best R^2 value comparing estimated DBH to measured DBH was only 0.40, with $p << 0.001$, when equation 10 was used with

Gougeon's tree crown identification algorithm [37] to find crown diameter and height [79].

4.2 Belowground Biomass

Xiang et al. (2011) found a close relationship between aboveground biomass (AGB) and belowground biomass (BGB) as well as allometrics for estimating root biomass from diameter and height measurements in their study of *Pinus massoniana* [134]. The regression fitted to the above and below ground relationship can be found in equation 11 [134]:

$$BGB = 0.1497(AGB)^{0.9986} \quad \textbf{(11)}$$

and has an R^2 coefficient of 0.9184 for n = 197. The averaged ratio of root to aboveground biomass for *P. massoniana* was 0.16 [134] and is in the same range found by others for the same species, but low compared to [149] for mixed species.

For paper birch (*Betula papyrifera*) and subalpine fir (*Abies lasiocarpa*), exponential relationships with DBH were found for estimating dry weight of root biomass [150]. The equations had R^2 values of 0.85 and 0.96 for subalpine fir and paper birch, respectively (n = 30 for each species) [150].

A study of small diameter (< 10cm DBH) *Albizia lebbeck*, *Acacia catechu* and *Dalbergia sissoo* trees produced very high R^2 values (0.8763 to 0.9661) for the root biomass equations that were developed [137]. The relationships found for percent contribution of above and below ground parts of all species to the total biomass were relatively similar (74.8–7.8% for aboveground and 13.8–25.2% for belowground) [137]. Only 25 trees were sampled for *A. catechu* and *D. sissoo* and 15 for *A. lebbeck* [137].

A total of 345 estimates of above and below ground biomass for softwood and hardwood species in cold temperate and boreal forests were used to form regression equations and the following relationships: softwood roots made up 18.9% of total tree biomass and the percentage of hardwood root biomass of total biomass ranged from 17.1% to 36.2% [149]. The goodness-of-fit of these equations and the standard deviations for percent of total biomass were not discussed in [149], but the equations were refined in a later study with an updated database [151]. The refined equations (12 and 13) are below [149, 151].

$$\text{Softwood Root Biomass (Mg/ha)} = 0.222 \pm 0.004 \times \text{AGB} \quad \textbf{(12)}$$

$$\text{Hardwood Root Biomass (Mg/ha)} = (e^{1.576 \pm 0.267}) \, \text{AGB}^{0.615 \pm 0.035} \quad \textbf{(13)}$$

The updated database had 340 and 103 pairs of aboveground and belowground figures for softwood and hardwood species, respectively [151], compared to the 260 and 85 original pairs. The R^2 values of the new equations are 0.799 for softwood and 0.562 for hardwood [151].

As more data is gathered, the equations with which belowground biomass is estimated improve [151]. Species-specific studies give different, more precise results: 13.8% compared to 17.1% lower bound for belowground contribution to total biomass [137, 149]; R^2 of 0.87 for *A. lebbeck* lateral root biomass equation versus 0.56 for general hardwood root biomass equation [137, 151]. Still, belowground biomass is subject to many biotic and abiotic factors that vary spatially and over time, including stand or tree age, tree species, soil temperature, moisture, and nutrient availability, as well as impacts by insects, fungi, and other soil organisms [151].

4.3 Optical Methods for Biomass Estimation

There has been some success using optical data to map biomass by extrapolating relationships between optical properties and ground truth through regression equations [89, 104, 146] or vegetation indices [1, 49]. There are several wavelengths that are known to be associated with physical properties such as biomass, chlorophyll, and liquid water content [146]. Tree proximity (which can be distinguished optically) can predict tree growth and size, which could help to boost the accuracy of biomass calculations, especially when there is not full lidar coverage [118].

Tree crown closure, the percentage of the forest floor or understory covered by the forest canopy, is a parameter in forest yield [146]. Like vegetation indices, this optical property (is the canopy sparse and open or closed) can be related to biomass. In [146], an exhaustive stepwise multiple regression algorithm in software called S-PLUS was used to mine the best bands of the AVIRIS data which corresponded to the ten crown closure classes. The classes were quantized by 10% from 0 to 100%. R^2 values of over 0.9 were found to relate sets of spectral bands to crown closure [146]. From there, biomass may be estimated using the relationship of crown closure to DBH or to bole biomass, which has been studied for coniferous species loblolly pine (*Pinus taeda*) and slash pine (*Pinus elliottii*) [152]. Needle area and bole biomass scatterplots had R^2 values of 0.80 for superior loblolly, 0.74 for average loblolly and 0.71 for slash pine [152]. Crown volume and DBH had R^2 values of 0.84 and 0.45 for loblolly and slash pine, respectively (n=24 loblolly pine family and n=22 for slash pine family) [152].

A vegetation index, ND45 (Normalized Difference), was used on Landsat TM (Thematic Mapper) data of Hinton, Alberta, to find biomass and aboveground carbon [1]. ND45 takes two Landsat bands TM4 and TM5 as shown in equation 14 [1]:

$$ND45 = 128 \times (TM4 - TM5) / (TM4 + TM5) + 128 \quad \textbf{(14)}$$

and then volume in m^3/ha is calculated with equation 15 [153]:.

$$\text{Volume } (m^3/ha) = -478.58 + 4.5041 \times ND45 \quad \textbf{(15)}$$

The timber volume was then multiplied by the wood density for biomass and half of the biomass was estimated to be carbon [1].

Another example of a vegetation index is the EVI (enhanced vegetation index), which uses bands of MODIS to gauge 'greenness' as a proxy for the amount of vegetation [49]. This index was used for change detection of global forest cover and the results were found to overlap very well with the validation data [49].

PLS (partial least squares) regression done on hyperspectral data with ground truth biomass data has achieved high correlations for GVWD forest: R^2 of 0.67 for the regression, resulting in an R^2 of 0.92 when predicted biomass was compared to VDYP (Variable Density Yield Prediction) model [153]; R^2 values from regression for AISA (2m) and AVIRIS (4m) data were over 0.76 for the lidar-derived biomass check plots, over 0.80 for VDYP plots [104], and over 0.88 for actual biomass predictions [105].

Optical data can be used to extrapolate biomass calculations made with scarcer data such as the height models from GLAS, to global scales [89] with the regression algorithms of Cubist [154]. R^2 correlations for the training dataset ranged from 0.56 to 0.77, with a mean of 0.67, and were similar for the testing dataset, with a mean R^2 of 0.57 [89]. SWIR reflectance based formulae have been found to be more effective than vegetation indices like NDVI (normalized difference vegetation index) for correlating mean height of Scots pine with optical data (yielding R^2 values of 0.65-0.70), possibly

due to saturation of the red band as forest density grows [90]. The ND45 index saturates with biomass values greater than 300 t/ha [153].

While goodness-of-fit for optical estimations with ground data can be low, such as the correlation between ND45 and the Canadian National Forestry Inventory with R^2 of 0.35 [1] for 10km by 10km cells, or given qualitatively as with [49], optical methods of forest monitoring are useful for change detection over time, especially of forest area.

4.4 Classification Algorithms

Ideally libraries containing the spectra of many materials could be used to identify and classify the sensed material. However, this is made difficult due to differences in angle, atmosphere, illumination and the variability of spectra within a class. It is best to have a large number of training areas spread out through the image, with accurate measurements and identification of the materials at that location. A goal of classification algorithms used in remote sensing is to achieve high accuracy with as little training data as possible.

Classification algorithms are frequently split into supervised and unsupervised categories [2, 155-158]. Unsupervised classifications do not require training data to start and use the intrinsic properties of the data to cluster pixels with similar spectra. The result must be labelled manually with training data or through matching with libraries or through a supervised classification. Because this category does not end up giving the clusters class labels, it is referred to as clustering in this thesis. Classification refers to supervised classification where training or truth data is used to prepare the classification rules and parameters. Then the algorithm is run on the full data set, using the rules that have been established. The result can be tested with the same training data or, for less bias, with truth data which were not used to train the algorithm.

A simple example of a classification algorithm is the minimum distance classifier. The training data are used to establish mean spectra for each class. Then each pixel of the image is labelled with the class to which its spectral signature is the closest. There are different ways to quantify the distance or difference between spectra. Spectral angle mapper, shown in equation 16 [159]:

$$\Theta(x,y) = \arccos(\langle x,y \rangle \div \|x\|_2\|y\|_2) \; ; \; 0 \leq \Theta \leq \pi/2 \qquad \textbf{(16)}$$

where x and y are vectors representing spectra, gives the angle between the spectra, without regard to magnitude, such that this method is invariant to differences in illumination and the angular orientation of the targets [159]. The Euclidean minimum distance is another measure, which is simply the two-norm of the difference between two spectra: $\| x - y \|_2$, where x and y are vectors of the reflectance values of a spectral signature, and the difference of these vectors is subject to a two-norm or Euclidean norm [159].

The most common supervised classification method used with remote sensing data is maximum likelihood classification (MLC) [157, 158]. Classifiers like the Gaussian MLC that take advantage of second order statistics (e.g. co-variance) of the classes are very powerful for discrimination, because in higher dimensions the second order variations can contain more information than first order variations (e.g. means) [160, 161].

MLC is based on Bayes' theorem, shown in equation 17 [162]:

$$p(a|b) = p(b|a)\, p(a) / p(b) \qquad \textbf{(17)}$$

where p(a) is the probability of a; and p(a|b) is the probability of a, given b. Equation 18 [158] is more specific to classification of a multispectral image:

$$p(\omega_i|x) = p(x|\omega_i)\, p(\omega_i) / p(x) \quad \textbf{(18)}$$

where x is a vector or position in spectral space; ω_i is the spectral classes for the image where i = 1, … the total number of classes; $p(\omega_i|x)$ is the probability that the class ω_i is the correct class for x; p(x) is the probability of finding any class at position x; $p(\omega_i)$ is the probability that the class ω_i appears in the image; and $p(x|\omega_i)$ is the probability of observing x in the class ω_i. If classes are assigned equal probability, the likelihood that a pixel with spectra, x, belongs to any class, ω_i, depends on $p(x|\omega_i)$ [2].

Training samples for each class are used to estimate the parameters of a probability density function (PDF) for each spectral class: $p(x|\omega_i)$. The training will typically form clusters, as shown in Figure 17. In the supervised learning stage, MLC estimates the mean and co-variance matrix from the training in order to define the PDFs [157], seen in Figure 18. Use of normal (Gaussian) distributions is most common, some believe that accuracy is not overly sensitive to violations of the assumptions that classes are normal [158]. The equation for a multidimensional normal distribution is given in equation 19 [158]:

$$p(\boldsymbol{x}) = \frac{1}{(2\pi)^{N/2}|\boldsymbol{\Sigma}|^{1/2}} \exp\{-\frac{1}{2}(\boldsymbol{x}-\boldsymbol{m})^t \boldsymbol{\Sigma}^{-1}(\boldsymbol{x}-\boldsymbol{m})\} \quad \textbf{(19)}$$

where **x** is a spectrum vector in N dimensional space, ***m*** is a mean spectral vector for a class, and $\boldsymbol{\Sigma}$ is the covariance matrix for the distribution of that class.

These PDFs are used to calculate likelihood of spectral class membership for each pixel, with equation 18. The class with highest computed likelihood is assigned to the pixel in the output classified image (i.e. x is an element of the class ω_i if $p(\omega_i|x) > p(\omega_j|x)$

for all $j \neq i$). By the end of the classification, all pixels should have either a class label or be labelled as unknown.

Advantages of MLC are that it is mathematically tractable, statistically desirable with a well-developed theoretical foundation and has proven performance with many land cover types and sensors [157, 158]. It is better for classification of high-dimensional data than less complex classifiers such as minimum distance [160, 161]. A disadvantage is that MLC tends to overemphasize classes which are well-represented in training and underemphasize less frequent ones [131].

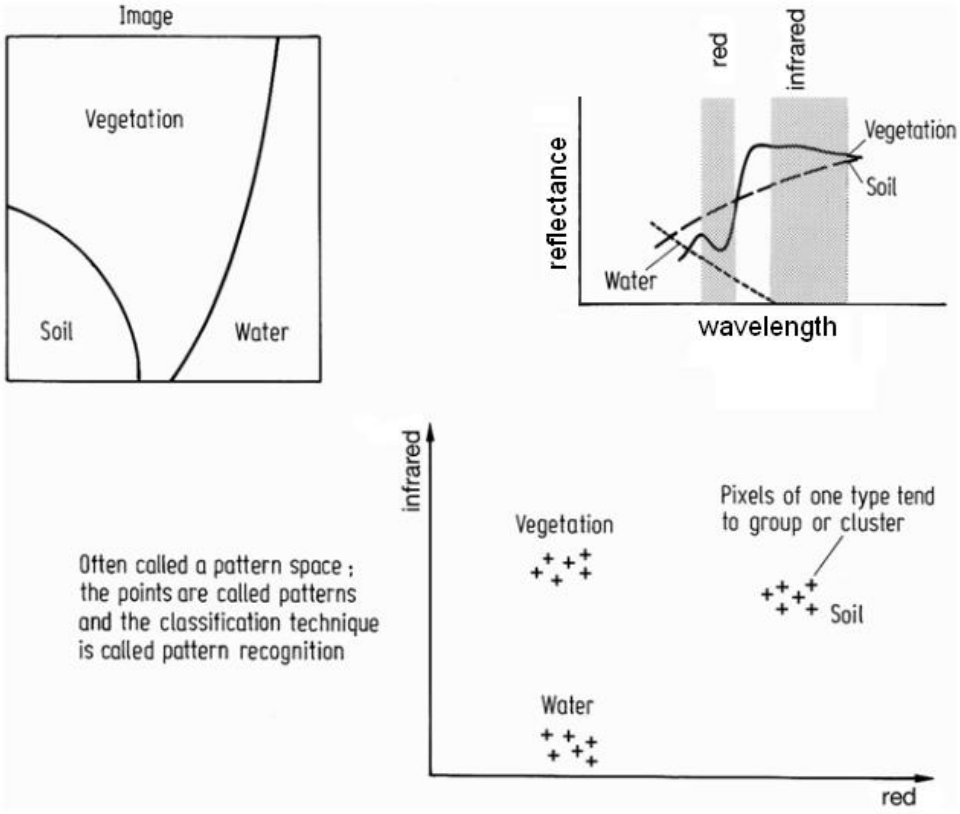

Figure 17: Illustration of a two-dimensional multispectral space showing its relation to the spectral reflectance characteristics of ground cover types. [158]

Other supervised classifiers include support vector machines (SVM) and artificial neural networks (ANN).

In the training stage, SVM classifiers find a plane which separates two classes, with the maximum margin of distance between the classes [158]. The data may need to be transformed into a higher dimensional feature space in order to find such a plane [158]. Two common kernels used for transformation are the polynomial kernel (equation 20) and the radial basis function kernel (equation 21)[158]. SVMs are binary classifiers which must be combined through multiple runs in order to classify with multiple classes [163].

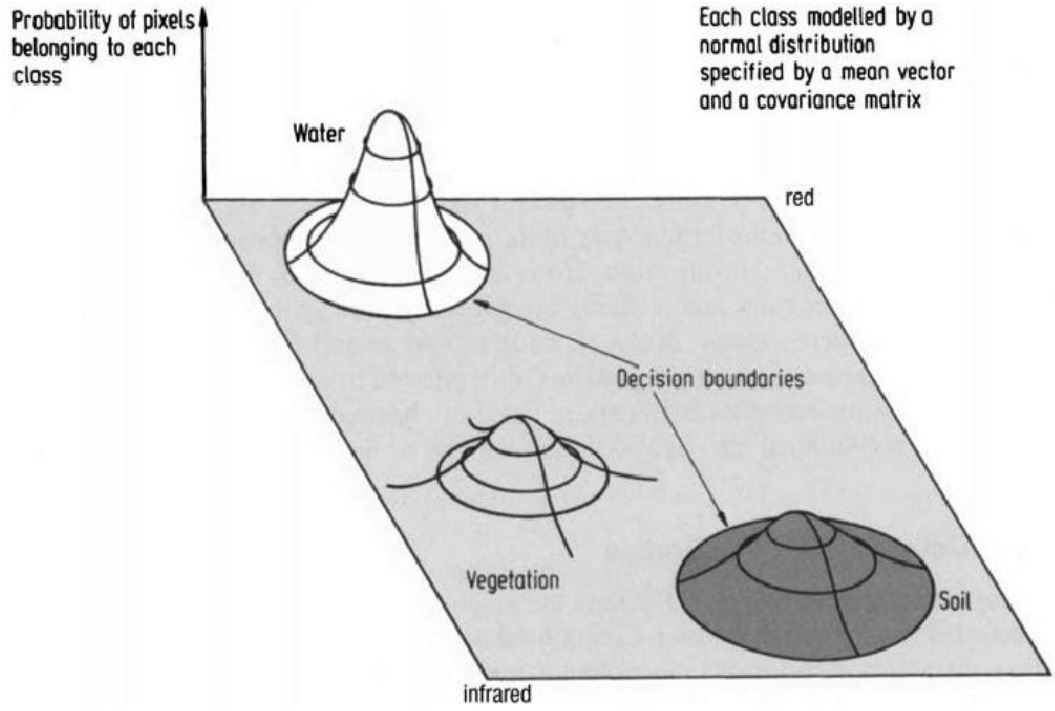

Figure 18: Two dimensional multispectral space with the spectral classes represented by Gaussian probability distributions. [158]

$$k(x_i,x_j) = [(x_i)(x_j) + 1]^{\rho} \quad \textbf{(20)}$$

where ρ is a constant which must be chosen

$$k(x_i,x_j) = e^{-\gamma||xi - xj||^2} \quad \textbf{(21)}$$

where γ is a constant which must be chosen

The neural network formed in training an ANN consists of layers of nodes connected by weight parameters, which form a directed graph from input nodes (the spectra) to output nodes (a value which can be mapped to a class label)[158, 164]. A study specifically comparing the conventional MLC to ANN, suggests that ANN gives superior classification results [165]. In another comparison of classifiers ANN achieved higher accuracies than MLC for remote sensing data, but was more difficult to apply and took more time to train [155]. ANN is more sensitive to outliers in the training data than statistical classifiers such as MLC [158]; it is even more important that the training areas are representative of the entire image.

Accuracy of a completed classification is generally given by use of a confusion matrix, as in Table 4, where overall accuracy is the area-weighted average of the diagonal entries or the total correctly classified testing area over the total testing area [155].

Table 4: Confusion matrix from a Maximum Likelihood Classification of AVIRIS data over D4S2 with percent accuracies per class (aggregated) and an overall accuracy of 80.4%

Class\Truth	Water	Swamp	Hemlock	Land	Cuts	Shrub	Red Alder	Pine	Douglas-fir	Total
Water	99.99	0.12	0.00	0.00	0.00	0.04	0.27	0.00	0.00	9.73
Swamp	0.00	98.58	0.07	0.78	0.00	0.07	0.67	0.36	0.35	6.37
Hemlock	0.00	0.00	42.79	0.00	0.00	16.95	2.89	7.77	4.04	5.54
Exposed Land	0.00	0.00	0.00	89.65	0.00	0.02	0.00	0.00	0.03	0.17
Recent Cuts	0.00	0.00	0.00	0.00	99.68	0.00	0.00	0.13	0.07	3.08
Shrub	0.00	0.00	0.00	0.00	0.00	60.58	0.00	0.08	10.22	8.81
Red Alder	0.00	1.17	1.87	7.03	0.00	11.45	95.19	0.00	1.34	3.74
Lodgepole Pine	0.00	0.00	2.53	0.00	0.00	0.00	0.00	60.07	4.00	6.96
Douglas-fir	0.01	0.13	52.74	2.54	0.32	10.89	0.98	31.59	79.96	55.60
Total	100.00	100.00	100.00	100.00	100.00	100.00	100.00	100.00	100.00	100.00

Accuracy can be hurt by “overfitting”, which is when a classifier becomes too sensitive to the specific training data and its noise to effectively classify other areas. It can be

eliminated through noise reduction or an increase in training data. Training samples that are obtained from spatially adjacent regions may not be good representatives of the samples of the same class that might exist in other regions of the scene [161]. It is difficult and expensive to get enough training data that is representative [132, 161]. The more examples of the variation in spectral signatures within a class, the less likely it is for the classification to make omission errors (exclusion of an area from a class to which it belongs), which would hurt producer accuracy. By using very specific classes, such as Douglas-fir Aged 200+ years with an open canopy, to train the classifier and then aggregating the classes by species after the labelling, the overall accuracy of the classification will increase. Compare, for example, the aggregated results of Table 4 (overall accuracy of 80.4%) to those of the non-aggregated classes in Table 11 in Appendix B (overall accuracy of 63.9%). The different accuracy measures for the non-aggregated and aggregated classification results are in Table 12 and Table 13, respectively, in Appendix B.

4.5 The Curse of Dimensionality and Principal Components Analysis

As more measurements are taken in an area such that more information is known, the ability to classify the area and identify targets should improve in accuracy; however, with enough measurements, along with noise and errors present in the data, the classification accuracy will plateau and actually decrease: a problem referred in the literature as the Hughes phenomenon or curse of dimensionality [133, 161]. Like multispectral data [166], hyperspectral data suffer from high correlation in adjacent bands and therefore contain similar information [133, 167].

The high dimensionality of hyperspectral data limits the application of classifiers because of the demand for a large number of training samples. It is well known that when the ratio of the number of training samples to the number of feature measurements (number of bands) is small, the estimates of the discriminant functions are not accurate and classification results may not be satisfactory [161]. These often result in unstable covariance matrices which in some cases can be singular [2, 132, 167]. As more measurements are taken, the distance between the classes grows, but so do the distances between members of the same class [160]. SVM classifiers exhibit low sensitivity to the Hughes effect due to their geometrical nature which takes advantage of the between-class distance, without requiring density estimation like some statistical classifiers [163].

Experimentally it is often observed that for finite training sets, when the number of measurements is increased, the performance of the classifier first improves, later reaches a peak, and finally falls off [161, 168, 169]. The value of optimal measurement complexity increases with training size [168]. Experiments with several classifiers and training sizes find that accuracy depends on sample size, type of classification rule, class-conditional distributions of the patterns of the training data and the "effectiveness of features and their ordering" [169]. For linear discriminant functions the optimal number of bands are N/2 – 1 for N training patterns [158, 169]. For quadratic discriminant functions, significantly lower than N/2 -1 bands are required, but the number still increases with N [169]. One reference suggests that dimensionality reduction may be needed if the number of bands exceeds 10 [158], while an implementation of maximum likelihood classification will function with up to N-1 bands [2, 158]. Hughes calculated accuracy of statistical pattern recognizers for 2-1000 design patterns and found that only

23 measurement values are significant for 1000 sample patterns [170]; he suggests that mapping by measurement selection, combination and reduction be investigated to aid in finding a smaller, more optimal measurement set to increase classification accuracy[170]. The most common strategy to increase the ratio of training samples to measurements is with feature extraction [156, 171]. Long training and classification times are another reason for reducing the number of bands used [2]: a maximum likelihood classification with B bands and T training sets requires $(B^2+B)\times T$ multiplications and $(B-1)\times(B+1) + 2\times B$ additions to compute each B-tuple [157].

One method for feature extraction, used by [161], [155], and [156] is to use bands which will maximize the Bhattacharyya distance, ß, between classes, maximizing the potential for discrimination. Bhattacharyya distance or divergence is defined in equation 22 [156] for the distance between two classes' probability density functions:

$$ß = -\ln \int [p(x \mid A)p(x \mid B)]^{1/2}\, dx \qquad \textbf{(22)}$$

where x is a new point's spectrum and p(x | A) is the probability that the new point is in class A It may require less computation to evaluate than error probability [156]. Distances from 0 to 1 are very poor separability, 1 to 1.9 are poor, and 1.9 to 2 are good [155]. With ß=infinity meaning that the PDFs do not overlap at all and ß=0 that the PDFs are the same [156]. In [161], the bands were ranked by ß and as more bands were added (from the largest ß values to smaller ones), classification accuracy rose sharply, peaked and declined, showing the Hughes phenomenon.

A principal components analysis (PCA) is a common tool to reduce dimensions of data [166], whether for compression, enhancement of remotely sensed data or for the purpose of visualization. PCA is a process by which data is sorted into orthogonal components,

beginning with the components with the most information or highest eigenvalues of the covariance matrix [172]. The eigenvalue decomposition (see equation 24) is done on the covariance matrix of the image or samples from the image, shown as S_x in equation 23 and 24[159].

$$\mathbf{S}_x = \frac{1}{N}\sum_{n=1}^{N}\left(\mathbf{x}(n)-\mu_x\right)\left(\mathbf{x}(n)-\mu_x\right)^T \quad \textbf{(23)}$$

where x is the sample which has size N, x(n) is a particular point in the sample, and μ_x is the mean vector of the whole sample set

$S_x = U\Sigma U^T$ **(24)**

where U is a unitary matrix of eigenvectors and Σ is a diagonal matrix of eigenvalues which decrease in value along the diagonal. S_x is the product of U, Σ , and U transform.

Pre-multiplication by a subset of the rows in U^T moves x to a new system of decorrelated variables oriented along the eigenvectors in U [159]. The original data exists as a linear combination of the components: a projection onto new axes which are ordered by decreasing variance. There is the same number of dimensions in the result as in the original data, and none of the data is lost, though it is located predominantly in the first few components. The effective dimensionality of the data can be estimated by counting the non-zero eigenvalues [159]. In classifications of hyperspectral data or other data with many dimensions and notable noise, a PCA is often performed and a subset of the components is taken as part of the feature extraction. PCA possesses optimal properties for retaining the energy in random signals, but cannot guarantee that the resulting transformation will preserve the information that aids in detecting low probability objects

[159]. This may be possible by performing a PCA using the covariance from samples of the low probability targets.

A maximum noise fraction (MNF) [166] or minimum noise fraction (adapted from [166], for ENVI [173]) is the use of PCA and noise whitening to maximize the covariance of the noise over the signal covariance [159]. An MNF followed by an inverse MNF will return the data to its original data space [173]. By applying an MNF to a hyperspectral image, it reduces between-channel correlation with a variance loss of < 1% [167]. MNF has the advantage over PCA of additional noise removal, because PCA eigenvectors are not always ordered by image quality [166]. By using only the first MNF bands, with the highest eigenvalues, much noise is separated from the data [109].

4.6 MNF Band Experiment

As part of a study using airborne hyperspectral data, the same classification was run on the first 12 components of the MNF result and the first 17. The resulting accuracies were similar and the agreement within classes was high (at 86.83%) with the twelve component overall accuracy better by 1.0% [105, 174]. A more thorough experiment with airborne hyperspectral data follows below.

Data from the two study locations in the GVWD (see section 2.6), acquired with the University of Victoria's AISA sensor and with NASA's AVIRIS sensor, were run through an MNF transformation. Increasing subsets of the resulting MNF bands were run through maximum likelihood classifications on the same training data, and their overall classification accuracies are shown in Figure 19 and Figure 20.

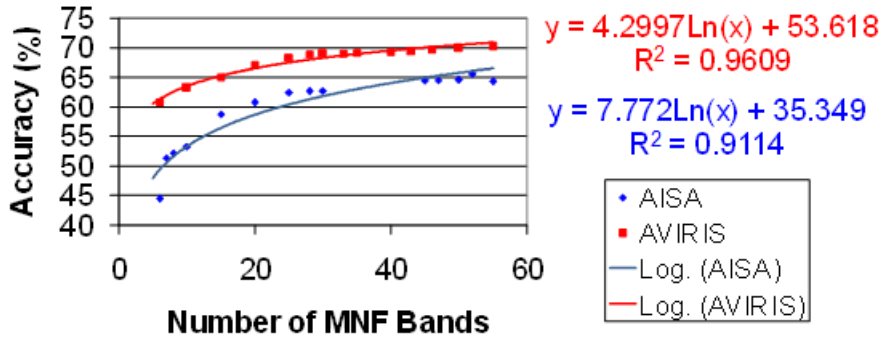

Figure 19: Classification accuracy for the D4S2 study site, for a number of MNF (minimum noise fraction) bands used in a maximum likelihood classification. The same training areas were used for AISA and AVIRIS data. The low accuracies are due to non-aggregated classes (different densities and ages of Douglas-fir). In the equations, y is classification accuracy and x is the number of MNF bands.

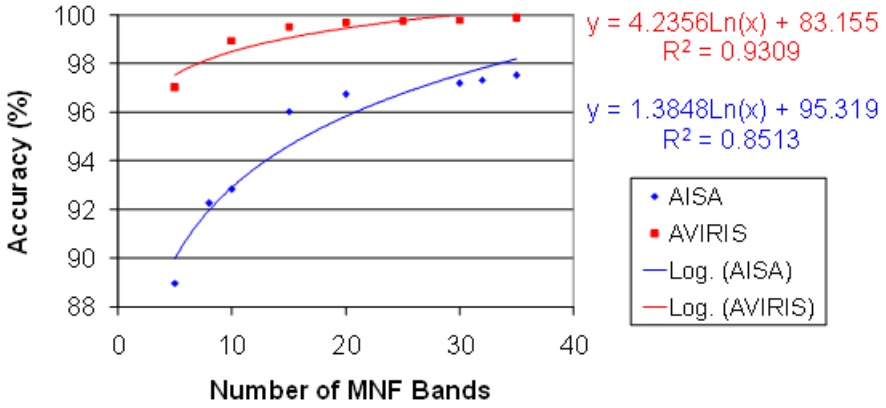

Figure 20: Classification accuracy for a number of MNF (minimum noise fraction) bands used in a maximum likelihood classification of the Rithet study area. The same training areas were used for AISA and AVIRIS. In the equations, y is classification accuracy and x is the number of MNF bands.

In an earlier study, AISA and AVIRIS SNR (signal-to-noise) was compared. It was found that AVIRIS had on average over all wavelengths, 19.9% more signal relative to AISA, though they were comparable in the VNIR [104, 105]. The eigenvalues from an MNF transformation on AISA and AVIRIS images of GVWD are shown in Figure 21, at different spatial and spectral resolutions for AISA, which has visibly less variance than

the AVIRIS sensor. The AVIRIS imagery acquired after 1999 was assessed by JPL (NASA's Jet Propulsion Lab) as having a SNR of over 1000:1 at 600nm[175], which is based on a 50% reflectance target at 30° solar zenith angle [125, 176]. After the valuable data is rearranged into the first MNF bands, it is reasonable to expect that more bands will continue to increase classification accuracy for AVIRIS than for AISA because the AVIRIS sensor has a higher signal-to-noise ratio.

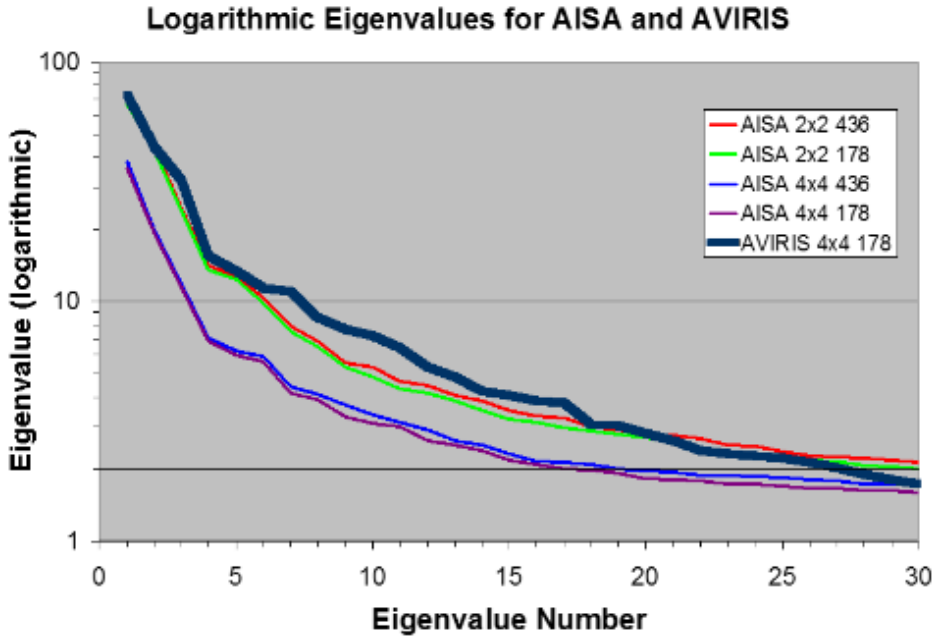

Figure 21: Eigenvalues from the MNF transformations of AISA and AVIRIS data over GVWD. The AVIRIS data which was used had 4m spatial resolution and 178 bands (after water absorption bands were removed). The AISA data was originally 2m with 436 channels, after the removal of water absorption bands, and was resampled both spectrally and spatially to match AVIRIS. Four variations of AISA are shown in the graph. [105]

4.7 Spectral Unmixing

Keshava and Mustard [159] define spectral unmixing to be "the decomposition of a mixed pixel into a collection of distinct spectra , or end members, and a set of fractional abundances that indicate the proportion of each end member." Decomposing a pixel into

its constituent parts can glean much more information about the land cover. For data with low spatial resolution, it could make a large difference to forest area if pixels which are classified as forest contain small fractional areas with trees.

Unmixing assumes that a pixel's spectrum is a combination of end members or pure spectra. The linear unmixing model (see equation 25 [167], below) finds a linear combination of the end members which can recreate the pixel's spectrum. Two constraints are often put in place for the fractional abundances: the sum-to-one constraint and the non-negative constraint [167]. The sum-to-one constraint ensures that the end member fractions in a pixel sum to 100%, which requires that all end members are known [167]. The non-negative constraint ensures there are no negative fractions of end members. In a study comparing unconstrained, partially constrained and fully constrained unmixing algorithms with AVIRIS hyperspectral data of British Columbia forest, the fully constrained algorithm had the best performance [167].

$$\boldsymbol{r}(x,y) = \mathbf{M}\boldsymbol{f}(x,y) + \boldsymbol{\varepsilon}(x,y) \quad \textbf{(25)}$$

where $\boldsymbol{r}(x,y)$ is the n-band spectrum of the pixel at co-ordinate (x,y); $\boldsymbol{f}(x,y)$ is a column vector holding the fractions of p end members; $\boldsymbol{\varepsilon}(x,y)$ is a column vector representing the additive random noise for each of the n bands; and $\mathbf{M}$ is an $n \times p$ end member spectral matrix

Nonlinear unmixing should be used for end members which are in an intimate association such that the end member materials are mixed on spatial scales smaller than pixels [159]. Nonlinear mixing effects have been associated with the transmission and scattering of green leaves [177].

Like classification, spectral unmixing can require close supervision and several steps. For example, using spectral clustering methods to isolate and remove shadow, or designate shadow as an endmember [177] may improve the results. In ENVI software, unmixing results that contain negative fractions or ones which are greater than 1 indicate impure end members or a shortage of end members [173].

5 Results and Validation of Aboveground Carbon Maps

There are a number of resources with which to compare the biomass maps and values generated by the automated system: theoretical bounding values (minimum and maximum expected biomass), files and documentation from past work in these study areas done by scientists in the Pacific Forestry Center [104, 105, 110, 125], high-level and plot-level NFI (Canadian National Forest Inventory) information and VDYP (Variable Density Yield Projection) results for much of the study areas. Many of these resources and those in the literature, report in terms of biomass, not in carbon. Carbon content of wood biomass depends on species, but is often assumed to be 50% of the oven-dried biomass, by mass [1, 58, 62].

5.1 Error Calculation

The biomass and carbon maps made from the process outlined in the next chapter will have errors due to the input accuracies of: height information, stem density, species classification, image co-registration, and allometric equations. The accuracy of the height data hinges upon the accuracy of the lidar instrument and subsequent processing. An investigation of lidar accuracy can be found in section 2.4. Airborne lidar data of forests is known to underestimate the height of trees. This underestimation increases with tree height, and appears to vary by species. For Douglas-fir dominated forests on Vancouver Island, lidar is accurate to within 6% of height [95]. The examples in this thesis have been calibrated for underestimation, such that the true heights of the trees should be reflected in the CHM, instead of only 88-95% of the height [95, 96, 178].

The accuracy of the tree count and location information from which the (SDM) stem density model is derived, depends on the algorithm used. Some of these algorithms are explained in section 2.5. The algorithm used in the experiments shown here, is Loos'[39],

which finds 80% of the trees [179]. This underestimation has also been corrected. In general, such algorithms will find dominant trees, so those which are not found are more likely to be smaller and have less biomass. The correction does not generate new trees in new locations, rather, it scales the SDM by a factor of 1.25 (see the process for deriving this factor in equation 26) This correction assumes that the missed trees are representative of the found trees, in height and species.

$$N' = N \times 0.80$$

$$N = N' \div 0.80$$

$$N = N' \times 1.25 \quad \textbf{(26)}$$

Where N is actual number of trees and N' is number of trees identified and counted by the Loos algorithm [39].

For the D4S2 area, calibration of the CHM and of the SDM caused the average biomass to double, though the result was still an underestimate compared to previous work [104, 105], VDYP and broad NFI estimates (see Figure 22).

Aggregated forest classification accuracies from Gaussian maximum likelihood classifiers were all greater than or equal to 80%, with higher accuracies for AVIRIS data (≥86%). By performing multiple classifications and masking the non-forest (setting the non-forest pixels to 0 or a non-data value to ignore the area in the next classification), accuracy was improved. For example, using this method, AVIRIS data over the GVWD had tree species classification accuracies as high as 93.2% [180]. Depending on the particular classification, there may be confusion between tree species or a misclassification of forest as non-forest. Errors caused by between species confusion can be conceptualized in Figure 23. Given a particular tree height, note the differences in

biomass for the different species. The height of the tree makes a large difference; for a lodgepole pine tree that is misclassified as a hemlock tree, at a height of 2m there is a loss of 28kg, at 18m there is a gain of only 2kg and at 32m there is a gain of 288kg. In the case where forest is misclassified as non-forest, all of the carbon for the misclassified area will be ignored. Fortunately, in the confusion matrices in Table 4 and Table 11, the confusion between species is more prevalent than the confusion between forest and non-forest classes, except for shrubs, which have significant mixing with the forest classes. The classification of non-forest as forest would make little difference to the carbon totals if the area has low height and stem density.

The allometric equations used for the species in the two study areas (see Table 2), all had high R^2 values reported in the publications from which they came. All of the equations are for total aboveground oven-dry biomass. The equation for red alder, the deciduous tree, had an R^2 of 0.99 for 41 trees in BC [129]. From the same source, allometrics for western hemlock in BC had an R^2 of 0.98 (n=70) [129]. This source also has equations for coast Douglas-fir (R^2= 0.99, n=49, standard error of the estimate SEE=69.27kg) and lodgepole pine (R^2=0.93, n=98 SEE=62.58kg). The lodgepole pine equation used in [105] and [104], was for trees in the Yukon Territory (R^2=0.9811, n=149, SEE=5.2402) [130]: a higher correlation found with a greater number of trees, but in a higher latitude. The Douglas-fir equation which was used in past publications on these study sites had an R^2 of 0.97 for 60 trees in BC (SEE=0.272, correction factor=1.04) [128]. The standard error of the estimate (SEE) for the equations which were chosen for Douglas-fir and lodgepole pine was much smaller than for those given by Standish et al. in [129].

Because all of the allometric equations above rely partially or fully on DBH, each is subject to the error in the height-to-DBH approximation equation (equation 9 and shown as the purple line fit in Figure 16 on page 43), which had an R^2 of 0.86 for all tree species in a plot which is local to the study areas. Section 4.1 discusses the R^2 values for the height-to-DBH equations as the species and number of plots is changed. Equation 9 and others in Figure 16 were developed to fit forest measurements from studies which had plots in the GVWD [118, 124]. The accuracies of these equations vary depending on tree species. Equation 9 was the best fit equation (R^2 of 0.90) for measurements of all species, from all plots in the GVWD; it was used to find DBH for all of the forest species in both study areas for carbon mapping.

There may also be errors due to the temporal differences in data acquisition. Studies in the GVWD conducted by the Canadian Forest Service have shown that trees having a DBH of over 30cm will seldom grow more than one millimetre per year in DBH [181]. "Annual volume increments per hectare in Douglas-Fir under the environmental conditions present at the GVWD range from 10 percent of standing volume at age 24 years, to about 5 percent by age 40, declining to zero after maturity is reached" [123]. Therefore, there may have been notable changes in the biomass of younger stands from the time of AVIRIS acquisition (2002) to AISA acquisition (2006) or from the time of the orthophotography (2007) and the CRD field work (1997 to 2005) [105].

In [182], biomass estimation methods using remote sensing were reviewed and categorized: the direct remote sensing methods (DR), such as regression, and combine and assign methods (CA) where biomass values are given to appropriately classified areas according to their attributes. It was noted that DR approaches would generally

underestimate biomass compared to CA. The research for this thesis found the opposite for the study areas, where PLS regression is DR and the classification and allometrics method is CA.

5.2 Sample Values

In the first inventory of forest biomass for all of Canada, published in 1985, it is stated that Canada's forest biomass exceeded 26 billion oven-dried tonnes and was 411 million hectares in area; this only includes forests for wood fibre production and harvesting [62]. The national average for forest biomass was 62 tonnes per hectare (t/ha), and was the highest in British Columbia at a provincial average of 178 t/ha on productive forest land with the highest average for individual forest types of 1100 t/ha [62].

In the current National Forest Inventory (NFI), most of Vancouver Island is shown to have an average of over 150 tonnes per ha of forest biomass (see Figure 22). Table 5 was populated with information from NFI plots in Southern Vancouver Island and shows the difference that height and stem density can make to average biomass. These figures can be compared with calculations done with allometric equations and the forest information. The following calculations will be based on the data from plot number 2 of Table 5. Using equation 7 for trees of 22.2m in height gives a resulting aboveground biomass of 186.3 t/ha. The equation was developed for mean canopy height, not full tree height, so one might expect an overestimation, which is not the case. Equation 8, gives 181 t/ha of usable wood biomass (for branches with diameters > 7cm) for plot 2. Ideally the height of the tallest 100 trees/ha would be used for height in equation 8, so this underestimation is justified. The Douglas-fir equation that was used for the maps in this thesis, from Table 2, can calculate the biomass for the 725 individual trees in a hectare, at 22.2m. First, DBH is

derived with equation 9 (giving 22.4cm) and then biomass in kilograms (209.5kg/tree). The result is 152 t/ha, which is also an underestimation compared to the NFI field data.

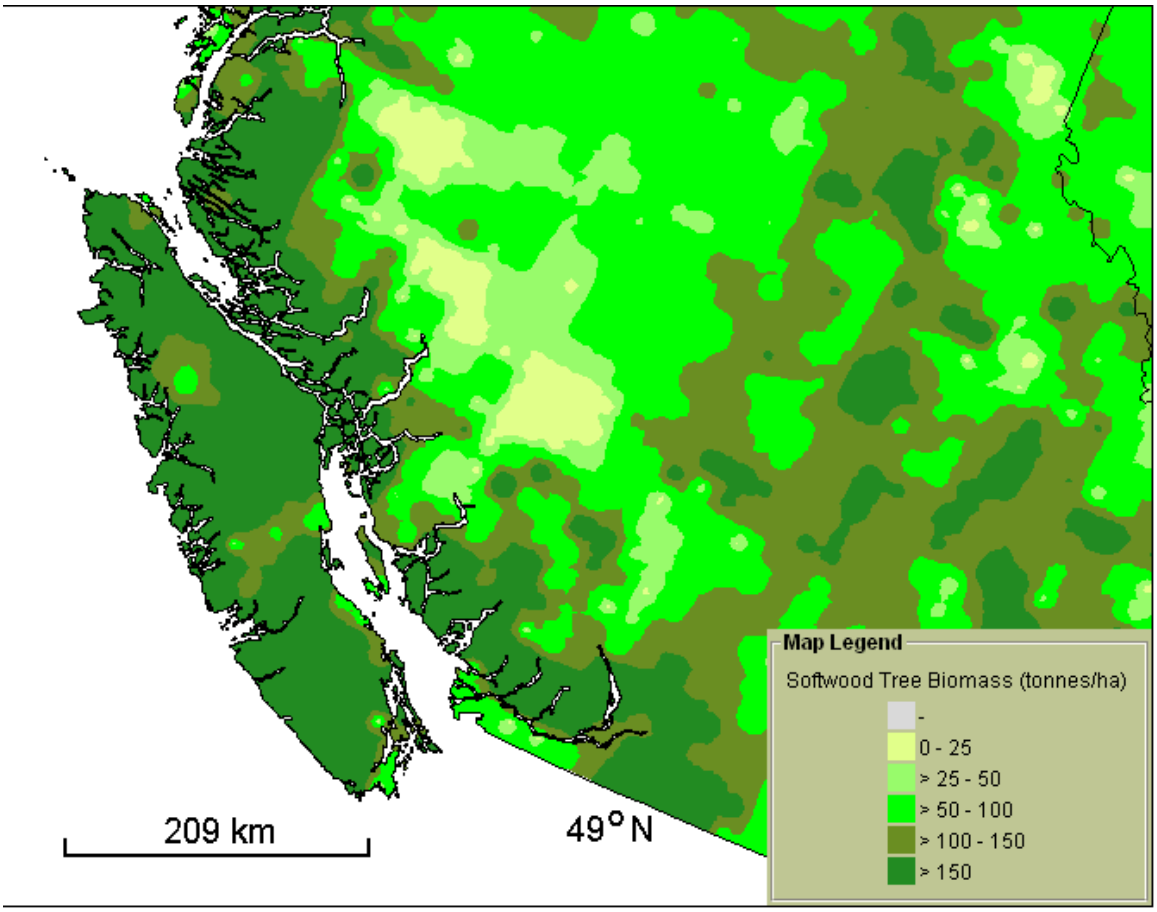

Figure 22: Softwood tree biomass for Vancouver Island and southern British Columbia, Canada, according to Canada's National Forest Inventory, 2006. [183]

Using the allometrics in Table 2, the value found for average biomass through the D4S2 study area was 41.8 t/ha. Given the lower stem density (223.4 stems/ha) and the average tree height of 14.5m in D4S2, this biomass average is consistent with the values in Figure 22.

Table 5: Plot statistics for three Douglas-fir dominant sites in Southern Vancouver Island.

Plot Number	**1**	**2**	**3**
Stem density (stems/ha)	125	725	625
Average height (m)	6.4	22.2	10.9
Percent Douglas-fir (%)	100	77.7	62.2
Age (years)	16	40	41
Average biomass (t/ha)	7.04	268.58	65.89

5.3 Larger Scales

Many of the studies discussed have been focussed on relatively small areas by necessity [183], yet estimates are usually required at larger spatial scales: for example, the UNFCCC requires that carbon sources and sinks must be reported at aggregated national scales [184]. Dean et al. [183] assert that "the need to 'scale' measurements and observations from the level of unit-area, patch or stand, up to landscapes, regions and beyond is a challenge in the field of carbon accounting."

Another reason to scale up the process is that lower spatial resolution than lidar for height information is more economical [185, 186]. At a lower resolution, individual trees cannot be delineated, with the consequence that tree top location and stem count are out of reach. Different metrics and equations need to be used to get average biomass if the number of trees cannot be counted. There are metrics such as the equation 7 and equation 8 which use only height. However, equation 8 uses the height of the tallest 100 trees per hectare [141]. To use the equation properly, either the heights of the individual trees must be known, or a relationship between average height and the height of the tallest 100 trees must be found. Equation 7 was developed using a full waveform lidar which can measure the forest profile and estimate the mean canopy height [140, 187]. Full waveform airborne large footprint systems are still experimental and generally not commercially

available outside North America [188], although this limitation was addressed to some extent by spaceborne lidar platforms such as the Geoscience Laser Altimeter System (GLAS) on NASA Ice, Cloud, and land Elevation Satellite (ICESat) and other full waveform lidar data (e.g. SLICER and LVIS) which show considerable promise for forest characterisation [189].

The GLAS on ICESat sampled approximately 65-m-diameter footprints every 172 m, and had elevation retrieval precision and accuracy of 2 and 14 cm per shot, respectively [190]. ICESat had a laser operating at 40 Hz and an analog detection system to record reflected laser energy in the infrared as a waveform [191]. ICESat-2 is planned for launch in 2016, and will have a photon counting system to measure reflections of its low pulse energy laser of 532nm light [191]. While meant for ice monitoring, ICESat's GLAS was used for forest and biomass applications [89], and ICESat-2 will have applications for vegetation measurement as well [190].

Other potential sensors for large scale height information are Germany's TanDEM-X and TerraSAR-X. With these sensors, a one metre resolution image can be acquired [192-194].

Allometric equations are built to fit the attributes of sampled trees as closely as possible, expecting that there will be variation and not that they will be very accurate for any individual tree. Hopefully the sampling will reflect the average tree of that species, in that environment. Assessment of aboveground biomass estimations at a per-pixel level is often difficult, and the accuracy may be misleading due to the registration errors between field collection data and the image [195]. As the spatial scale is greater, the accuracy of biomass estimates should increase [196], partly due to spatial agreement between the

maps usually increasing at lower spatial resolution [182]. However, it is important to consider the non-linearity in the process before attempting to up-scale [197]. See Figure 23for the exponential nature of four allometric equations. Depending on the distribution of heights in an averaging window, the biomass may be underestimated if the height of a tall tree is smoothed. The tall trees are significant contributors to biomass. For example, if the tree height in the entire forested Rithet region was averaged (13.87m), the resulting average biomass would be 7.86 t/ha, which is significantly smaller than the average biomass without smoothing of 41.8 t/ha, and even smaller than the >150 t/ha average of Vancouver Island according to Figure 22. According to the equation for DBH (equation9) and for Douglas-fir biomass in Table 2, an average tree would only have 35.17kg of oven-dry biomass. By contrast, a tree of 61m (the maximum height in the Rithet region), has an oven-dry biomass of 14 tonnes.

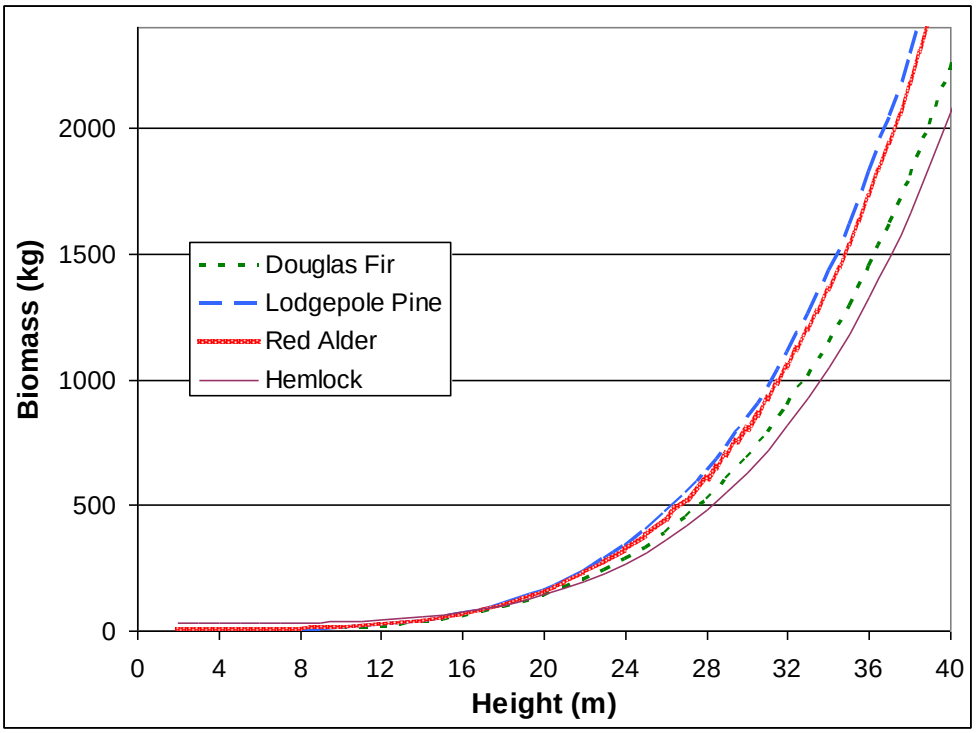

Figure 23: Biomass in kilograms versus height in metres for four species found in the study areas. Height and DBH (estimated from height) are used to find aboveground oven-dry biomass.

An example of biomass estimation in [123] for the GVWD shows how using average DBH in allometric equations for each study plot caused an underestimate of the total biomass by about 20 percent compared with the approach which computes the biomass on a per-tree basis, though there was a high coefficient of determination (R^2=0.987).

5.4 Stem Density Model from Hyperspectral Imagery

Because canopy parameters are easier to judge with remote sensing, scientists have strived to predict characteristics such as tree height and density through canopy models from remotely sensed data; however, the complexity of canopy characteristics, atmospheric conditions, sun angle and viewing geometry, and terrain slope and aspect limit the effectiveness of such models.

An experiment was performed to test the strength of the relationship between hyperspectral imagery and stem density. The results are useful to users who require biomass maps of larger areas where extensive, high resolution lidar height information or optical imagery does not exist and there is no way to generate an SDM from individual tree top locations. PLS (partial least squares) regression was used on hyperspectral data with various levels of averaging. The stem density truth was sampled from the SDM generated by Loos' tree-top finding algorithm and the lidar CHM. A window average of 28 by 28 metres was found to be optimal for AVIRIS data over the D4S2 study site, yielding an average R^2 of 0.94. This was for 6 loading factors (linear combinations of spectral bands), which may be enough to cause overfitting. The more factors, the better the results for the training plots, but this is worse for generalizability [198]. The plot size is large enough to incorporate density information, but smaller than the hectare which is part of the output unit of the resulting stem density image (stems/ha). The regression with the best R^2 (0.98) was from the second derivative of the spectra using the two points left method (see Figure 24 for an explanation of the different transformations used in the PLS regression). For check plots which were not used for the PLS regression, the R^2 was 0.96; this is a high correlation which suggests that a good relationship was found between the SDM from Loos and the spatially-averaged hyperspectral data.

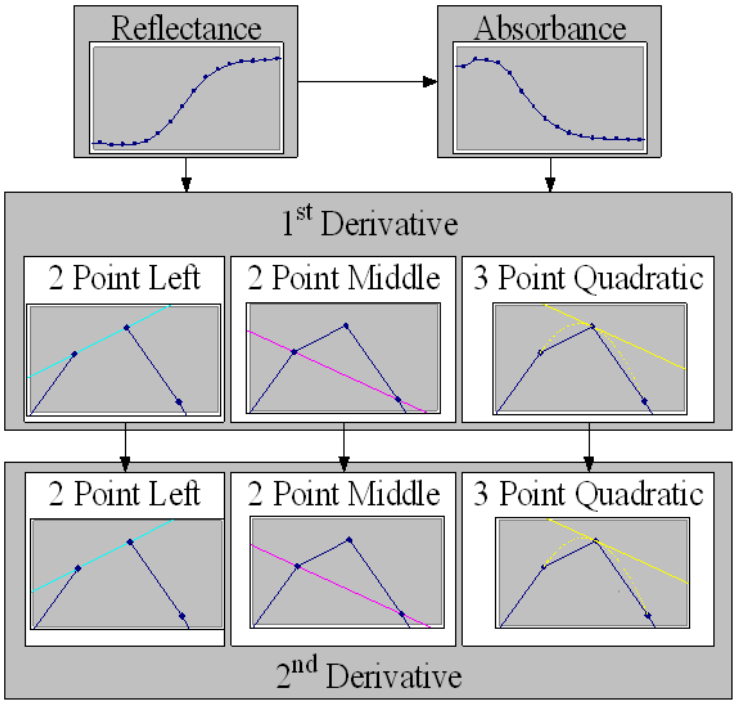

Figure 24: The fourteen transformations which can be tested in the PLS regression program used are represented here. There is reflectance (no transformation), absorbance, and for each of these, there are six types of derivatives which can be taken. The blue dots represent values in a single spectrum sample. The light blue, pink and yellow lines show the slope found by the different derivative techniques [110].

The coefficients from the best regression were applied to the transformed hyperspectral image to create a SDM for the entire area. The biomass map generated from the PLS-derived SDM had a high correlation with the biomass map from the tree-top method, but reported 35% more biomass on average.

The same regression coefficients were applied to AVIRIS data of the Rithet area and there was no correlation ($R^2 \approx 0.0$). This is unfortunate, but not surprising: successful model transfer requires similar biophysical environments in the study areas, and accurate atmospheric correction between multi-scene or multi-temporal data [195]. The AVIRIS data was taken with a Twin Otter aircraft at 4km altitude, and all of the 4m GVWD

imagery was acquired on August 12, 2002, removing atmospheric effects and temporal factors. This leaves overfitting and differences in the forest species from one area to the other. In the original experiment the training and check plots were primarily Douglas-fir.

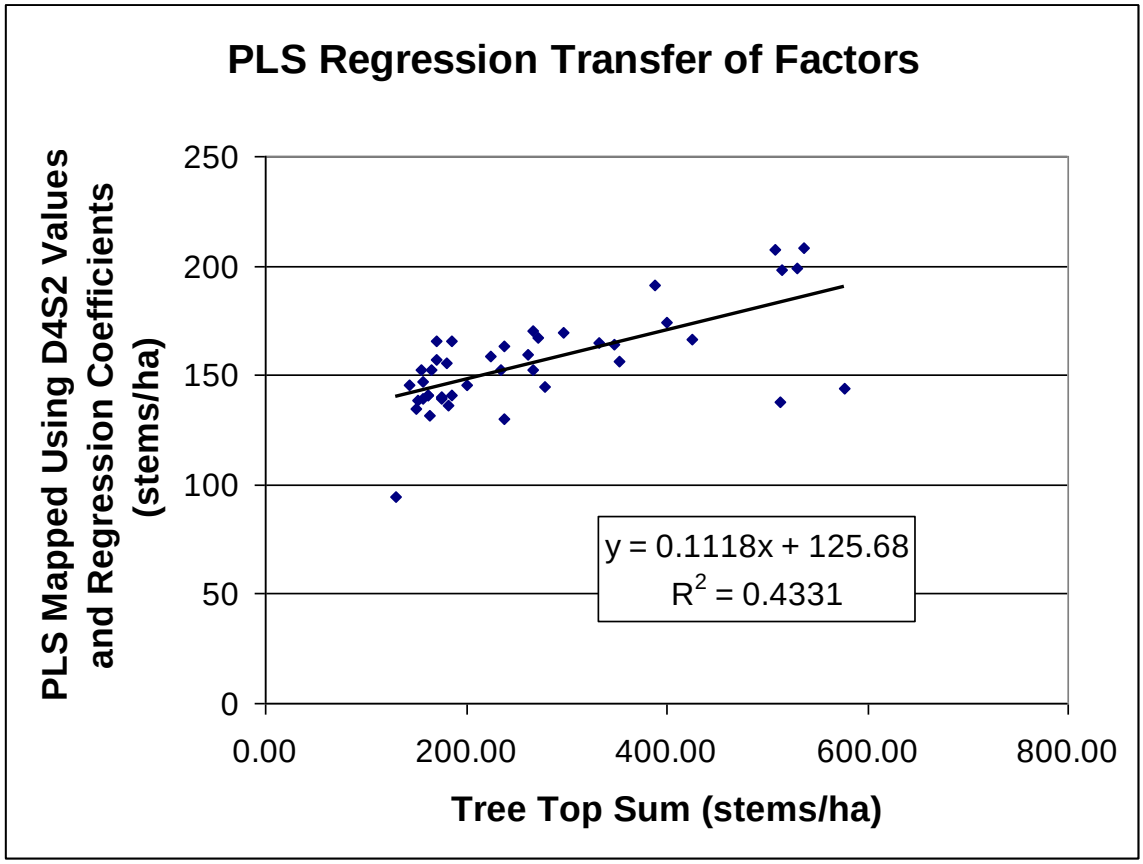

Figure 25: PLS regression model transfer from D4S2 to Rithet at 42 test plots

Subsequent experiments with PLS regression used fewer factors (3) to avoid overfitting. The R^2 for D4S2 stem density prediction was 0.86 for the training plots and 0.52 for the check plots; however the correlation for the model transfer to Rithet was still poor (shown in Figure 25). The correlation was investigated in ENVI, where a scatterplot was created to compare the truth SDM (created with processed tree top locations from lidar), and the result of the model transfer of PLS regression from the D4S2 area to the Rithet area. The scatterplot alone, is in Figure 26, coloured to show the frequency of stem

density values, with purple being the lowest pixel density and red as the highest. The red colouring can be seen at the origin. Some of the highest density is on the zero axes: on the y-axis because of the mask on the PLS map results and on the x-axis because of the non-data regions of the truth SDM image.

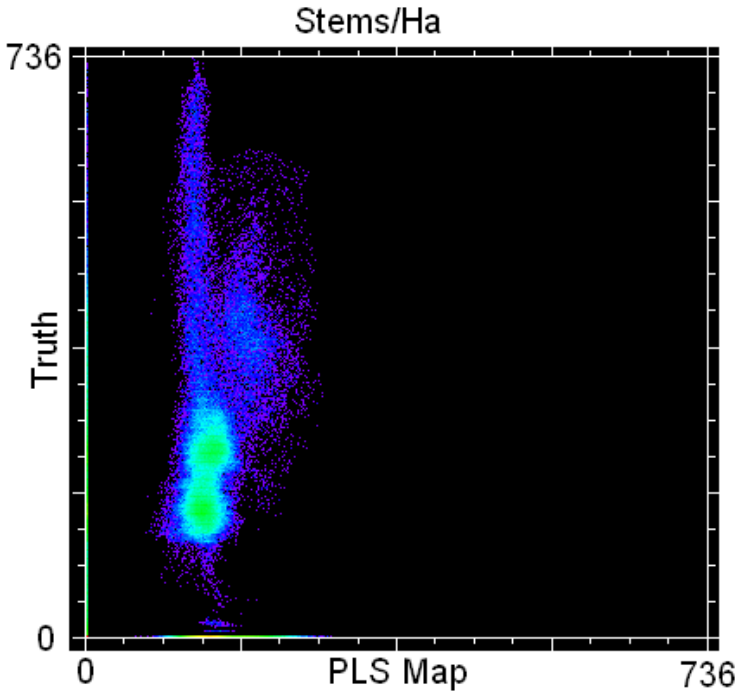

Figure 26: A scatterplot of the Rithet area SDM (stem density model) generated from summing tree tops identified from lidar imagery (y-axis), and an SDM from partial least squares regression (x-axis) using the summed lidar SDM as truth and AVIRIS hyperspectral imagery of the D4S2 area for generating factors.

Figure 27 shows the truth image for the Rithet area (far left), beside the PLS regression result which used factors from D4S2. The green areas on the PLS image correspond to the green pixels on the scatterplot within a margin (± ~140 stems per hectare) around the x=y line. These areas also correspond well with the areas which are classified as dense Douglas-fir (far right). The most extreme underestimations of stem density (red on the scatterplot and the PLS image) are spatially located where there are

stands of Lodgepole Pine and open Douglas-fir (red and blue, respectively, in the far right classification image).

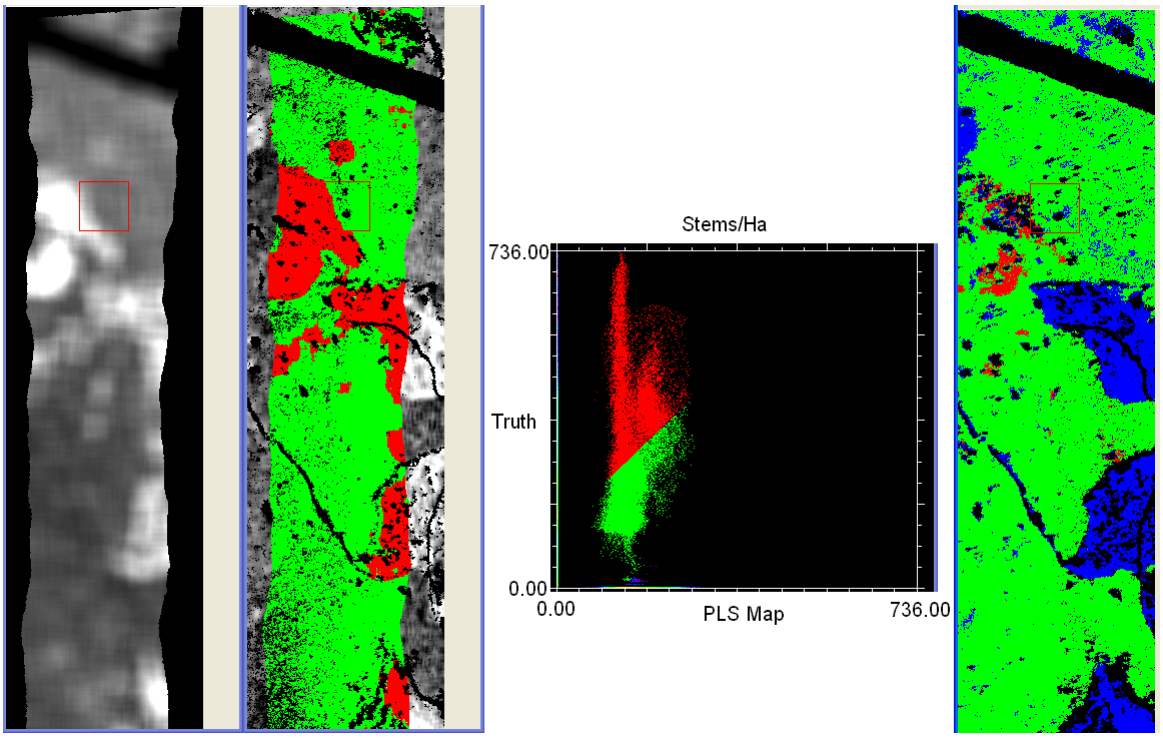

Figure 27: (left to right) the lidar-derived SDM (stem density model) which was used as truth; the SDM from PLS regression factors generated for AVIRIS imagery of D4S2 and applied to the Rithet area, showing colours which correspond to those on the scatterplot; a scatterplot with the PLS values on the x-axis and truth on the y-axis, where a margin around the 1:1 line has been coloured green and above this margin has been coloured red; a forest species classification of the Rithet area where blue is open Douglas-fir, green is dense Douglas-fir, red is Lodgepole Pine and black is non-forest.

The PLS regression which was performed using Rithet plots and applied to the Rithet image (R^2 of 0.89 for the training plots and 0.68 for check plots which were not used in regression), had similar inaccuracies with the open Douglas-fir and Lodgepole Pine classes, as shown in Figure 28.

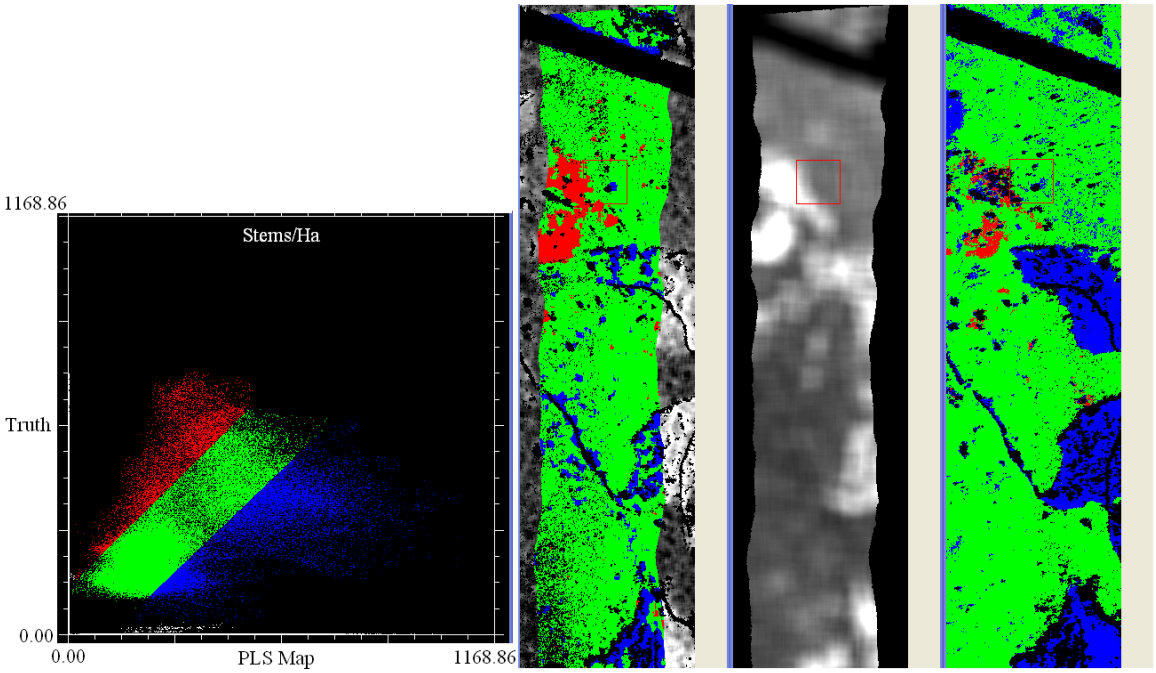

Figure 28: (left to right) A scatterplot for the values of the truth SDM (y-axis) versus the PLS SDM (x-axis); the PLS SDM, coloured corresponding to the colours on the scatterplot; the truth SDM; and the species classification for the area with green for dense Douglas-fir, blue for open Douglas-fir, red for Lodgepole Pine and black for non-forest.

The hyperspectral bands with the most weight (absolute value of the coefficients) are graphed in Figure 29. It is expected that the wavelengths with high reflectance for vegetation, such as the NIR (near infrared), would have more influence. PLS regression has been used to estimate biomass directly from hyperspectral data in a study over the GVWD [110]. Many of the larger coefficients from that study were in the same range as those below in Figure 29, but there was also representation at 480nm, 1712nm, 2020nm and the most extreme spike at 2250nm, in the SWIR. It was found in that study that as the signal to noise ratio drops, the accuracy of the biomass prediction from regression decreases. At the highest SNR, the regression predicted the VDYP biomass for the area with an R^2 of 0.82 [110].

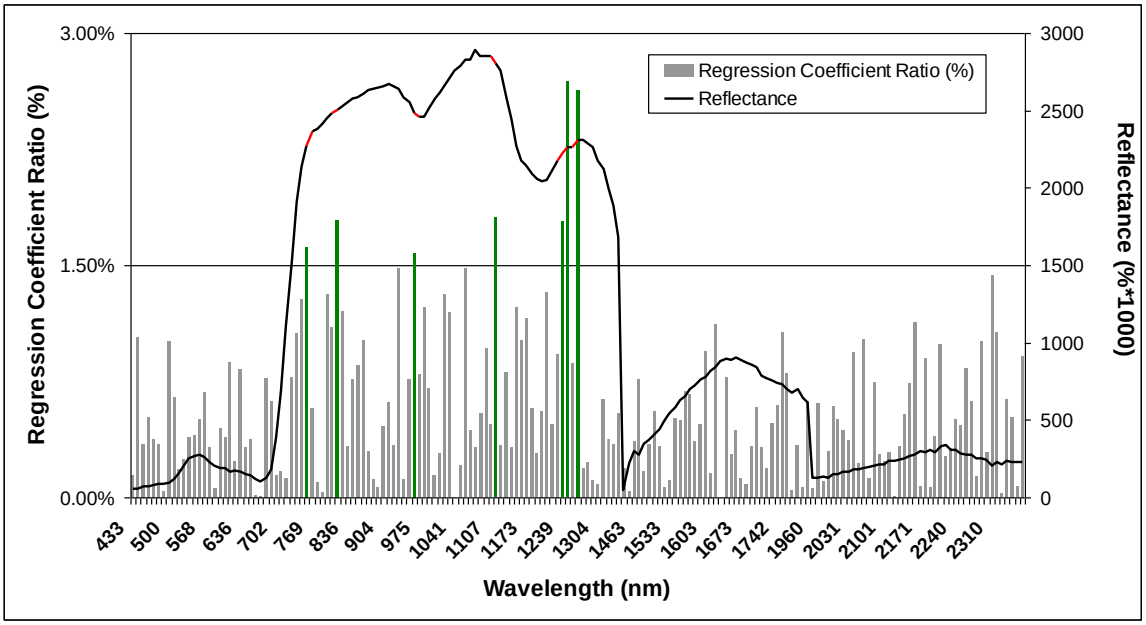

Figure 29: The normalized stem density PLS regression coefficients from D4S2 for each band and an example of reflectance over a forest plot in D4S2. The normalization was done by taking the absolute value of all regression coefficients and dividing them by their sum, giving a percentage. The coefficients with the most weight, past the 1.5% threshold are coloured in green and the corresponding points in the reflectance spectrum are coloured red.

The success of the SDM made from the regression process for D4S2 is encouraging for the scalability of creating large scale aboveground carbon maps. With a relatively small amount of stem density information, a relationship can be found with hyperspectral data through regression. Unfortunately, stem density ground truth should be taken for all of the major species in the area for the most accurate results. Fortunately, with the aid of hyperspectral imagery, the forest species in the area can be classified so that sources of uncertainty may be mapped.

6 Design of System for Creating Aboveground Carbon Maps

A system, named FACEM: Forest Aboveground Carbon Estimation and Mapping, was developed to produce aboveground carbon maps and meet the requirement that users can easily make changes to the system parameters such as enter new forest species allometric equations. The expected input to FACEM includes a species classification from hyperspectral data and forest height from lidar or radar. A survey was done of existing software tools which might support FACEM. The final system can be integrated with ENVI, which assists in the pre-processing of the input. Methods to evaluate FACEM are discussed and its performance is evaluated.

6.1 Requirements

The key requirement of the system is that it produces maps of aboveground carbon. The granularity of the spatial distribution in these maps will depend on the resolution of the input data and by the spatial extents of the imagery. For example, the output cannot be at a finer spatial resolution than the input data, and be accurate. Also, it would not be a very useful map if the spatial resolution is so low that the entire carbon map is only one average value, or if the values were extremely diluted by the non-data outside of the image boundary.

Just like the balance between automation and the ability for human interaction, there is a trade-off between multipurpose, customizable software and more single-purpose, effective software. An extreme example of ultimate customization is to provide the user with a language in which the user may program their own processes and algorithms to fit their exact needs. The other extreme being a black box with a click-and-go interface which is very easy to run, but the inner workings are unknown and unchangeable. The extent of customization for the software is almost boundless given the multitudes of

different algorithms and models which could be used in the process. It has been mentioned that some processes, including classification, involve many options and benefit from human intervention and decision making.

A solution to the customization versus usability debate is a modular design and the inclusion of default settings which can be changed. For example, if there exists a tree species in the input image which is not included in the system library, the user can choose a similar species or add a new allometric equation. A modular design allows parts of the system to be upgraded and substituted easily. The classification stage, for example, should be easy to replace with another method of classification.

As per the discussion of error in section 5.1, and for users with a definition of forest which is dependent on a minimum height: a user should be able to set a height threshold to exclude areas which are not within the desired range. This feature can be utilized to help avoid errors due to misclassification between forest and non-forest, including short shrubs or tall buildings.

6.2 Inputs

To determine the probable inputs, an important question to ask is who will be the users of the system? Users who have access to hyperspectral data of forest with interest in aboveground carbon are most likely to be forest sector workers in government or industries with an interest in the carbon cycle, the environment and forests. These people must have access to remotely sensed hyperspectral imagery and forest data.

For large areas of forest, especially on a provincial or national scale, it is unreasonable to expect extensive airborne lidar coverage due to high costs and relatively small swath width (see section 2.3). Radar for height is more likely, which will be at a lower spatial

resolution (sections 2.2). It is possible that height data could come from a large footprint system such as GLAS on ICESat (decommissioned in October of 2009 [190]) or ICESat-2 (predicted launch date in 2015 [190]). In conclusion, a small amount of lidar height data or a lower resolution radar height image are expected. With a small amount of lidar data, a full SDM can be extrapolated using regression and hyperspectral coverage, as seen in section 5.4.

Multispectral sensors outnumber the hyperspectral sensors on satellite platforms, though there is a trend emerging toward more hyperspectral sensors [158]; for example, there is currently a proposed hyperspectral satellite in planning stages: NASA's hyperspectral infrared imager (HyspIRI) [199, 200]. Accuracies for forest species classification are not expected to be as high for multispectral images as for hyperspectral images, due to fewer spectral bands.

6.3 Automation

When classification is closely supervised by an expert user, there are opportunities to interact and guide the process with intuition from experience. For example, the use of a clustering classifier such as ISODATA or K-means, is advantageous in differentiating classes with intrinsic disparate spectral properties. After clustering the data, a user can visually inspect the results and judge whether to rerun the clustering algorithm on a subset of the data. All possible data and improvements to the equations and algorithms cannot be accounted for in the program; therefore, maintaining transparency and reasonable opportunity to override, without allowing too much room for user error, is important. There will always be a trade-off between automation and potential accuracy. To design an automated system, as the second research question addresses, requires

finding a “sweet spot” between the speed and precision of full automation and the accuracy of expert judgements and subsequent manual calculations - specifically for aboveground carbon mapping of Canadian forests.

The more information the user has about the area to be mapped, the more accurate the results should be. Research is being undertaken to attempt to integrate human intuition with image information mining of remotely sensed imagery. The use of prior knowledge of a study site to constrain the hyperplanes in Support Vector Machine (SVM) classification is shown in [201] to improve recognition rate. However, it should not be expected that all users will have thorough knowledge of the forest areas to be mapped. The best way to allow for such flexibility is with best practices. Clear documentation of the program will be kept for as much understanding as possible. The source code should have high cohesion (statements which use the same data and have similar purposes should be near one another) and low coupling (low dependency between modules, such that a change in one area of the source code should not require many changes in other areas) for ease of making changes for customization or for future improvements.

As better classifiers emerge, and they will, a carbon mapping system which includes classification in its automated process would need to be modified. By taking a classification image as an input, rather than attempting to automate the classification process, more room is left for the user to utilize their prior knowledge and intuition. Also, existing geo-imaging systems, which will be examined in the next section, already include useful classification tools.

6.4 Analysis of Off-the-shelf Components

The environment for visualising images (ENVI) is a set of software tools developed by International Telephone and Telegraph's (ITT) Visual Information Solutions (VIS), now Exelis VIS for imagery analysts, scientists, and GIS (global information systems) professionals [202].

ENVI displays single bands, spectra, and colour composites of images, including hyperspectral data. It includes tools for many processes such as image correction and calibration, dimensionality reduction with minimum noise fraction (see section 4.5), spectral unmixing (see section 4.7 Spectral Unmixing), and classification (see section 4.4). It is written in interactive data language (IDL), a powerful image processing language, which can also be extended to include custom tools. The aboveground carbon mapping process, and the creation of other forest products, as published in several of their papers [104, 105, 122, 203] is done largely with ENVI tools, supervised by remote sensing technologists. Many hyperspectral image analysis groups rely on ENVI software for image analysis. For example, the Advanced Forest Technologies group at the Pacific Forestry Centre, under Natural Resources Canada (NRCan) uses ENVI regularly in viewing and processing remotely sensed images to create forest classifications and forest chemistry maps. The Department of Geography at the University of Victoria also uses ENVI for analysis of hyperspectral data and for teaching remote sensing analysis.

PCI Geomatics developed Geomatica, which is another software suite for processing remotely sensed imagery and maps. Geomatica allows the additions of map features such as legends, scale, and lines of latitude and longitude. There is a hyperspectral module that can be added to the Geomatica core which includes image pre-processing such as

MODTRAN4-based atmospheric correction, noise removal, and spectral unmixing. These same features are available in ENVI [173].

ArcGIS a product of Esri, is software for organization and analysis of geographic information. ArcGIS does not have as extensive a set of tools for manipulation of maps and hyperspectral data, although it can be used with hyperspectral data [204].

MATLAB, by MathWorks, can be used to perform calculations on data. One could write a classifier in MATLAB and apply it to hyperspectral data. However, there are no built-in hyperspectral analysis tools in MATLAB. The input and output would need to be written by the user or provided by a programmer who had already done this. MATLAB does have a large user community. The more application-specific image analysis software packages, above, have much higher prices for licensing than MATLAB.

6.5 Methods for Evaluation

The finished system should be deterministic, GIS professionals should find it understandable and usable, the code should follow best practices, and there should be a speed up on the processing time of carbon map generation, from the non-automated system.

An undergraduate electrical engineering student following the process to create an aboveground carbon map of forest in the study area found that the process took an hour and a half, not including the feature extraction.

6.6 Description of the System

The system, which generates maps of aboveground forest carbon from forest characteristics and a classification image, has been named FACEM: Forest Aboveground Carbon Estimation and Mapping. In the sections below are descriptions of the steps

involved in the system from the acquisition of the input files to the aboveground carbon map. Detailed data flow diagrams can be found in Appendix C. Figure 30 shows the overall process including how the inputs are derived. Figure 31 and Figure 32 (which are also found in Appendix C) show the main parts of the FACEM program.

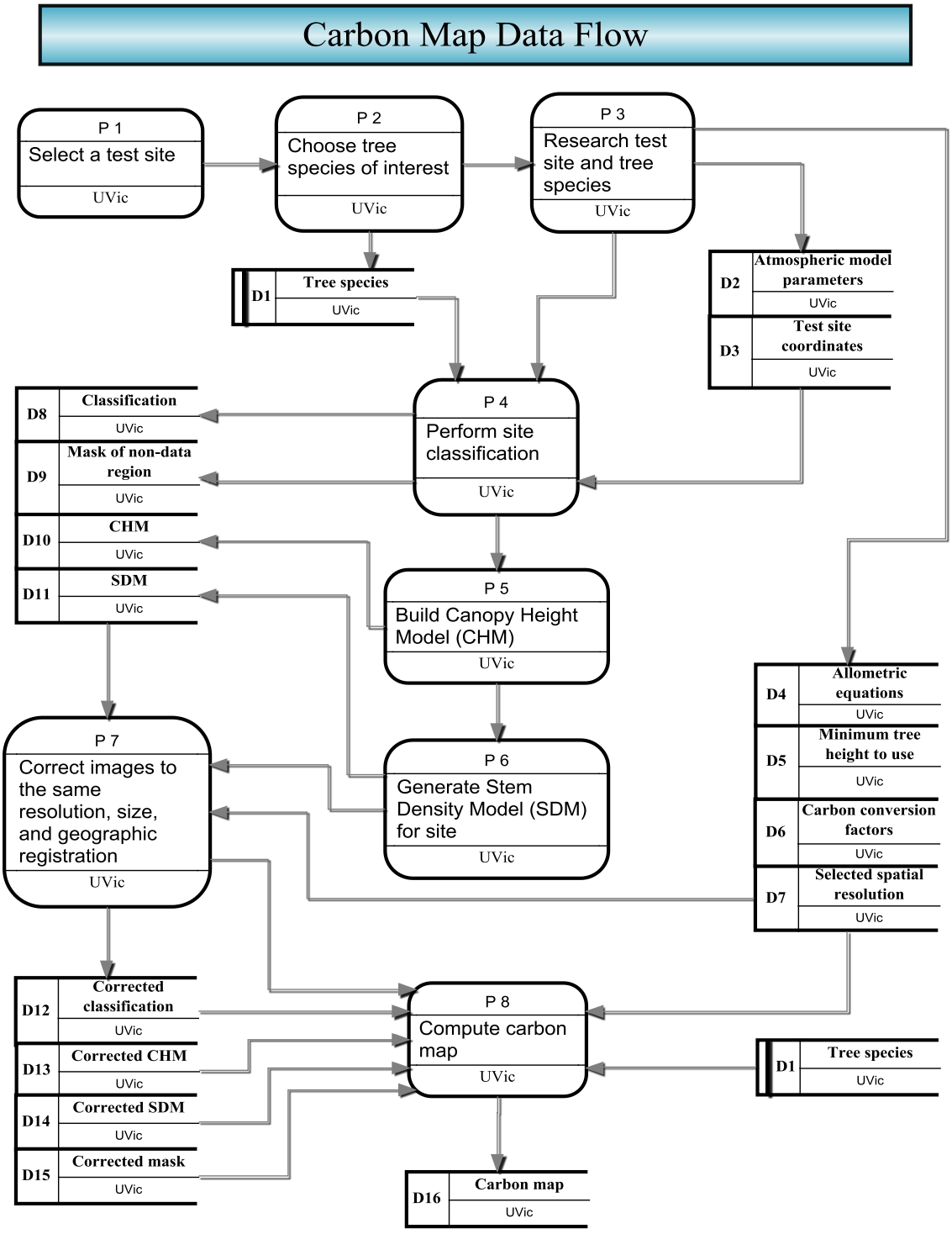

Figure 30: Overview of the carbon estimation and mapping process. Processes are labelled with 'P', data with 'D'. The processes are numbered with their order, starting at P1. The FACEM program is P8.

6.6.1 First Pre-Processing Steps

Raw hyperspectral radiance from an airborne or spaceborne platform is atmospherically corrected, orthographically rectified, and calibrated to reflectance with ground spectroscopy data.

Ground data from field work or local knowledge of the area is georeferenced through the creation of regions of interest (ROIs) for major tree species and non-forest areas such as exposed land and water.

If the user has specific allometric equations, the FACEM program will need to have these equations integrated manually into the source code. The code will then need to be recompiled.

The outputs of the first pre-processing stage are the hyperspectral reflectance images, and ROIs for supervised training. The tree species which are in the image must be identified so they can be matched with pre-programmed allometric equations.

6.6.2 Second Pre-Processing: Classification

The inputs are hyperspectral reflectance images and ROIs for supervised training.

A classification must be run on the reflectance image (or an image which has had dimensionality reduction performed, such as an MNF, as in section 4.5) with the ROIs as training. The most accurate classification result should be used for the automated process (see section 4.4).

The outputs of this process are a classification image and the accuracy of the classifications. An image mask for areas which should be ignored (such as the border of the image, which contains no data) is optional for input into the system.

6.6.3 Third Pre-Processing: Forest Characteristics

Lidar height information is corrected and calibrated, and is made into a CHM (canopy height model); or radar height information is acquired, corrected, calibrated and smoothed into a usable, de-speckled tree height raster.

A SDM (stem density model) raster must be created, whether it is from knowledge of the area, regression analysis (see section 5.4), or through running a tree-top finding algorithm (see section 2.5) on optical or height data and then summing up the number of stems per hectare.

The output of this stage is a CHM image in metres, and SDM in stems/ha

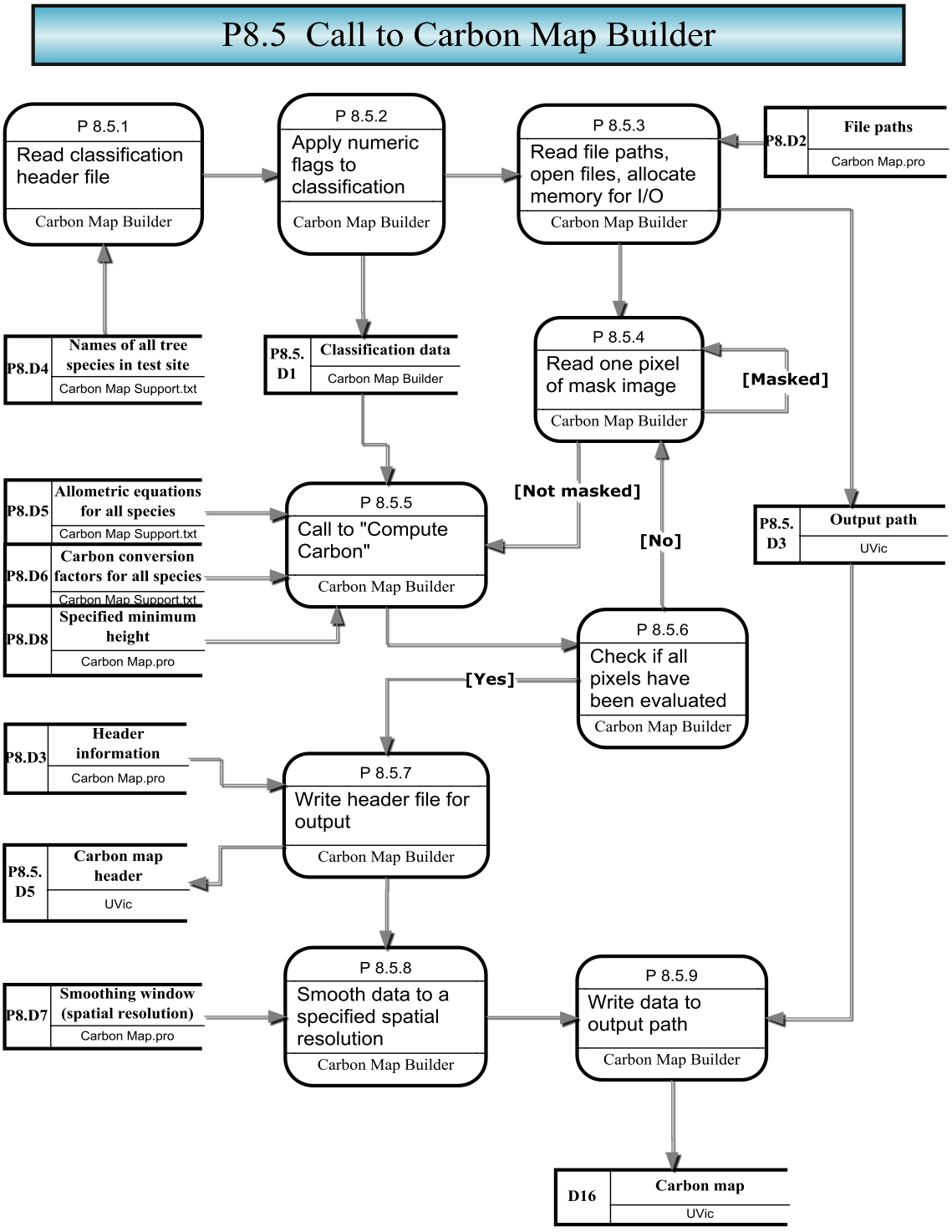

Figure 31: FACEM code flow chart, within ENVI.

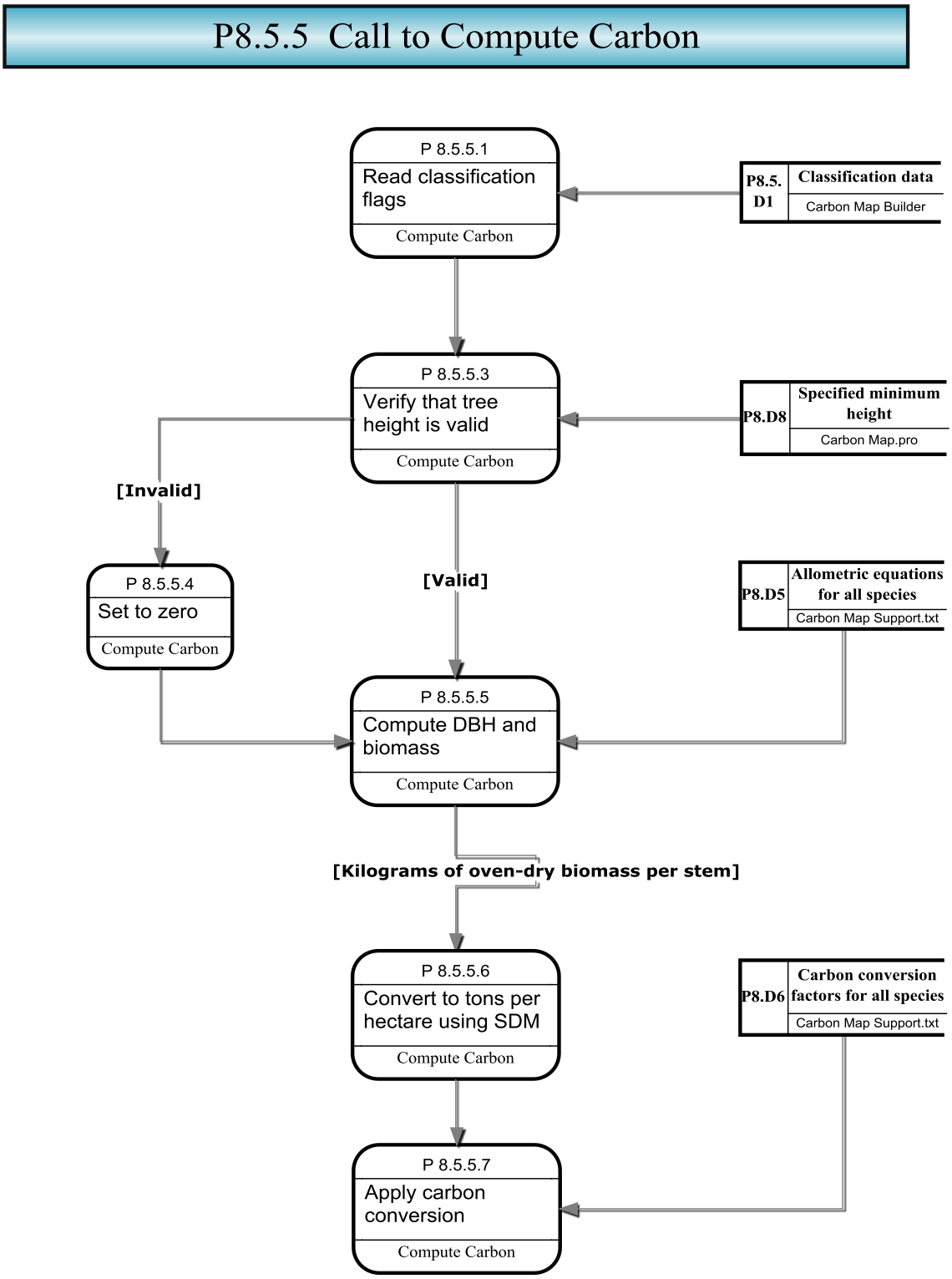

Figure 32: FACEM core function of calculating carbon map from height and stem density.

6.6.4 The Automated Process

Inputs to FACEM are the classification image (the tree species in the class image will be matched by the user with those in the system), CHM (canopy height model), and SDM (stem density model). Allometric equations are written into the code and may be added for additional species. Smoothing of the values for the final carbon map is optional; the user is prompted for a window size which meets, for example, a minimum area mapping requirement.

The height values in the CHM will be used as the tree heights in the allometric equations. The CHM may be averaged or filtered before running the following automated process, if it will be better for the allometric equations which will be used. The user may enter a minimum and maximum tree height for a valid pixel.

The processing steps are as follows:

1. Checks are performed to ensure that the input files are the same size.
2. A header file is written for the resulting carbon map file.
3. The class image is used to isolate the different forest classes, which have been matched with allometric equations by the user. The main output file is created. For each pixel which is classified with a forest species and which has a corresponding height value within the minimum and maximum thresholds, a carbon value is calculated and written to the output file:
    a. Apply corresponding allometric equations for biomass to those corresponding height data, and DBH derived from height data. Oven-dried biomass in kilograms will result.

b. Multiply the biomass by the stem density to get oven-dried biomass per hectare.

c. Multiply the masked biomass data by carbon factor or a default value (0.5) if no factor is given, to get kilograms of carbon per hectare.

d. If the user requested smoothing, apply a low-pass filter of the specified window size over the output image.

4. Calculate carbon statistics for the area and write a report with these details to an output file.

The outputs of FACEM are an aboveground forest carbon map for the area represented in the input files, a header file for the carbon map, and statistics for the output file such as mean carbon values. The units of the carbon map will be tonnes per hectare, with the spatial resolution depending on the smoothing (as per user specification) and the input images.

6.7 Performance

The length of time taken for FACEM to run on D4S2 was less than two seconds. This represents at least half an hour of time saved on manual mask creation, manual mask application and manual band math, for every carbon map created. The convenience is significant as well.

FACEM operates simply and deterministically: if the same input files are given, the same result will be generated.

The source code is documented with inline comments regarding how and where to add allometric equations. There are help files, instructions through the GUI process and also reports and diagrams (see Appendix C) regarding the operation of the software.

6.8 Execution

FACEM may be called on the command line interface. It has been tested on Windows, Linux and Mac-OS. All input files are specified as command line arguments when FACEM is executed, as follows:

```
facem.exe classification-file-path CHM-file-path SDM-file-path output-file-path samples lines smoothing-window-size min-height number-of-forest-species species-information… mask-file-path
```

There are ten arguments, plus three arguments for each forest species specified. The file path parameters include the location and name of the file. The samples and lines arguments are the dimensions of all of the input images, in pixels. The smoothing window size must be an odd number of pixels. The minimum height is in the same units as the CHM and the height taken for the allometric equations, which in this case are metres. The `species-information` should be provided for as many forest species as were specified in the number-of-forest-species argument, in the following format: `ROI-name species-name species-classification-number`. The `species-classification-number` is the value which represents that species in the classification image.

The FACEM executable can be called from command line scripts, to do batches of jobs, or called from programs such as ENVI. An advantage of using FACEM in ENVI is that the samples and lines for the images are automatically found when the files are loaded. Also, the classification values do not need to be entered: the user simply matches the ROI names to the names for the allometric equations (see Figure 37). The user has

fewer opportunities to mistype and more instruction through the steps. Reading through the instructions and having to browse for and open all of the input files in the ENVI program is time consuming; however, use of FACEM is much less time consuming than creating masks for each forest species and the other steps of the more manual carbon mapping process.

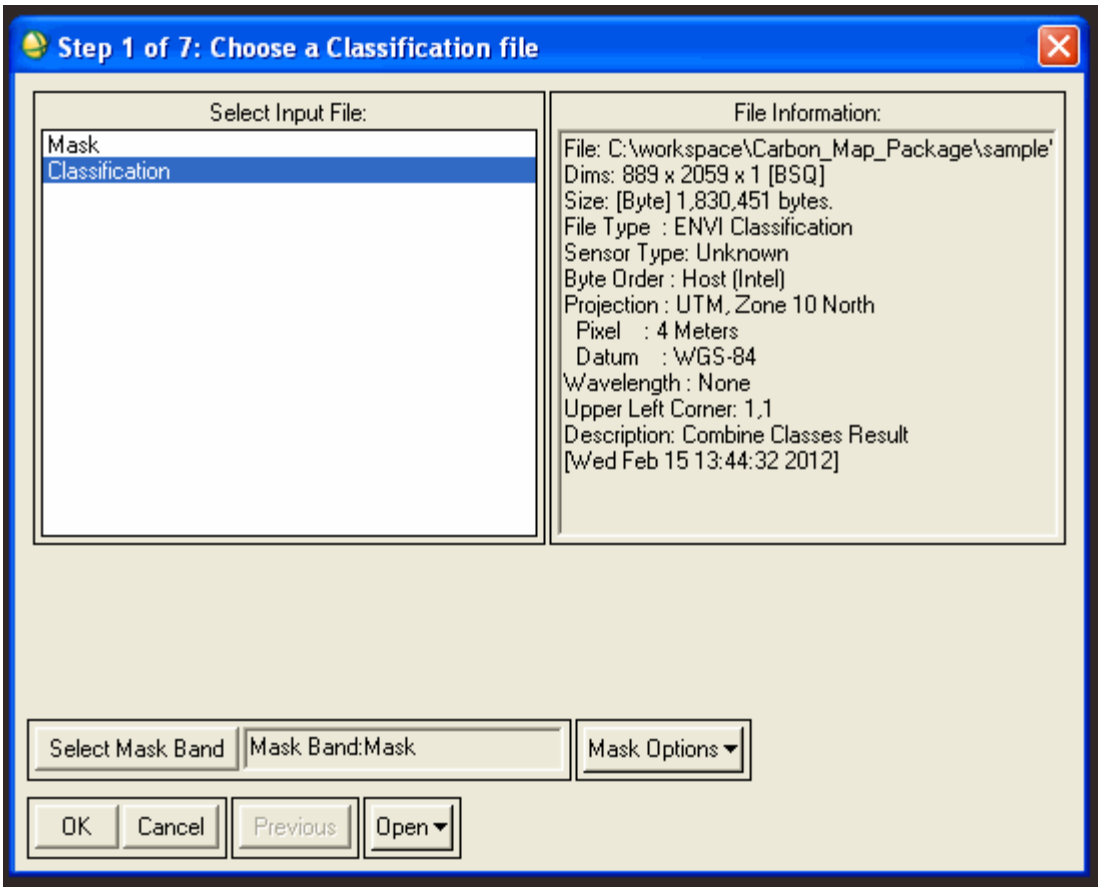

Figure 33: The first step in the ENVI menus, after the welcome dialogue. The user must select the classification image and has the option to choose a mask as well.

Some of the steps FACEM, when wrapped in ENVI, are shown in the figures above. In the window shown in Figure 33, the user chooses the classification image and an optional mask for non-data regions. The next steps are similar, with menus to select the CHM and SDM files, and to choose an output filename and destination.

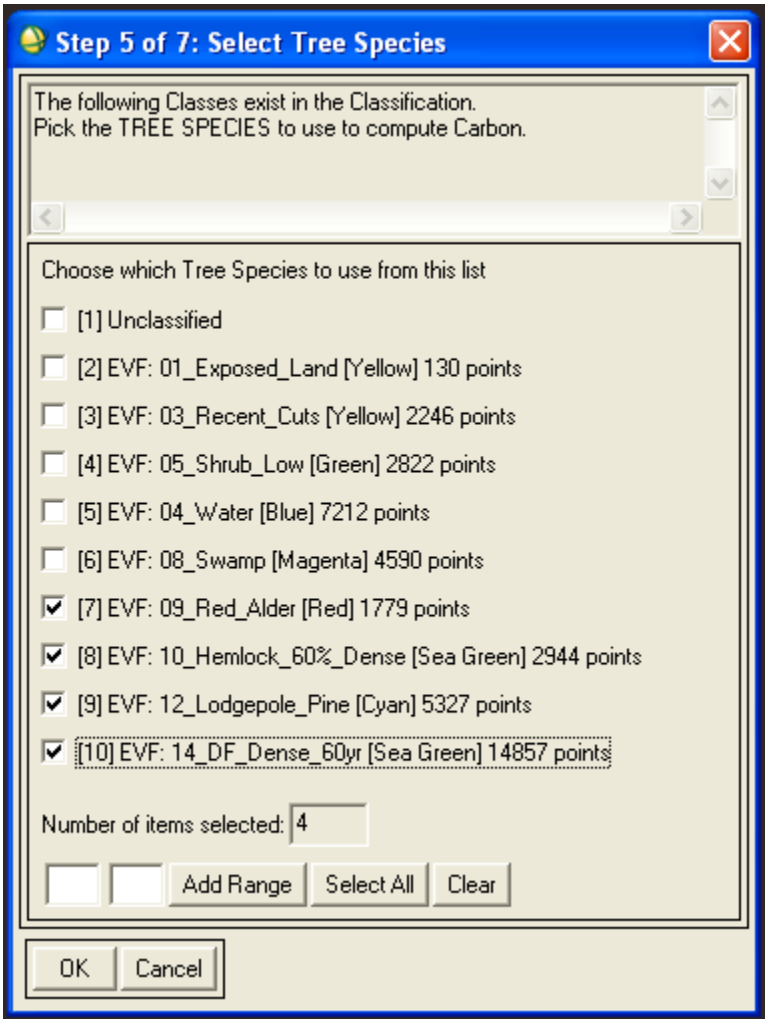

Figure 34: The user selects the forest species of interest from the class names which were read from the classification image.

ENVI reads the classes from the classification file and has the user select the forest species from all of the classes in Figure 34. ENVI then has the user match the allometric equations (hardcoded into FACEM) with the class names via the window in Figure 37. Finally the user may choose to smooth the resulting file and input a minimum tree height, as shown in Figure 35. The program runs and the carbon map is available for viewing in ENVI.

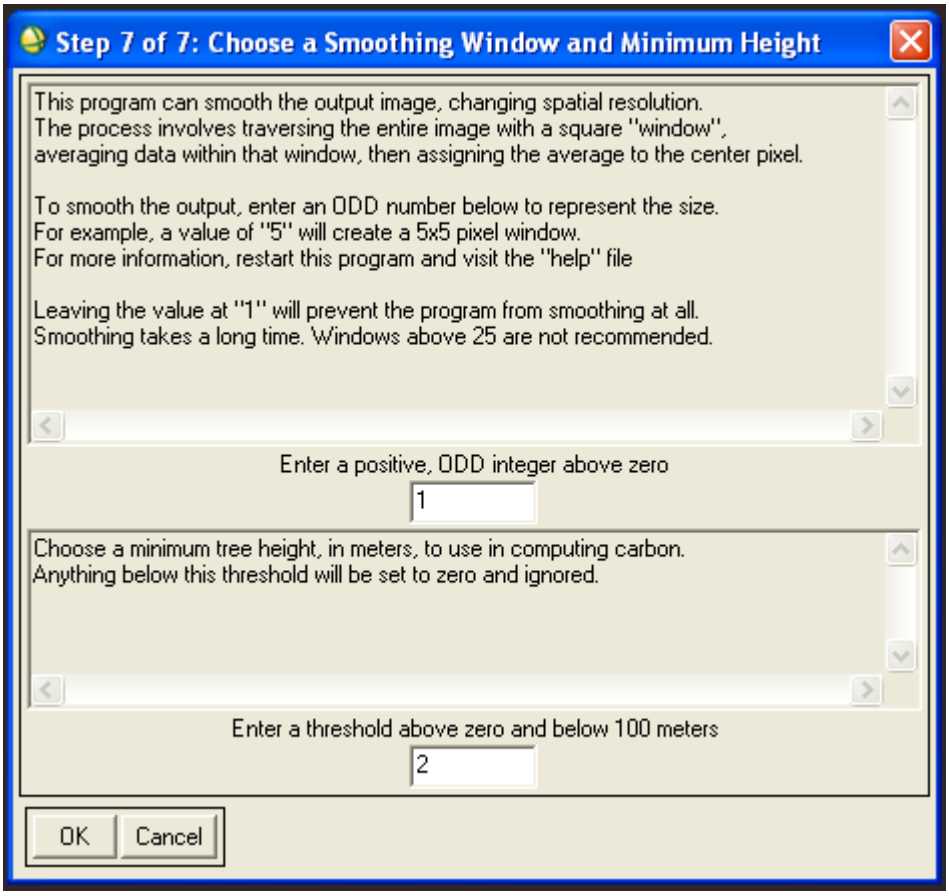

Figure 35: The final step of FACEM in ENVI.

The results of the recent biomass maps are similar looking to the biomass maps produced through PLS regression in [104, 105]. Visual comparisons are shown in Figure 36.

6.9 Limitations

Because there are too many possible forms for allometric equations for which to generalize the input steps, instructions will be provided to adapt FACEM to different allometrics. At present, the user is shown which species are in the image area, as a result of the classification process and the user matches those species to the species for which allometric equations are provided.

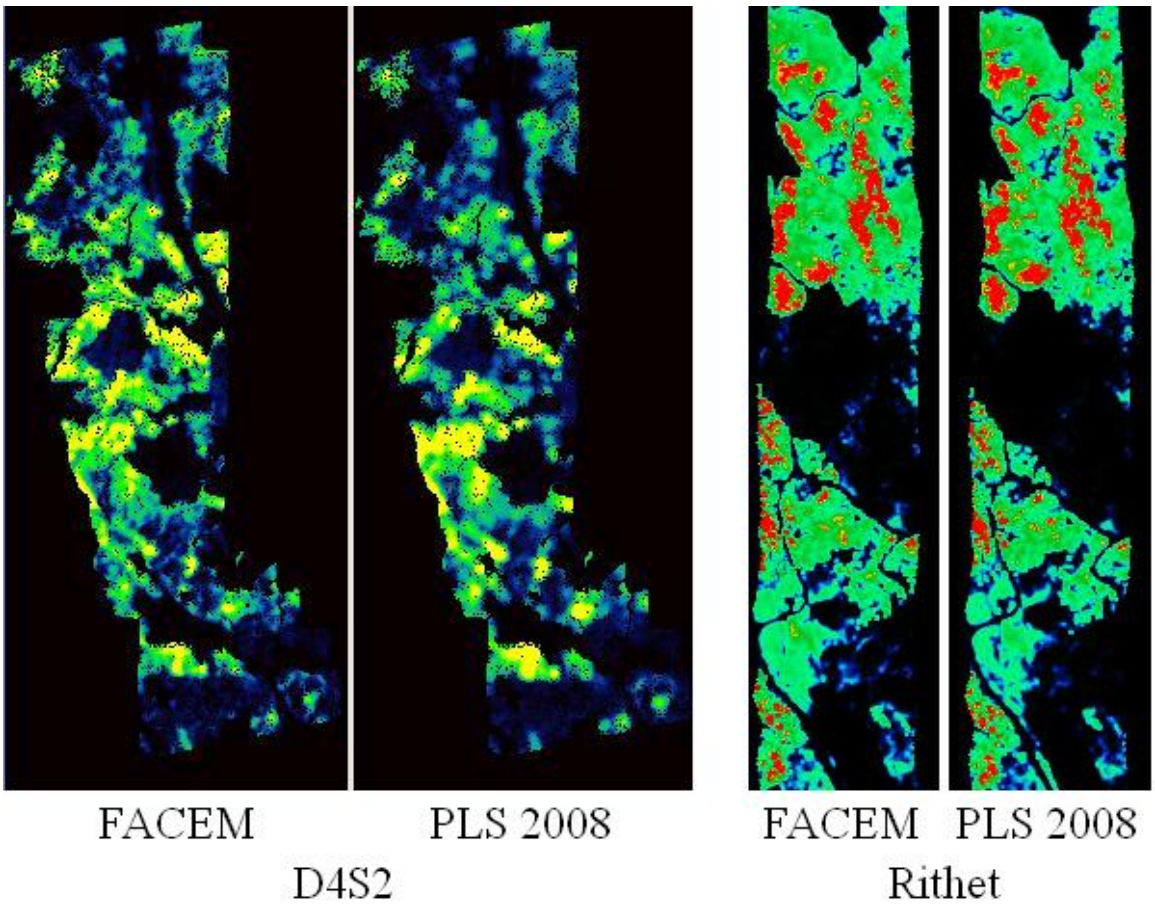

Figure 36: Comparisons of previous biomass maps to recent ones generated with the FACEM program, using the same colour mapping, in the two study areas (only half of the Rithet flightline is shown).

The interface for ENVI has a manual, and a number of pre-written input dialogues. For example, drawing a line to connect species names might be a more intuitive menu for matching the tree species in the system to the tree species from the classification; however, the menu shown in Figure 37 suffices.

If the user is integrating FACEM with ENVI, in Windows, the file path name for the program files must not have any spaces in it. Windows had also imposed a 1000 character limit on file names and paths, which has been solved. A solution to the problem with spaces in file paths has not yet been found.

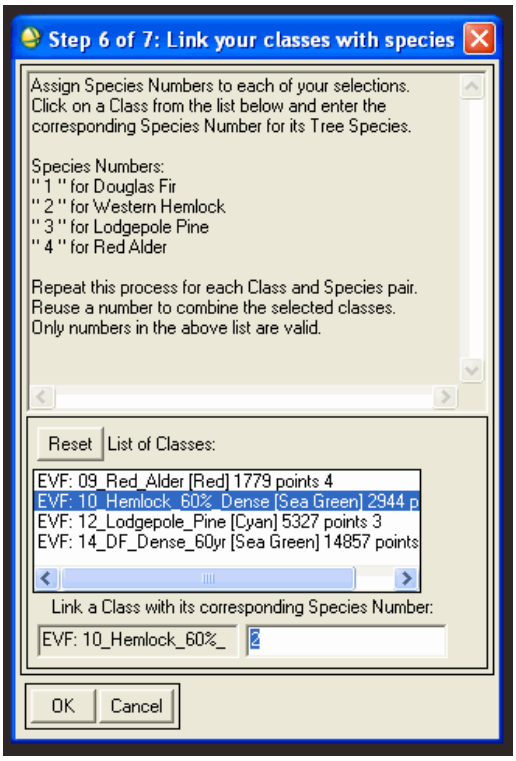

Figure 37: One of the IDL menus as part of the GUI for the automated system when integrated with ENVI.

The maps created and described in this research did not specifically include shrubs or litterfall (dead leaves and branches which are not attached to the trees). There do exist equations and studies which take the understory and litterfall into account in their carbon estimation [205]. The program's instructions may not be inclusive to non-tree elements; however, if these equations were used and if their classes were designated by the user in the mapping process, the program would include this carbon in the resulting map.

7 Conclusions

7.1 Summary

Forests can be an important carbon sink [23] and Canada contains the world's third largest forested area (more than 400 million hectares) [206]. British Columbia has a substantial portion of Canada's forest biomass, and thus carbon [62]. The main result of this thesis is FACEM, which significantly speeds up the aboveground forest carbon mapping process. This thesis has examined two British Columbian study sites with a challenging variety of stand ages. The process of generating carbon maps from forest data was researched, explained and automated. Aspects of the process were reviewed, such as the feature extraction (section 4.5) and classification (section 4.4) of hyperspectral data, the remote acquisition of digital height (sections 2.2 and 2.3) and stem density information (sections 2.5 and 5.4), and the development of allometric equations for forest (section 4.1). The design of a system which acknowledges these steps and automates the carbon mapping process was described (chapter 6) and implemented.

7.2 Contributions

This thesis and the corresponding research was in part an exploration of the literature around remote sensing of the aboveground carbon in forests, especially with optical sensors. The process for generating a carbon map from remotely sensed data was outlined and a system for simplifying the process was developed. The system has filled a gap in the existing computer programs which facilitate the monitoring of forests and provide tools for mapping (sections 1.4 and 6.4). The source code was inspired by an existing low-pass image filtering system and it now contains a function to do just that. The basic program has been modified for many purposes such as to count the number of pixels with

a value greater than some threshold. Certain statistical reports are still included in the finished program and can easily be extended and customized.

The results of two experiments were discussed which had not previously been performed for the study regions: determination of the optimal number of MNF bands for high classification accuracy (section 4.6), and PLS regression to relate spatially averaged hyperspectral data to stem density (section 5.4). The success of the latter opens up possibilities for large scale carbon mapping with small footprint lidar.

7.3 Answers to the Research Questions

A system which automates the creation of aboveground forest carbon maps can indeed be built. The design for one such system is described in section 6.6. Essentially, the program does the tedious work of applying the equations to the forest data, and leaves the stages which benefit the most from close supervision, such as feature extraction and classification, to the user. The solution which was developed is portable as a C++ executable, and it can also be integrated into ENVI and given a graphical user interface.

The determination of the accuracies of aboveground carbon maps can be done by comparisons with ground truth. This is best done with destructive sampling. Unfortunately for the study sites, destructive sampling was not an option and it was necessary to rely upon a diverse set of sources for reliable ground truth data. The VDYP estimates of biomass were compared with the estimates from volume calculated with lidar height (see section 5.1 Error Calculation). Carbon maps resulting from the automated system will match those made in the more manual fashion with the tedious masking and band math process. No known errors have been introduced by the automation.

8 Future Work

The user interface should continue to be refined, tested and tailored to the changing end user needs, especially with any further code changes. In future the program could be extended to include a guide through the earlier stages of the carbon mapping process, without taking control away from the user, but helping him/her make informed decisions. This addition could also result in improvements on speed, through scheduling the steps efficiently: for examples, if an MNF is necessary, it could be run in the background as other system parameters are entered by the user.

The system should be populated with more equations to derive the DBH from tree height, for different tree species, especially deciduous. The biomass and carbon map accuracies rely heavily on the accuracy of this derivation which is likely inaccurate for trees which are dissimilar to Douglas-fir. More species specific allometrics for biomass should be added as well. 80% of the Canadian forest land (circa 1985) is coniferous and Spruce predominates at 35% of the biomass of coniferous species [62]. Allometric equations for Spruce are in Table 6. These should be tested with hyperspectral data for a Spruce-dominant study site.

Table 6: Allometric equations for Spruce trees in British Columbia [129]

Spruce Species	N	R^2	SEM (kg)	SEE (kg)	Equation for oven-dried AGB (kg) from height, H (m) and DBH (m)
Sitka	40	0.96	24.14	19.64	$17.6 + 172.1 \times DBH^2 \times H$
White	105	0.96	34.62	50.82	$32.2 + 146.9 \times DBH^2 \times H$
Engelmann	43	0.98	59.54	54.28	$41.0 + 140.9 \times DBH^2 \times H$
Black	60	0.97	13.35	14.15	$22.4 + 159.5 \times DBH^2 \times H$

More mapping options could be automated, such as extrapolation of biomass through canopy closure calculations or directly through regression on carbon values with

spaceborne multispectral or hyperspectral coverage. There exist programs that are available to do the regression, such as Cubist [154], which was used for extrapolating lidar biomass estimations in [89] and is under the Gnu GPL (general public license) [207].

The PLS regression for stem density findings should be applied to other environments, as should the FACEM program. The way that FACEM is written is amenable to the different allometric equations and corresponding custom masks, classifications, SDM, or CHM files for various situations. FACEM should be able to create carbon maps for any forested location, given the appropriate input files. Areas with sparser forest may benefit more from FACEM as the SDM may be more accurate due to a higher likelihood of detection in automated treetop detection algorithms. The study areas which were used are in some of the densest forest (in terms of biomass) in Canada according to the National Forest Inventory. Carbon mapping results for coniferous forest with similar climates in North America, Europe and Russia would likely be similar in accuracy to the study areas. It should be studied how the volume of biomass changes map accuracy when using the automated allometric method in FACEM.

Bibliography

[1] D. G. Goodenough, A. S. Bhogal, A. Dyk, M. Apps, R. Hall, P. Tickle, C. Hao, K. Butler, and M. Gim, "Determination of above ground carbon in Canada's forests-a multi-source approach," Proc. IEEE International Geoscience and Remote Sensing Symposium (IGARSS) 2000 Honolulu, HI, USA, pp. 949-953, 2000.

[2] H. Chen, "An advanced classification system for processing multitemporal landsat imagery and producing Kyoto Protocol products," Masters, Department of Computer Science, University of Victoria, Victoria, 2004.

[3] K. O. Niemann, G. Quinn, D. G. Goodenough, F. Visintini, and R. Loos, "Addressing the Effects of Canopy Structure on the Remote Sensing of Foliar Chemistry of a 3-Dimensional, Radiometrically Porous Surface," *Selected Topics in Applied Earth Observations and Remote Sensing, IEEE Journal of*, vol. 5, no. 2, pp. 584-593, 2012.

[4] W. Lucht, and C. Schaaf. "BRDF Explained," December 12, 2011; http://www-modis.bu.edu/brdf/brdfexpl.html.

[5] A. Ozturk, M. Kurt, A. Bilgili, and C. Gungor, "Linear approximation of Bidirectional Reflectance Distribution Functions," *Computers & Graphics*, vol. 32, no. 2, pp. 149-158, 2008.

[6] A. Wilson. "Geocorrection," February 14, 2012; http://www.neodc.rl.ac.uk/tutorials/nercarsf/3.htm.

[7] B. Husch, *Forest Mensuration and Statistics*, 1 ed., New York: The Ronald Press Company, 1963.

[8] G. E. Dallal. "P values," February 2, 2012; http://www.jerrydallal.com/LHSP/pval.htm.

[9] M. Barker, and W. Rayens, "Partial least squares for discrimination," *Journal of Chemometrics*, vol. 17, no. 3, pp. 166-173, 2003.

[10] C. Jiangfeng, and Y. Baozong, "Spectral Partial Least Squares Regression," Proc. Signal Processing (ICSP), 2010 IEEE 10th International Conference on, pp. 1351-1354, 2010.

[11] L. R. Odom, and J. R. Morrow Jr, "What's this r? A Correlational Approach to Explaining Validity, Reliability and Objectivity Coefficients," *Measurement in Physical Education & Exercise Science*, vol. 10, no. 2, pp. 137-145, 2006.

[12] M. K. Chung, "R^2," *Encyclopedia of Research Design*, Thousand Oaks, USA: SAGE Publications, 2010.

[13] H. Abdi, and L. J. Williams, "Coefficients of Correlation, Alienation, and Determination," *Encyclopedia of Research Design*, Thousand Oaks, USA: SAGE Publications, 2010.

[14] A. Asuero, A. Sayago, and A. González, "The Correlation Coefficient: An Overview," *Critical Reviews in Analytical Chemistry*, vol. 36, no. 1, pp. 41-59, 2006.

[15] R. K. Moore, and D. S. Simonett, "Radar Remote Sensing in Biology," *BioScience*, vol. 17, no. 6, pp. 384-390, 1967.

[16] P. A. Rosen, S. Hensley, I. R. Joughin, F. K. Li, S. N. Madsen, E. Rodriguez, and R. M. Goldstein, "Synthetic aperture radar interferometry," *Proceedings of the IEEE,* vol. 88, no. 3, pp. 333-382, 2000.

[17] J. Whitmarsh, and Govindjee, "Photosynthesis," *Encyclopedia of Applied Physics*, E. H. Immergut, ed., pp. 513-532: VCH Publishers, Inc, 1995.

[18] J. Amthor, R. Dahlman, D. Drell, and S. Weatherwax, "Carbon Cycling and Biosequestration: Integrating Biology and Climate Through Systems Science," *Report from the March 2008 Workshop,* vol. DOE/SC-108, pp. 141, 2008.

[19] M. Carlowicz. "Seeing Forests for the Trees and the Carbon: Mapping the World's Forests in Three Dimensions," January 10, 2012; http://earthobservatory.nasa.gov/Features/ForestCarbon/?src=eoa-features.

[20] J. E. Smith, L. S. Heath, K. E. Skog, and R. A. Birdsey, *Methods for calculating forest ecosystem and harvested carbon with standard estimates for forest types of the United States,* [Washington, D.C.]: United States Dept. of Agriculture, Forest Service, Northeastern Research Station, 2006.

[21] G. B. Bonan, "Forests and Climate Change: Forcings, Feedbacks, and the Climate Benefits of Forests," *Science,* vol. 320, no. 5882, pp. 1444-1449, June 13, 2008.

[22] W. Powers, "The forest for the trees: building a carbon ranching market," *World Policy Journal,* vol. 26, no. 3, pp. 9, September 22, 2009.

[23] Y. Pan, R. A. Birdsey, J. Fang, R. Houghton, P. E. Kauppi, W. A. Kurz, O. L. Phillips, A. Shvidenko, S. L. Lewis, J. G. Canadell, P. Ciais, R. B. Jackson, S. Pacala, A. D. McGuire, S. Piao, A. Rautiainen, S. Sitch, and D. Hayes, "A Large and Persistent Carbon Sink in the World's Forests," *Science,* July 14, 2011.

[24] S. Solomon, G.-K. Plattner, R. Knutti, and P. Friedlingstein, "Irreversible climate change due to carbon dioxide emissions," *Proceedings of the National Academy of Sciences,* vol. 106, no. 6, pp. 1704-1709, February 10, 2009.

[25] M. Scholze, W. Knorr, N. W. Arnell, and I. C. Prentice, "A climate-change risk analysis for world ecosystems," *Proceedings of the National Academy of Sciences,* vol. 103, no. 35, pp. 13116-13120, August 29, 2006.

[26] M. Marquis, and P. Tans, "Carbon Crucible," *Science,* vol. 320, no. 5875, pp. 460-461, April 25, 2008.

[27] J. H. Seinfeld, "Insights on global warming," *AIChE Journal,* vol. 57, no. 12, pp. 3259-3284, 2011.

[28] V. A. Mohnen, W. Goldstein, and W.-C. Wang, "The conflict over global warming: The application of scientific research to policy choices," *Global Environmental Change,* vol. 1, no. 2, pp. 109-123, 1991.

[29] M. G. R. Cannell, "Growing trees to sequester carbon in the UK: answers to some common questions," *Forestry,* vol. 72, no. 3, pp. 11, 1999.

[30] K. M. K. Yu, I. Curcic, J. Gabriel, and S. C. E. Tsang, "Recent Advances in CO2 Capture and Utilization," *ChemSusChem,* vol. 1, no. 11, pp. 893-899, 2008.

[31] J. Weitz, "Carbon Capture with Artificial Trees," *Planning,* vol. 76, no. 7, pp. 1, August 1, 2010.

[32] X. Cavard, Y. Bergeron, H. Y. H. Chen, and D. Paré, "Mixed-species effect on tree aboveground carbon pools in the east-central boreal forests," *Canadian Journal of Forest Research,* vol. 40, no. 1, pp. 37-47, 2010.

[33] J. B. Bradford, R. A. Birdsey, L. A. Joyce, and M. G. Ryan, “Tree age, disturbance history, and carbon stocks and fluxes in subalpine Rocky Mountain forests,” *Global Change Biology*, vol. 14, no. 12, pp. 2882-2897, 2008.

[34] D. E. Pataki, R. J. Alig, A. S. Fung, N. E. Golubiewski, C. A. Kennedy, E. G. McPherson, D. J. Nowak, R. V. Pouyat, and P. Romero Lankao, “Urban ecosystems and the North American carbon cycle,” *Global Change Biology*, vol. 12, no. 11, pp. 2092-2102, 2006.

[35] R. V. Pouyat, I. D. Yesilonis, and D. J. Nowak, “Carbon Storage by Urban Soils in the United States,” *Journal of environmental quality*, vol. 35, no. 4, pp. 9, July, 2006.

[36] D. J. Nowak, “Atmospheric Carbon Reduction by Urban Trees,” *Journal of Environmental Management*, vol. 37, no. 3, pp. 207-217, 1993.

[37] F. A. Gougeon, “A crown-following approach to the automatic delineation of individual tree crowns in high spatial resolution aerial images,” *Canadian Journal of Remote Sensing*, vol. 21, no. 3, pp. 11, 1995.

[38] A. Richardson, D. G. Goodenough, H. Chen, B. Moa, G. Hobart, and W. Myrvold, "Unsupervised nonparametric classification of polarimetric SAR data using the K-nearest neighbor graph," Proc. IGARSS '10, Honolulu, HI, USA, pp. 1867-1870, 2010.

[39] R. Loos, and O. Niemann, "Identification of Individual Trees And Canopy Shapes using LiDAR Data for Fire Management," Proc. IGARSS '06, Denver, CO, USA, pp. 3755-3757, 2006.

[40] K. O. Niemann, G. Frazer, R. Loos, F. Visintini, and R. Stephen, "Integration of first and last return LiDAR with hyperspectral data to characterize forested environments," Proc. IGARSS '07, Barcelona, Spain, pp. 1537-1540, 2007.

[41] D. G. Goodenough, G. S. Quinn, K. Olaf Niemann, H. Chen, and D. P. Ton, "Helicopter high resolution imaging spectroscopy: Mapping species variation," Proc. Hyperspectral Image and Signal Processing: Evolution in Remote Sensing (WHISPERS), 2011 3rd Workshop on, pp. 1-4, 2011.

[42] "Why SWIR? What is the Value of Shortwave Infrared?," December 13, 2011; http://www.sensorsinc.com/whyswir.html.

[43] R. Bamler, “Principles Of Synthetic Aperture Radar,” *Surveys in Geophysics*, vol. 21, no. 2, pp. 147-157, 2000.

[44] C. Wolff. "Polarization of electromagnetic waves," December 14, 2011; http://www.radartutorial.eu/06.antennas/an06.en.html.

[45] E. Bird, "Synthetic Aperture Radar Systems," *Encyclopedia of Coastal Science*, Encyclopedia of Earth Sciences Series M. L. Schwartz, ed., pp. 937-939: Springer Netherlands, 2005.

[46] C. Wolff. "Coherence in Radar," December 19, 2011; http://www.radartutorial.eu/06.antennas/an06.en.html.

[47] R. Bamler, and P. Hartl, “Synthetic aperture radar interferometry,” *Inverse Problems*, vol. 14, no. 4, pp. R1, 1998.

[48] C. Nealon. "NASA climate change program on ice," http://weblogs.dailypress.com/news/science/dead_rise/2011/04/nasa_climate_change_program_on.html.

[49] A. Garg, V. Mithal, Y. Chamber, I. Brugere, V. Chaudhari, M. Dunham, V. Krishna, S. Krishnamurthy, S. Vangala, S. Boriah, M. Steinbach, V. Kumar, A. Cho, J. Stanley, T. Abraham, J. C. Castilla-Rubio, C. Potter, and S. Klooster, "GOPHER: Global Observation of Planetary Health and Ecosystem Resources," Proc. IGARSS '11, Vancouver, Canada, pp. 1449-1452, 2011.

[50] T. Milne, D. G. Goodenough, and P. Gordon, "REDD+ Implementation," *IEEE Geoscience and Remote Sensing Society (GRSS) Workshop on Forest Mapping, Forest Carbon, and REDD+*, Proc. Asian Conference on Remote Sensing (ACRS) 2011, Taipei, Taiwan, 2011.

[51] R. P. a. Stakeholders, *REDD+ partnership work program components and timeline (2011-2012)*, United Nations Framework Convention on Climate Change, Oslo, Norway, 2010.

[52] "What is a Forest?," December 19, 2011; http://www.daff.gov.au/brs/forest-veg/nfi/forest-info/what-is.

[53] FAO. "Global Forest Resources Assessment 2005" December 18, 2011; http://www.fao.org/docrep/008/a0400e/a0400e00.htm.

[54] M. Nadkarni. "What is a Forest?," December 18, 2011; http://www.forestfacts.org/l_3/forests_1.htm#1p2.

[55] J. E. Smith, L. S. Heath, and M. C. Nichols, *US forest carbon calculation tool: forest-land carbon stocks and net annual stock change*, U.S. Department of Agriculture, Forest Service, Northern Research Station, Newtown Square, PA, 2007.

[56] C. L. Miner, N. R. Walters, and M. L. Belli, *A guide to the TWIGS program for the North Central United States*, U.S. Dept. of Agriculture, Forest Service, North Central Forest Experiment Station, St. Paul, MN, 1998.

[57] J. Penman, *Good Practice Guidance for Land Use, Land-Use Change and Forestry*, Institute for Global Environmental Strategies, Hayama, Japan, 2003.

[58] W. A. Kurz, and M. J. Apps, "A 70-year retrospective analysis of carbon fluxes in the Canadian forest sector," *Ecological Applications*, vol. 9, no. 2, pp. 526-547, May, 1999.

[59] M. A. Wulder, J. A. Dechka, M. A. Gillis, J. E. Luther, R. J. Hall, A. Beaudoin, and S. E. Franklin, "Operational mapping of the land cover of the forested area of Canada with Landsat data: EOSD land cover program," *The Forestry Chronicle*, vol. 79, no. 6, pp. 1075-1083, 2003.

[60] C. Thiel, P. Drezet, C. Weise, S. Quegan, and C. Schmullius, "Radar remote sensing for the delineation of forest cover maps and the detection of deforestation," *Forestry*, vol. 79, no. 5, pp. 9, 2006.

[61] G. Patenaude, R. A. Hill, R. Milne, D. L. A. Gaveau, B. B. J. Briggs, and T. P. Dawson, "Quantifying forest above ground carbon content using LiDAR remote sensing," *Remote Sensing of Environment*, vol. 93, no. 3, pp. 368-380, 2004.

[62] G. M. Bonnor, *Inventory of Forest Biomass in Canada*, Petawawa National Forestry Institute, Ottawa, 1985.

[63] P. Van Deusen, and F. A. Roesch, "Sampling a Tree for Total Volume, Biomass, and Carbon," *Journal of Forestry*, vol. 109, no. 3, pp. 131-135, 2011.

[64] Y. Huang, H. Xu, J. Chen, C. Li, J. Li, and Y. Zhou, "An algorithm for interferometric SAR data processing," *Journal of Electronics (China),* vol. 17, no. 3, pp. 202-207, 2000.

[65] J. Kellndorfer, W. Walker, L. Pierce, C. Dobson, J. A. Fites, C. Hunsaker, J. Vona, and M. Clutter, "Vegetation height estimation from Shuttle Radar Topography Mission and National Elevation Datasets," *Remote Sensing of Environment,* vol. 93, no. 3, pp. 339-358, 2004.

[66] W. S. Walker, J. M. Kellndorfer, and L. E. Pierce, "Quality assessment of SRTM C- and X-band interferometric data: Implications for the retrieval of vegetation canopy height," *Remote Sensing of Environment,* vol. 106, no. 4, pp. 428-448, 2007.

[67] J. M. Kellndorfer, W. S. Walker, E. LaPoint, K. Kirsch, J. Bishop, and G. Fiske, "Statistical fusion of lidar, InSAR, and optical remote sensing data for forest stand height characterization: A regional-scale method based on LVIS, SRTM, Landsat ETM+, and ancillary data sets," *J. Geophys. Res.,* vol. 115, pp. 10, 2010.

[68] S. Solberg, R. Astrup, O. M. Bollandsås, E. Næsset, and D. J. Weydahl, "Deriving forest monitoring variables from X-band InSAR SRTM height," *Canadian Journal of Remote Sensing,* vol. 36, no. 1, pp. 68-79, Feb 4, 2010.

[69] C. P. Tan, A. Marino, I. Woodhouse, S. Cloude, J. Suarez, and C. Edwards, "See the forests with different eyes," Proc. IGARSS '11, Vancouver, Canada, pp. 1405-1408, 2011.

[70] P. Hyde, R. Nelson, D. Kimes, and E. Levine, "Exploring LiDAR–RaDAR synergy—predicting aboveground biomass in a southwestern ponderosa pine forest using LiDAR, SAR and InSAR," *Remote Sensing of Environment,* vol. 106, no. 1, pp. 28-38, 2007.

[71] J. J. Hemphill. "Stereoscopy & Height Measurement " February 2, 2012; http://www.geog.ucsb.edu/~jeff/115a/lectures/stereoscopy_and_height_measurement.html.

[72] W. Kornus, R. Alamús, A. Ruiz, and J. Talaya, "DEM generation from SPOT-5 3-fold along track stereoscopic imagery using autocalibration," *ISPRS Journal of Photogrammetry and Remote Sensing,* vol. 60, no. 3, pp. 147-159, 2006.

[73] T. R. Edwards. "Johnson's Criteria for Pixel Resolution Four Levels of Discrimination," February 4, 2012; http://www.trec.com/johnsoncriteria.htm.

[74] Y. Pailhas, Y. Petillot, and C. Capus, "High-Resolution Sonars: What Resolution Do We Need for Target Recognition?," *EURASIP Journal on Advances in Signal Processing,* vol. 2010, 2010.

[75] Z. Bo, "Computer vision vs. human vision," Proc. Cognitive Informatics (ICCI), 2010 9th IEEE International Conference on, pp. 3-3, 2010.

[76] R. T. H. Collis, "Lidar," *Appl. Opt.,* vol. 9, no. 8, pp. 1782-1788, 1970.

[77] J. C. Suárez, C. Ontiveros, S. Smith, and S. Snape, "Use of airborne LiDAR and aerial photography in the estimation of individual tree heights in forestry," *Computers & Geosciences,* vol. 31, no. 2, pp. 10, 2005.

[78] G. Fraley, "Lidar and Airborne Laser Scanning " *Encyclopedia of Geography,* Thousand Oaks, USA: SAGE Publications, 2010.

[79] R. García, J. C. Suárez, and G. Patenaude, "Delineation of individual tree crowns for LiDAR tree and stand parameter estimation in Scottish woodlands," *Lecture*

Notes in Geoinformation and Cartography, The European Information Society S. I. Fabrikant and M. Wachowicz, eds., pp. 55-85: Springer Berlin Heidelberg, 2007.

[80] J. Evans, A. Hudak, R. Faux, and A. M. Smith, "Discrete Return Lidar in Natural Resources: Recommendations for Project Planning, Data Processing, and Deliverables," *Remote Sensing*, vol. 1, no. 4, pp. 776-794, 2009.

[81] J. S. Evans, A. T. Hudak, and A. M. S. Smith. "Introduction to Discrete Return LiDAR " December 22, 2011; http://www.cnrhome.uidaho.edu/default.aspx?pid=90302

[82] M. A. Wulder, and D. Seemann, "Forest inventory height update through the integration of lidar data with segmented Landsat imagery," *Canadian Journal of Remote Sensing*, vol. 29, no. 5, pp. 536-543, May 1, 2003.

[83] K. O. Niemann, G. Frazer, R. Loos, F. Visintini, and R. Stephen, "Integration of first and last return lidar with hyperspectral data to characterize forested environments," Proc. International Geoscience and Remote Sensing Symposium (IGARSS), Barcelona, Spain, 2007.

[84] E. NÆsset, "Practical Large-scale Forest Stand Inventory Using a Small-footprint Airborne Scanning Laser," *Scandinavian Journal of Forest Research*, vol. 19, no. 2, pp. 164-179, 2004.

[85] Y. Yamamoto, N. Tanioka, and T. Imai, "The spaceborne lidar experiment," *Acta Astronautica*, vol. 39, no. 9-12, pp. 687-695, 1996.

[86] D. M. Winker, R. H. Couch, and M. P. McCormick, "An overview of LITE: NASA's Lidar In-space Technology Experiment," *Proceedings of the IEEE*, vol. 84, no. 2, pp. 164-180, 1996.

[87] J. Boudreau, R. F. Nelson, H. A. Margolis, A. Beaudoin, L. Guindon, and D. S. Kimes, "Regional aboveground forest biomass using airborne and spaceborne LiDAR in Québec," *Remote Sensing of Environment*, vol. 112, no. 10, pp. 3876-3890, 2008.

[88] L. I. Duncanson, "Aboveground biomass estimation using spaceborne LiDAR in managed conifer forests in south central British Columbia," Thesis, Dept. of Geography, University of Victoria, Victoria, British Columbia, Canada, 2009.

[89] M. A. Lefsky, "A global forest canopy height map from the Moderate Resolution Imaging Spectroradiometer and the Geoscience Laser Altimeter System," *Geophysical Research Letters*, vol. 37, Aug 5, 2010.

[90] C. Pascual, A. García-Abril, W. B. Cohen, and S. Martín-Fernández, "Relationship between LiDAR-derived forest canopy height and Landsat images," *International Journal of Remote Sensing*, vol. 31, no. 5, pp. 1261-1280, 2010.

[91] M. Katoh, F. Gougeon, and D. Leckie, "Application of high-resolution airborne data using individual tree crowns in Japanese conifer plantations," *Journal of Forest Research*, vol. 14, no. 1, pp. 10-19, 2009.

[92] L. Chasmer, C. Hopkinson, and P. Treitz, "Investigating laser pulse penetration through a conifer canopy by integrating airborne and terrestrial lidar," *Canadian Journal of Remote Sensing*, vol. 32, no. 2, pp. 10, Feb. 14, 2006.

[93] M. Maltamo, K. Mustonen, J. Hyyppä, J. Pitkänen, and X. Yu, "The accuracy of estimating individual tree variables with airborne laser scanning in a boreal nature

reserve," *Canadian Journal of Forest Research*, vol. 34, no. 9, pp. 1791-1801, 2004.

[94] D. L. A. Gaveau, and R. A. Hill, "Quantifying canopy height underestimation by laser pulse penetration in small-footprint airborne laser scanning data," *Canadian Journal of Remote Sensing,* vol. 29, no. 5, pp. 650-657, October, 2003.

[95] S. Magnussen, and P. Boudewyn, "Derivations of stand heights from airborne laser scanner data with canopy-based quantile estimators," *Canadian Journal of Forest Research,* vol. 28, no. 7, pp. 1016-1031, April 27, 1998.

[96] D. G. Leckie, F. A. Gougeon, D. A. Hill, R. Quinn, L. Armstrong, and R. Shreenan, "Combined high-density lidar and multispectral imagery for individual tree crown analysis," *Canadian Journal of Remote Sensing,* vol. 29, no. 5, pp. 17, 2003.

[97] S. Magnussen, P. Eggermont, and V. N. LaRiccia, "Recovering Tree Heights from Airborne Laser Scanner Data," *Forest Science,* vol. 45, no. 3, pp. 407-422, 1999.

[98] D. Gatziolis, J. S. Fried, and V. S. Monleon, "Challenges to Estimating Tree Height via LiDAR in Closed-Canopy Forests: A Parable from Western Oregon," *Forest Science,* vol. 56, no. 2, pp. 17, 2010.

[99] D. G. Leckie, F. o. A. Gougeon, N. Walsworth, and D. Paradine, "Stand delineation and composition estimation using semi-automated individual tree crown analysis," *Remote Sensing of Environment,* vol. 85, no. 3, pp. 355-369, 2003.

[100] D. S. Culvenor, "TIDA: an algorithm for the delineation of tree crowns in high spatial resolution remotely sensed imagery," *Computers & Geosciences,* vol. 28, no. 1, pp. 33-44, 2002.

[101] D. G. Leckie, F. o. A. Gougeon, S. Tinis, T. Nelson, C. N. Burnett, and D. Paradine, "Automated tree recognition in old growth conifer stands with high resolution digital imagery," *Remote Sensing of Environment,* vol. 94, no. 3, pp. 311-326, 2005.

[102] H. Weinacker, B. Koch, U. Heyder, and R. Weinacker, "Development of filtering, segmentation and modelling modules for lidar and multispectral data as a fundament of an automatic forest inventory system," *Laser-Scanner for forest and landscape assessment,* Proc. ISPRS, Freiburg, Germany, pp. 50-55, 2004.

[103] S. C. Popescu, R. H. Wynne, and R. F. Nelson, "Measuring individual tree crown diameter with lidar and assessing its influence on estimating forest volume and biomass," *Canadian Journal of Remote Sensing,* vol. 29, no. 5, pp. 14, 2003.

[104] D. G. Goodenough, K. O. Niemann, A. Dyk, G. Hobart, P. Gordon, M. Loisel, and C. Hao, "Comparison of Aviris and AISA Airborne Hyperspectral Sensing for Above-Ground Forest Carbon Mapping," Proc. IGARSS '08, Boston, MA, USA, pp. II-129-II-132, 2008.

[105] D. G. Goodenough, K. O. Niemann, A. Dyk, G. Hobart, P. Gordon, and M. Loisel, "A Comparison Of Forest Products From AISA And AVIRIS," Proc. ASTRO 2008, Montreal, Quebec, pp. 1-13, 2008.

[106] J. W. Metzler, and S. A. Sader, "Model development and comparison to predict softwood and hardwood per cent cover using high and medium spatial resolution

imagery," *International Journal of Remote Sensing*, vol. 26, no. 17, pp. 3749-3761, Sept. 10, 2005.

[107] A. Smith, and B. N. Rock, "Mapping Forest Types using Multi-Sensor Remote Sensing Methods," Proc. IGARSS '08, Boston, MA, USA, pp. III - 708-III - 711, 2008.

[108] G. Sun, K. J. Ranson, Z. Guo, Z. Zhang, P. Montesano, and D. Kimes, "Forest biomass mapping from lidar and radar synergies," *Remote Sensing of Environment*, vol. 115, no. 11, pp. 2906-2916, 2011.

[109] J. Anderson, M. E. Martin, M. L. Smith, R. O. Dubayah, M. A. Hofton, P. Hyde, B. E. Peterson, J. B. Blair, and R. G. Knox, "The use of waveform lidar to measure northern temperate mixed conifer and deciduous forest structure in New Hampshire," *Remote Sensing of Environment*, vol. 105, no. 3, pp. 248-261, 2006.

[110] D. G. Goodenough, T. Han, A. Dyk, J. Gour, and J. Li, "Mapping Forest Biomass with AVIRIS and Evaluating SNR Impact on Biomass Prediction," *2005 AVIRIS Workshop* R. Green and J. Raney, eds., 2005.

[111] S. Campbell, and D. Philippe. "Plant Detail Gaultheria shallon," December 22, 2011; http://nativeplants.evergreen.ca/search/view-plant.php?ID=00320.

[112] D. Tirmenstein. "Gaultheria shallon," December 22, 2011; http://www.fs.fed.us/database/feis/plants/shrub/gausha/all.html.

[113] R. K. Hermann, and D. P. Lavender, "Douglas-fir planted forests," *New Forests*, vol. 17, no. 1, pp. 53-70, 1999.

[114] P. Gupta, and D. Holmstrom, "Douglas - Fir (Pseudotsuga menziesii)
Protocol for Somatic Embryogenesis in Woody Plants," Forestry Sciences S. Jain and P. Gupta, eds., pp. 25-34: Springer Netherlands, 2005.

[115] W. Scott, R. Meade, R. Leon, D. Hyink, and R. Miller, "Planting density and tree-size relations in coast Douglas-fir," *Canadian Journal of Forest Research*, vol. 28, no. 1, pp. 74-78, Jan. 1, 1998.

[116] W. B. Critchfield, *Genetics of lodgepole pine*, [Washington, D.C.]: U.S. Dept. of Agriculture, Forest Service : For sale by the Supt. of Docs., U.S. G.P.O., 1980.

[117] J. M. Cahill, *Western hemlock*, [Washington, D.C.]: Forest Service, U.S. Dept. of Agriculture : [Supt. of Docs., U.S. G.P.O., distributor], 1984.

[118] S. Getzin, C. Dean, F. He, J. A. Trofymow, K. Wiegand, and T. Wiegand, "Spatial patterns and competition of tree species in a Douglas-fir chronosequence on Vancouver Island," *Ecography*, vol. 29, no. 5, pp. 671-682, 2006.

[119] N. P. Worthington, F. Pacific Northwest, and S. Range Experiment, *Silvical characteristics of red alder*, Portland, Or.: Pacific Northwest Forest and Range Experiment Station, U.S. Dept. of Agriculture, Forest Service, 1957.

[120] A. R. Weiskittel, D. W. Hann, D. E. Hibbs, T. Y. Lam, and A. A. Bluhm, "Modeling top height growth of red alder plantations," *Forest Ecology and Management*, vol. 258, no. 3, pp. 323-331, 2009.

[121] D. T. Lester, D. S. DeBell, and S. Pacific Northwest Research, *Geographic variation in red alder*, Portland, Or. (319 S.W. Pine St., Portland 97208): U.S. Dept. of Agriculture, Forest Service, Pacific Northwest Research Station, 1989.

[122] D. G. Goodenough, K. O. Niemann, G. S. Quinn, P. Gordon, A. Gross, H. Tian, G. Hobart, C. Hao, and A. Dyk, "Comparison of AVIRIS and AISA for chemistry mapping," Proc. IGARSS '09, Cape Town, Africa, pp. I-80-I-83, 2009.

[123] A. S. P. Bhogall, D. G. Goodenough, A. Dyk, H. Chen, K. O. Niemann, and C. West, "Extraction of forest attribute information using multisensor data fusion techniques: a case study for a test site on Vancouver Island, British Columbia," Proc. Communications, Computers and signal Processing, 2001. PACRIM. 2001 IEEE Pacific Rim Conference on, pp. 674-680 vol.2, 2001.

[124] J. A. Trofymow, G. L. Porter, B. A. Blackwell, R. Arksey, V. Marshall, and D. Pollard, *Chronosequences for research into the effects of converting coastal British Columbia old-growth forests to managed forests: an establishment report*, [Victoria, B.C.]: Pacific Forestry Centre, 1997.

[125] D. G. Goodenough, A. Dyk, G. Hobart, and C. Hao, "Forest information products from hyperspectral data - Victoria and Hoquiam test sites," Proc. IGARSS '07, Barcelona, Spain, pp. 1532-1536, 2007.

[126] J. E. Smith, and S. United, *Methods for calculating forest ecosystem and harvested carbon with standard estimates for forest types of the United States*, Newtown Square, PA: United States Department of Agriculture, Forest Service, Northeastern Research Station, 2006.

[127] Merriam-Webster.com, "allometry," *Merriam-Webster*, Online, 2011.

[128] M. T. Ter-Mikaelian, and M. D. Korzukhin, "Biomass equations for sixty-five North American tree species," *Forest Ecology and Management,* vol. 97, no. 1, pp. 1-24, 1997.

[129] J. T. Standish, G. H. Manning, and J. P. Demaerschalk, *Development of biomass equations for British Columbia tree species*, Pacific Forest Research Centre, Victoria, BC, 1985.

[130] G. H. Manning, M. R. C. Massie, and J. D. Rudd, *Metric single-tree weight tables for the Yukon Territory*, Pacific Forest Research Centre, Victoria, BC, 1984.

[131] O. Hagner, and H. Reese, "A method for calibrated maximum likelihood classification of forest types," *Remote Sensing of Environment,* vol. 110, no. 4, pp. 438-444, 2007.

[132] C. Mingmin, K. Qian, J. A. Benediktsson, and F. Rui, "Ensemble Classification Algorithm for Hyperspectral Remote Sensing Data," *Geoscience and Remote Sensing Letters, IEEE,* vol. 6, no. 4, pp. 762-766, 2009.

[133] M. A. Cho, L. Naidoo, R. Mathieu, and G. P. Asner, "Mapping savanna tree species using Carnegie Airborne Observatory hyperspectral data resampled to WorldView-2 multispectral configuration," *Ecosystem function in savannas: measurement and modelling at landscape to global scales*, Proc. 34th International Symposium on Remote Sensing of Environment, Sydney, Australia, p. 4, 2011.

[134] W. Xiang, S. Liu, X. Deng, A. Shen, X. Lei, D. Tian, M. Zhao, and C. Peng, "General allometric equations and biomass allocation of Pinus massoniana trees on a regional scale in southern China," *Ecological Research,* vol. 26, no. 4, pp. 697-711, 2011.

[135] R. J. Williams, A. Zerihun, K. D. Montagu, M. Hoffman, L. B. Hutley, and X. Chen, "Allometry for estimating aboveground tree biomass in tropical and subtropical eucalypt woodlands: towards general predictive equations," *Australian Journal of Botany,* vol. 53, no. 7, pp. 607-619, 2005.

[136] T. G. Cole, and J. J. Ewel, "Allometric equations for four valuable tropical tree species," *Forest Ecology and Management,* vol. 229, no. 1-3, pp. 351-360, 2006.
[137] V. Singh, A. Tewari, S. P. S. Kushwaha, and V. K. Dadhwal, "Formulating allometric equations for estimating biomass and carbon stock in small diameter trees," *Forest Ecology and Management,* vol. 261, no. 11, pp. 1945-1949, 2011.
[138] C. Véga, and S. Durrieu, "Multi-level filtering segmentation to measure individual tree parameters based on Lidar data: Application to a mountainous forest with heterogeneous stands," *International Journal of Applied Earth Observation and Geoinformation,* vol. 13, no. 4, pp. 646-656, 2011.
[139] T. Allouis, S. Durrieu, C. Véga, and P. Couteron, "Exploiting Fullwaveform Lidar Signals to Estimate Tiimber Volume and Above-Ground Biomass of Individual Trees," Proc. IGARSS '11, Vancouver, Canada, pp. 1251-1254, 2011.
[140] M. A. Lefsky, W. B. Cohen, D. J. Harding, G. G. Parker, S. A. Acker, and S. T. Gower, "Lidar remote sensing of above-ground biomass in three biomes," *Global Ecology and Biogeography,* vol. 11, no. 5, pp. 393-399, 2002.
[141] T. Mette, K. Papathanassiou, I. Hajnsek, H. Pretzsch, and P. Biber, "Applying a common allometric equation to convert forest height from Pol-InSAR data to forest biomass," Proc. IGARSS '04, Anchorage, AK, USA, p. 272, 2004.
[142] A. T. Caicoya, F. Kugler, K. Papathanassiou, P. Biber, and H. Pretzsch, "Biomass estimation as a function of vertical forest structure and forest height - Potential and limitations for Radar Remote Sensing," *Synthetic Aperture Radar (EUSAR), 2010 8th European Conference on*, pp. 1-4, 2010.
[143] D. R. Vann, P. A. Palmiotto, and G. Richard Strimbeck, "Allometric equations for two South American conifers: Test of a non-destructive method," *Forest Ecology and Management,* vol. 106, no. 2–3, pp. 55-71, 1998.
[144] C. Gehring, S. Park, and M. Denich, "Liana allometric biomass equations for Amazonian primary and secondary forest," *Forest Ecology and Management,* vol. 195, no. 1-2, pp. 69-83, 2004.
[145] D. Zianis, and M. Mencuccini, "On simplifying allometric analyses of forest biomass," *Forest Ecology and Management,* vol. 187, no. 2-3, pp. 311-332, 2004.
[146] K. Staenz, D. J. Williams, M. Truchon, and R. Fritz, "Estimation of crown closure from AVIRIS data using regression analysis," *JPL Airborne Geoscience Workshop*, Proc. AVIRIS Workshop, Washington, D.C., USA, pp. 169-172, 1993.
[147] W. Wilcke, Y. Oelmann, A. Schmitt, C. Valarezo, W. Zech, and J. Homeier, "Soil properties and tree growth along an altitudinal transect in Ecuadorian tropical montane forest," *Journal of Plant Nutrition and Soil Science*, vol. 171, no. 2, pp. 220-230, 2008.
[148] G. P. Asner, R. F. Hughes, T. A. Varga, D. E. Knapp, and T. Kennedy-Bowdoin, "Environmental and Biotic Controls over Aboveground Biomass Throughout a Tropical Rain Forest," *Ecosystems,* vol. 12, no. 2, pp. 261-278, Feb, 2009.
[149] W. A. Kurz, S. J. Beukema, and M. J. Apps, "Estimation of root biomass and dynamics for the carbon budget model of the Canadian forest sector," *Canadian Journal of Forest Research,* vol. 26, no. 11, pp. 1973-1979, 2012/01/30, 1996.
[150] J. R. Wang, T. Letchford, P. Comeau, and J. P. Kimmins, "Above- and below-ground biomass and nutrient distribution of a paper birch and subalpine fir mixed-

species stand in the Sub-Boreal Spruce zone of British Columbia," *Forest Ecology and Management,* vol. 130, no. 1-3, pp. 17-26, 2000.

[151] Z. Li, W. A. Kurz, M. J. Apps, and S. J. Beukema, "Belowground biomass dynamics in the Carbon Budget Model of the Canadian Forest Sector: recent improvements and implications for the estimation of NPP and NEP," *Canadian Journal of Forest Research,* vol. 33, no. 1, pp. 126-136, 2003/01/01, 2003.

[152] D. J. Chmura, M. S. Rahman, and M. G. Tjoelker, "Crown structure and biomass allocation patterns modulate aboveground productivity in young loblolly pine and slash pine," *Forest Ecology and Management,* vol. 243, no. 2-3, pp. 219-230, 2007.

[153] D. G. Goodenough, H. Chen, A. Dyk, T. Han, and J. Li, "Multisensor Data Fusion For Aboveground Carbon Estimation," Proc. XXVIIIth General Assembly of the International Union of Radio Science (URSI), New Delhi, India, pp. 1-4, 2005.

[154] R. Quinlan. "Data Mining with Cubist," January 30, 2012; http://www.rulequest.com/cubist-info.html.

[155] E. Ayhan, and O. Kansu, "Analysis of Image Classification Methods for Remote Sensing," *Experimental Techniques,* vol. 36, no. 1, pp. 18-25, 2012.

[156] A. S. Zachor, "Spectral pattern recognition in IR remote sensing," *Applied Optics,* vol. 22, no. 17, pp. 2699, 1983.

[157] P. V. Bolstad, and T. M. Lillesand, "RAPID MAXIMUM-LIKELIHOOD CLASSIFICATION," *Photogrammetric engineering and remote sensing,* vol. 57, no. 1, pp. 67-74, 1991.

[158] J. A. Richards, and X. Jia, *Remote Sensing Digital Image Analysis*, 4 ed., Germany: Springer-Verlag, 2006.

[159] N. Keshava, and J. F. Mustard, "Spectral unmixing," *Signal Processing Magazine, IEEE,* vol. 19, no. 1, pp. 44-57, 2002.

[160] C. Lee, and D. A. Landgrebe, "Analyzing high-dimensional multispectral data," *Geoscience and Remote Sensing, IEEE Transactions on,* vol. 31, no. 4, pp. 792-800, 1993.

[161] B. M. Shahshahani, and D. A. Landgrebe, "The effect of unlabeled samples in reducing the small sample size problem and mitigating the Hughes phenomenon," *Geoscience and Remote Sensing, IEEE Transactions on,* vol. 32, no. 5, pp. 1087-1095, 1994.

[162] C. M. Bishop, "Maximum likelihood," *Pattern Recognition and Machine Learning*, Information Science and Statistics M. Jordan, J. Kleinberg and B. Scholkopf, eds., pp. 432-435, Singapore: Springer, 2006.

[163] F. Melgani, and L. Bruzzone, "Classification of hyperspectral remote sensing images with support vector machines," *Geoscience and Remote Sensing, IEEE Transactions on,* vol. 42, no. 8, pp. 1778-1790, 2004.

[164] C. M. Bishop, "Neural Networks," *Pattern Recognition and Machine Learning,* Information Science and Statistics M. Jordan, J. Kleinberg and B. Scholkopf, eds., pp. 225-290, Singapore: Springer, 2006.

[165] G. F. Hepner, T. Logan, N. Ritter, and N. Bryant, "Artificial neural network classification using a minimal training set - Comparison to conventional supervised classification " *Photogrammetric Engineering and Remote Sensing,* vol. 56, pp. 5, April, 1990.

[166] A. A. Green, M. Berman, P. Switzer, and M. D. Craig, “A transformation for ordering multispectral data in terms of image quality with implications for noise removal,” *Geoscience and Remote Sensing, IEEE Transactions on,* vol. 26, no. 1, pp. 65-74, 1988.

[167] D. G. Goodenough, T. Han, and A. Dyk, “Comparing and validating spectral unmixing algorithms with AVIRIS imagery,” *Canadian Journal of Remote Sensing,* vol. 34, no. S1, pp. S82-S91, June 18, 2008.

[168] L. Kanal, “Patterns in pattern recognition: 1968-1974,” *Information Theory, IEEE Transactions on,* vol. 20, no. 6, pp. 697-722, 1974.

[169] S. J. Raudys, and A. K. Jain, “Small sample size effects in statistical pattern recognition: recommendations for practitioners,” *Pattern Analysis and Machine Intelligence, IEEE Transactions on,* vol. 13, no. 3, pp. 252-264, 1991.

[170] G. Hughes, “On the mean accuracy of statistical pattern recognizers,” *Information Theory, IEEE Transactions on,* vol. 14, no. 1, pp. 55-63, 1968.

[171] L. Weizman, and J. Goldberger, “Classification of hyperspectral remote-sensing images using discriminative linear projections,” *International Journal of Remote Sensing,* vol. 30, no. 21, pp. 5605-5617, Oct. 16, 2009.

[172] C. M. Bishop, "Principal Component Analysis," *Pattern Recognition and Machine Learning,* Information Science and Statistics M. Jordan, J. Kleinberg and B. Scholkopf, eds., pp. 561-570, Singapore: Springer, 2006.

[173] *ENVI Help,* Exelis Visual Information Solutions, Boulder, Colorado, 2010.

[174] D. G. Goodenough, K. O. Niemann, A. Dyk, G. Hobart, P. Gordon, and M. Loisel, "A comparison of forest products from AISA and AVIRIS," Proc. ASTRO, Montreal, Canada, pp. 1-13, 2008.

[175] R. Green, and B. Pavri, "AVIRIS In-Flight Calibration Experiment, Sensitivity Analysis, and Intraflight Stability," Proc. AVIRIS Workshop, Pasadena, CA, p. 15, 2000.

[176] D. G. Goodenough, A. Dyk, T. Han, A. Jazayeri, and J. Li, "Impacts of lossy compression on hyperspectral products for forestry," Proc. IGARSS '04, Anchorage, AK, USA, pp. 465-468, 2004.

[177] D. A. Roberts, M. O. Smith, and J. B. Adams, “Green vegetation, nonphotosynthetic vegetation, and soils in AVIRIS data,” *Remote Sensing of Environment,* vol. 44, no. 2–3, pp. 255-269, 1993.

[178] N. Coops, T. Hilker, M. Wulder, B. St-Onge, G. Newnham, A. Siggins, and J. Trofymow, “Estimating canopy structure of Douglas-fir forest stands from discrete-return LiDAR,” *Trees - Structure and Function,* vol. 21, no. 3, pp. 295-310, 2007.

[179] R. Loos, “Understanding the forest structure: development of tools for identification and delineation of individual trees using LiDAR.,” Thesis, Dept. of Geography, University of Victoria, Victoria, BC, 2009.

[180] D. G. Goodenough, K. O. Niemann, P. Gordon, G. S. Quinn, and F. Visintini, "A Comparison of Forest Classification Between Simulated Sentinel-2 Data, Landsat, and Hyperspectral Data," Proc. Sentinel-2 Preparatory Symposium, Frascati, Italy, pp. 1-5, 2012.

[181] A. K. Mitchell, H. J. Barclay, H. Brix, D. F. W. Pollard, R. Benton, and R. deJong, “Biomass and nutrient element dynamics in Douglas-fir: effects of

thinning and nitrogen fertilization over 18 years," *Canadian Journal of Forest Research*, vol. 26, no. 3, pp. 376-388, Sept. 28, 1995.

[182] V. Avitabile, M. Herold, M. Henry, and C. Schmullius, "Mapping biomass with remote sensing: a comparison of methods for the case study of Uganda," *Carbon Balance and Management,* vol. 6, no. 1, pp. 7, 2011.

[183] C. Dean, S. Roxburgh, and B. G. Mackey, "Forecasting landscape-level carbon sequestration using gridded, spatially adjusted tree growth," *Forest Ecology and Management*, vol. 194, no. 1–3, pp. 109-129, 2004.

[184] UNFCCC, *Decision 1/CP.16, The Cancun Agreement*, United Nations, Cancun, Mexico, 2010.

[185] S. C. Popescu, R. H. Wynne, and J. A. Scrivani, "Fusion of Small-Footprint Lidar and Multispectral Data to Estimate Plot- Level Volume and Biomass in Deciduous and Pine Forests in Virginia, USA," *Forest Science*, vol. 50, no. 4, pp. 551-565, 2004.

[186] R. H. Wynne, "Forest mensuration with remote sensing: A retrospective and a vision for the future," *Southern forest science: past, present, and future*, H. M. Rauscher and K. Johnsen, eds., pp. 109-116, Asheville, NC, USA: Department of Agriculture, Forest Service, Southern Research Station, 2004.

[187] F. Pirotti, "Analysis of full-waveform LiDAR data for forestry applications: a review of investigations and methods," *iForest - Biogeosciences and Forestry*, vol. 4, no. 3, pp. 100-106, Feb. 21, 2011.

[188] A. C. Lee, and R. M. Lucas, "A LiDAR-derived canopy density model for tree stem and crown mapping in Australian forests," *Remote Sensing of Environment*, vol. 111, no. 4, pp. 493-518, 2007.

[189] R. H. Wynne, R. G. Oderwald, G. A. Reams, and J. A. Scrivani, "Optical Remote Sensing for Forest Area Estimation," *Journal of Forestry*, vol. 98, no. 5, pp. 31-36, 2000.

[190] W. Abdalati, H. J. Zwally, R. Bindschadler, B. Csatho, S. L. Farrell, H. A. Fricker, D. Harding, R. Kwok, M. Lefsky, T. Markus, A. Marshak, T. Neumann, S. Palm, B. Schutz, B. Smith, J. Spinhirne, and C. Webb, "The ICESat-2 Laser Altimetry Mission," *Proceedings of the IEEE*, vol. 98, no. 5, pp. 735-751, 2010.

[191] M. McGill, and T. Markus, "ICESat-2 and the importance of space-based laser altimetry measurements," Proc. Lasers and Electro-Optics (CLEO), 2011 Conference on, pp. 1-2, 2011.

[192] N. Faller, and M. Weber, "TerraSAR-X and TanDEM-X: Revolution in spaceborne radar," Proc. IGARSS '07, Barcelona, Spain, pp. 4924-4928, 2007.

[193] S. Gantert, G. Riegler, F. Teufel, O. Lang, L. Petrat, W. Koppe, and J. Herrmann, "TerraSAR-X, TanDEM-X, TerraSAR-X2 and their applications," Proc. Synthetic Aperture Radar (APSAR), 2011 3rd International Asia-Pacific Conference on, pp. 1-4, 2011.

[194] E. Heinemann, and D. V. Eck. "TanDEM-X The Earth in three dimensions," February 15, 2012; http://www.dlr.de/eo/en/desktopdefault.aspx/tabid-5727/10086_read-21046/.

[195] D. Lu, "The potential and challenge of remote sensing-based biomass estimation," *International Journal of Remote Sensing*, vol. 27, no. 7, pp. 1297-1328, April 10, 2006.

[196] Z. Fazakas, M. Nilsson, and H. Olsson, “Regional forest biomass and wood volume estimation using satellite data and ancillary data,” *Agricultural and Forest Meteorology*, vol. 98–99, pp. 417-425, 1999.

[197] B. Medlyn, D. Barrett, J. Landsberg, P. Sands, and R. Clement, “Conversion of canopy intercepted radiation to photosynthate: review of modelling approaches for regional scales,” *Functional Plant Biology*, vol. 30, no. 2, pp. 153-169, 2003.

[198] P. Geladi, and B. R. Kowalski, “Partial least-squares regression: a tutorial,” *Analytica Chimica Acta*, vol. 185, pp. 1-17, 1986.

[199] F. A. Kruse, J. V. Taranik, W. M. Calvin, J. Michaels, E. F. Littlefield, M. Coolbaugh, and B. A. Martini, "Characterization of hydrothermal systems using simulated HyspIRI data," Proc. Aerospace Conference, 2011 IEEE, pp. 1-13, 2011.

[200] S. Samiappan, S. Prasad, L. M. Bruce, and W. Robles, "NASA's upcoming HyspIRI mission: precision vegetation mapping with limited ground truth," Proc. IGARSS '10, Honolulu, HI, USA, pp. 3744-3747, 2010.

[201] S. S. Durbha, R. L. King, and N. H. Younan, "Evaluating Transfer Learning Approaches for Image Information Mining Applications," *Data Mining and machine Learning for Remote Sensing* Proc. IGARSS '11, Vancouver, Canada, p. 4, 2011.

[202] ITT. "History of ITT," April 30, 2012; http://www.itt.com/about/history/.

[203] D. G. Goodenough, K. O. Niemann, G. S. Quinn, A. Gross, and K. Lang, "Environmental controls on forest chemistry: evaluating and refining foliar chemistry from imaging spectroscopy," Proc. IGARSS '10, Honolulu, HI, USA, pp. 3764-3767, 2010.

[204] J. L. Ware, "Using ArcGIS for Geospatial Analysis with Multi/Hyperspectral Data," Defense Geospatial-Intelligence School, National Geospatial-Intelligence College, 2010, p. 9.

[205] P. Bernier, P. J. Hanson, and P. S. Curtis, "Measuring Litterfall and Branchfall Field Measurements for Forest Carbon Monitoring," C. M. Hoover, ed., pp. 91-101: Springer Netherlands, 2008.

[206] L. Benoit, *Canada's Forest Industry: Recognizing the Challenges and Opportunities*, Canada Parliament House of Commons, Ottawa, ON, CAN, 2008.

[207] "GNU General Public License," February 1, 2012; http://www.gnu.org/copyleft/gpl.html.

Appendix A: Studies in the Greater Victoria Watershed District

Studies in the Greater Victoria Watershed District (GVWD): 1992 – 2000.

VWS is Victoria Watershed South and VWN is Victoria Watershed North in [124]. Three plots from VWS were re-examined in [118] in 1999 and 2000.

Table 7: Tree species measurements in the GVWD from Getzin et al., 2006.

Table 3. Stand structure and composition of the chronosequence. ⟨⟩ = mean, NN = nearest neighbor; S = Pielou's segregation index.

Plot/ species	⟨NN⟩ distance (m) in plot	Number of stems	% stems	% mortality per species	⟨DBH⟩ (cm) per species	% with DBH of 0.1–10 cm	% mortality within DBH class of 0.1–10 cm	Pielou's S
Immature	0.63							
Douglas-fir		885	49.9	56.8	8.2	74.0	60.8	0.296
Western hemlock		750	42.3	71.7	5.4	86.6	75.6	0.318
Mature	0.82							
Douglas-fir		875	28.9	50.1	33.7	6.5	95.5	0.193
Western hemlock		381	12.6	19.7	10.0	65.7	23.9	0.398
Western redcedar		720	23.8	5.3	7.8	80.5	5.1	0.567
Old-growth	0.93							
Douglas-fir		244	16.7	36.5	52.2	15.3	44.4	0.350
Western hemlock		1061	72.6	40.3	11.0	59.0	57.3	0.485
Western redcedar		130	8.9	24.6	19.9	36.0	21.9	0.600

Table 8: Attributes of the different study areas from Trofymow et al., 1997. Of interest are VWS and VWN.

Table 5. Environmental characteristics summary by chronosequence

Attribute	Location							
	VWS	VWN	KOK	NAN	REN	RGC	NIT	KLA
BEC zone	CWHxm1	CWHxm2, xm1	CWHxm2	CWHxm1	CWHvm1	CWHvm1	CWHvm1	CWHvm1
Elevation (m) (mean: range)	303: 240 – 390	382: 260 – 465	631: 590 – 710	440: 430 – 460	206: 130 – 320	172: 80 – 300	227: 85 – 325	155: 120 – 230
Slope (%) (mean: range)	26: 11 – 40	21: 5 – 40	20: 15 – 35	21: 20 – 25	38: 25 – 45	47: 10 – 100	31: 22 – 45	23: 15 – 35
Aspect	NE (NW)	W, N, NE	S	S, SE, SW	W – N	N (E)	SW – W	NW (SE)
Slope position	upper, middle, lower	middle	middle	middle (upper)	middle	middle (level)	middle (lower)	middle, lower
Exposure	n/a	n/a	wind	n/a (wind)	wind (n/a)	wind	wind (n/a)	wind
Surface shape	straight, (concave)	straight, (convex, concave)	straight, (convex)	straight, (concave)	straight, (convex, concave)	straight, (convex)	straight, concave	convex, (straight, concave)
Hygrotope	mesic, subhygric	mesotrophic	mesic (subxeric, submesic)	submesic (subxeric)	mesic (subhygric)	mesic (subhygric)	mesic (submesic)	submesic – subhygric
Trophotope	mesotrophic, permesotrophic	mesotrophic	mesotrophic (submesotrophic)	submesotrophic	mesotrophic (submesotrophic)	mesotrophic – permesotrophic	submesotrophic – permesotrophic	mesotrophic
Terrain	gravelly sandy inactive morainal, (fluvial)	gravelly (fragmental) sandy inactive morainal, (weathered bedrock)	gravelly silty, inactive colluvial	gravelly silty, gravelly sandy, inactive morainal	sandy fragmental and silty fragmental inactive colluvial	silty fragmental inactive colluvial	gravelly silty (sandy) inactive colluvial	gravelly sandy, inactive colluvial
Soil	Orthic (Duric) Dystric Brunisols	Orthic Humo-Ferric Podzols and Duric Dystric Brunisols	Orthic Humo-Ferric Podzols	Duric Humo-Ferric Podzols	Orthic (gleyed) Humo-Ferric Podzols	Orthic Humo-Ferric Podzols (Duric Ferro-Humic Podzols)	Orthic Humo-Ferric Podzols	Orthic Humo-Ferric and Ferro-Humic Podzols
Family particle size	fine-silty, coarse-loamy	variable	fine-silty, loamy	fine-silty, loamy	variable	fine-silty (silty), loamy	fine-silty, loamy	fine-silty (silty), loamy
Rooting depth (cm) (mean: range)	37: 23 – 46	65: 45 – 78	47: 40 – 50	52: 30 – 60	38: 25 – 50	57: 50 – 60	40: 10 – 75	45: 40 – 60
Root restrict depth (cm) (mean: range)	63: 44 – 83	71: 45 – 95		35	61: 25 – 100	60	30: 26 – 35	130
Soil drainage	well (moderately well)	well	rapid	well	well (poor)	well	rapid	moderately well (well)
Humus form[a]	mull-like moders (conifero- typical moders, conifero zoomulls)	Humi–fibrimors	Hemihumimors	Hemihumimors	Orthihemimors	Orthihemimors, Moders	Hemihumimors, (Moders)	Orthi(ligno)humi(hemi)mors

[a]from Bernier (1968) for VWS and VWN; otherwise from Klinka (1981).

NOTE: Where a cell contains more than one attribute, the most common attribute (if there is one) is listed first. Attributes separated by commas are approximately equal in frequency among the plots in the group; those enclosed in parentheses are from a single plot only.

Table 9: Tree measurements made in 1994-5 and published by Trofymow et al., 1997.

Table V-1. Mensuration summary (with standard error) for Victoria Watershed South (VWS) plots

Plot	Form	Spp.	n	Mean density (#/ha)	Basal area (m^2/ha)		Mean DBH (cm)		Mean height (m)		Maximum height (m)	Mean Age BH (years)	
Living trees													
01 (1)	tree	all	34	1443	0.3	(< 0.1)	1.4	(0.2)	0.9	(0.1)	3.7	4	
02 (2)	tree	FD	24	1019	22.7	(3.4)	13.2	(2.2)	11.9	(1.1)	22.6	18	(1)
		HW	29	1231	7.7	(1.4)	6.6	(1.1)	7.6	(0.8)	18.2		
			53	**2250**	**30.4**								
05 (3a)	tree	CW	7	99	4.8	(0.4)	23.1	(3.6)	16.9	(2.5)	28.3	89	(2)
		DR	1	14	1.5		36.2		37.4		37.4		
		FD	39	552	81.8	(9.1)	39.0	(3.1)	34.2	(1.5)	50.2		
		HW	1	14	0.6		22.5		20.5		20.5		
		PW	1	14	< 0.1		6.5		8.0		8.0		
			49	**693**	**88.7**								
06 (4)	tree	CW	4	42	2.9	(0.1)	26.9	(7.4)	16.7	(4.8)	27.6	235	(15)
		DR	1	11	0.9		32.5		16.9		16.9		
		FD	14	149	73.6	(6.4)	76.8	(5.6)	47.5	(2.0)	58.4		
		HW	32	340	5.7	(0.8)	12.4	(1.4)	10.4	(1.3)	34.0		
			51	**542**	**83.1**								
Stumps and snags													
01 (1)	stump	CW	30	318	45.9	(5.1)	38.1	(3.6)	0.4	(< 0.1)	0.7		
		FD	3	32	13.2		71.7	(9.0)	0.6	(0.3)	1.2		
			33	**350**	**59.1**								
02 (2)	stump	FD	3	127	67.1	(2.4)	81.7	(4.4)	0.7	(0.1)	0.8		
	snag	FD	14	594	0.4		2.7	(0.2)	3.9	(0.3)	5.8		
		HW	9	382	0.2		2.6	(0.4)	3.9	(0.5)	6.5		
			26	**1103**	**67.7**								
05 (3a)	snag	DR	4	57	3.9	(1.0)	29.3	(1.5)	15.5	(6.7)	31.2		
		FD	17	693	21.1	(6.4)	18.8	(2.7)	9.8	(2.0)	27.3		
			21	**750**	**25.0**								
06 (4)	snag	DR	1	11	0.6		26.6		4.9		4.9		
		FD	2	21	5.9		55.1	(22.6)	25.0	(22.6)	47.6		
		HW	33	467	8.1	(1.6)	7.9	(1.1)	4.4	(0.5)	10.6		
			36	**499**	**14.6**								

Notes:
Living tree data are derived from all living stems in regeneration plots and from all stems ≥ 3.0 m in all other plots.
Data for snags and stumps are derived from all snag and stump data for all plots.
Bold numbers indicate plot totals of living and dead materials.
Standard error for basal area / hectare refers to variation between mensuration subplots; standard errors for diameter and height refer to variation within plots. Missing values for standard error imply that either the material was observed in only one mensuration subplot, or that only one instance of the material was observed.
Plot numbers in brackets indicate the original chronosequence plot number in the plot location and establishment report (Blackwell 1992a).
CW = western redcedar; DR = red alder; FD = Douglas-fir; HW = western hemlock

Table 10: Tree measurements made in 1993-4 and published by Trofymow et al., 1997.

Table V-2. Mensuration summary (with standard error) for Victoria Watershed North (VWN) plots

Plot	Form	Spp.	n	Mean density (#/ha)	Basal area (m^2/ha)		Mean DBH (cm)		Mean height (m)		Maximum height (m)	Mean Age BH (years)	
Living trees													
11 (1)	tree	all	24	1019	0.5	(< 0.1)	2.2	(0.3)	1.2	(0.1)	2.6	6	
12 (2)	tree	FD	49	2080	48.6	(0.6)	16.4	(0.8)	18.2	(0.5)	23.5	32	(1)
13 (3)	tree	CW	3	64	1.6		15.2	(6.7)	9.2	(3.5)	16.0		
		FD	60	1273	65.1	(7.1)	20.8	(1.9)	19.1	(1.5)	37.6	83	(2)
			63	**1337**	**66.7**								
15 (4)	tree	CW	8	117	5.5	(2.6)	24.3	(5.7)	15.2	(3.4)	26.6	306	(3)
		FD	34	361	81.4	(1.2)	51.5	(2.6)	32.0	(1.1)	47.4		
		HW	16	233	3.1	(0.9)	10.9	(2.8)	7.7	(1.7)	29.0		
			58	**711**	**90.0**								
Stumps and snags													
11 (1)	stump	CW	5	53	15.1	(4.1)	53.2	(14.1)	0.4	(0.1)	0.7		
		FD	24	255	78.1	(2.0)	60.2	(3.5)	0.4	(< 0.1)	0.8		
		HW	3	32	0.5	(< 0.1)	13.3	(1.8)	0.3	(< 0.1)	0.3		
			32	**340**	**93.7**								
12 (12)	stump	FD	3	127	15.3		37.3	(8.4)	0.6	(0.1)	0.7		
	snag	FD	12	509	2.1	(0.3)	6.5	(1.0)	8.8	(1.3)	15.2		
			15	**636**	**17.4**								
13 (3)	stump	FD	1	21	7.0		65.0		0.5		0.5		
	snag	FD	32	679	3.1	(0.6)	6.3	(0.7)	6.7	(0.8)	16.4		
			33	**700**	**10.1**								
15 (4)	snag	CW	2	21	0.7		19.8	(1.8)	12.9	(0.5)	13.4		
		FD	10	297	14.7	(1.0)	24.3	(3.3)	4.5	(1.7)	18.8		
		HW	2	85	< 0.1		2.2	(0.1)	1.9	(0.7)	2.6		
			14	**403**	**15.4**								

Notes:
Living tree data are derived from all living stems in regeneration plots, from all stems ≥ 3.0 m in all other plots.
Data for snags and stumps are derived from all snag and stump data for all plots.
Bold numbers indicate plot totals of living and dead materials.
Standard error for basal area / hectare refers to variation between mensuration subplots; standard errors for diameter and height refer to variation within plots. Missing values for standard error imply that either the material was observed in only one mensuration subplot, or that only one instance of the material was observed. Plot numbers in brackets indicate the original chronosequence plot number in the plot location and establishment report (Blackwell 1992a).
FD = Douglas-fir; HW = western hemlock; DR = red alder; PW = western white pine; CW = western redcedar

Appendix B: Confusion Matrices from Maximum Likelihood Classification

Table 11: Confusion matrix for non-aggregated classes in the D4S2 area from a maximum likelihood classification run on AVIRIS hyperspectral data. RA is Red Alder, PL is Lodgepole Pine, and Cuts are recent clearcuts. The overall accuracy is 63.9%.

									Douglas-fir					
									Dense		Open		Sparse	
	Class\Truth	Water	Swamp	Hemlock	Land	Cuts	Shrub	RA	PL	60yr	110yr	40yr	200+yr	40yr	Total
	Water	99.99	0.12	0.00	0.00	0.00	0.04	0.27	0.00	0.00	0.00	0.00	0.00	0.00	9.73
	Swamp	0.00	98.58	0.07	0.78	0.00	0.07	0.67	0.36	0.16	0.00	0.21	0.02	1.10	6.37
	Hemlock	0.00	0.00	42.79	0.00	0.00	16.95	2.89	7.77	0.01	5.55	10.07	8.09	0.18	5.54
	Land	0.00	0.00	0.00	89.65	0.00	0.02	0.00	0.00	0.01	0.00	0.08	0.00	0.01	0.17
	Cuts	0.00	0.00	0.00	0.00	99.68	0.00	0.00	0.13	0.01	0.00	0.29	0.00	0.00	3.08
	Shrub	0.00	0.00	0.00	0.00	0.00	60.58	0.00	0.08	31.00	0.00	0.41	0.20	1.34	8.81
	Red Alder	0.00	1.17	1.87	7.03	0.00	11.45	95.19	0.00	0.22	0.00	4.67	0.17	0.56	3.74
	PL	0.00	0.00	2.53	0.00	0.00	0.00	0.00	60.07	0.00	1.30	14.86	2.39	0.00	6.96
	Dense 60	0.00	0.07	0.03	0.00	0.00	0.07	0.22	0.00	61.51	0.00	7.32	0.00	53.25	21.04
	Dense 110	0.00	0.00	34.32	0.00	0.00	0.00	0.00	12.44	0.00	88.33	2.15	31.76	0.00	9.90
	Open 40	0.01	0.00	1.29	1.56	0.32	7.97	0.48	10.35	0.09	0.79	46.02	3.10	3.10	8.90
	Open 200+	0.00	0.00	17.07	0.00	0.00	1.60	0.06	8.62	0.00	4.03	10.50	52.99	0.01	7.89
	Sparse 40	0.00	0.06	0.03	0.98	0.00	1.25	0.22	0.18	6.98	0.00	3.42	1.28	40.47	7.87
	Total	100.00	100.00	100.00	100.00	100.00	100.00	100.00	100.00	100.00	100.00	100.00	100.00	100.00	100.00

Douglas-fir (age in years)

Table 12: Non-aggregated producer accuracy, user accuracy, commission error and omission error for maximum likelihood classification of AVIRIS data of D4S2.

Class\Error(%)	Prod. Acc.	User Acc.	Commision	Omission
Water	99.99	99.84	0.16	0.01
Swamp	98.58	95.76	4.24	1.42
Hemlock	42.79	30.74	69.26	57.21
Exposed Land	89.65	89.82	10.18	10.35
Recent Cuts	99.68	98.17	1.83	0.32
Shrub	60.58	26.28	73.72	39.42
Red Alder	95.19	61.35	38.65	4.81
Lodgepole Pine	60.07	62.06	37.94	39.93
DF Dense 60yr	61.51	58.63	41.37	38.49
DF Dense 110yr	88.33	45.30	54.70	11.67
DF Open 40yr	46.02	78.65	21.35	53.98
DF Open 200+	52.99	59.87	40.13	47.01
DF Sparse 40yr	40.47	73.22	26.78	59.53

Table 13: After aggregation producer accuracy, user accuracy, commission error and omission error for a maximum likelihood classification of AVIRIS data of D4S2.

Class\Error(%)	Prod. Acc.	User Acc.	Commision	Omission
Water	99.99	99.84	0.16	0.01
Swamp	98.58	95.76	4.24	1.42
Hemlock	42.79	30.74	69.26	57.21
Exposed Land	89.65	89.82	10.18	10.35
Recent Cuts	99.68	98.17	1.83	0.32
Shrub	60.58	26.28	73.72	39.42
Red Alder	95.19	61.35	38.65	4.81
Lodgpole Pine	60.07	62.06	37.94	39.93
Douglas-fir	79.96	91.31	8.69	20.04

Below is a confusion matrix for the classification of AVIRIS data over D4S2 with percent accuracies per class (aggregated) and an overall accuracy of 80.4%. It is a duplicate of Table 4.

Class\Truth	Water	Swamp	Hemlock	Land	Cuts	Shrub	Red Alder	Pine	Douglas-fir	Total
Water	99.99	0.12	0.00	0.00	0.00	0.04	0.27	0.00	0.00	9.73
Swamp	0.00	98.58	0.07	0.78	0.00	0.07	0.67	0.36	0.35	6.37
Hemlock	0.00	0.00	42.79	0.00	0.00	16.95	2.89	7.77	4.04	5.54
Exposed Land	0.00	0.00	0.00	89.65	0.00	0.02	0.00	0.00	0.03	0.17
Recent Cuts	0.00	0.00	0.00	0.00	99.68	0.00	0.00	0.13	0.07	3.08
Shrub	0.00	0.00	0.00	0.00	0.00	60.58	0.00	0.08	10.22	8.81
Red Alder	0.00	1.17	1.87	7.03	0.00	11.45	95.19	0.00	1.34	3.74
Lodgepole Pine	0.00	0.00	2.53	0.00	0.00	0.00	0.00	60.07	4.00	6.96
Douglas-fir	0.01	0.13	52.74	2.54	0.32	10.89	0.98	31.59	79.96	55.60
Total	100.00	100.00	100.00	100.00	100.00	100.00	100.00	100.00	100.00	100.00

Appendix C: Data Flow Diagrams

The following data flow diagrams give an overview of the aboveground carbon estimation process, from data acquisition through to the output carbon map. It is important that the users of the automated system understand the types of input data which are expected. Extra notes on the process diagrams will be included, referring to the numbered processes P #, and data stores D #. Some processes have been expanded upon in their own diagrams. The arrows connect the processes in order and show from where the data is coming and in which processes it is used.

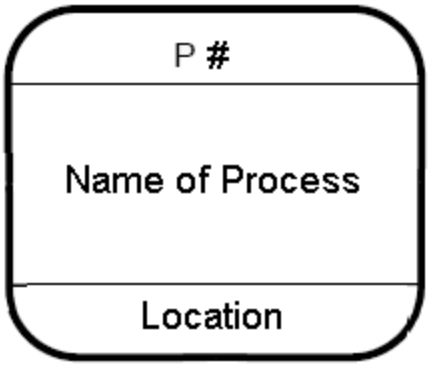

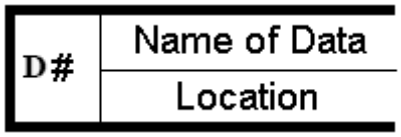

The processes P 4.4, P 4.5 and P 4.6, demonstrate that some classification techniques, such as maximum likelihood, will require feature extraction first while others may not. In P 4.7, the user must decide on a lower bound for classification accuracy. If the classification results are not accurate enough, features may need to be added or subtracted, another classifier type may be chosen, or the data could be masked to remove shadow or to isolate the difficult classes. Such masking may be the result of a clustering algorithm or another classification.

Carbon Map Data Flow

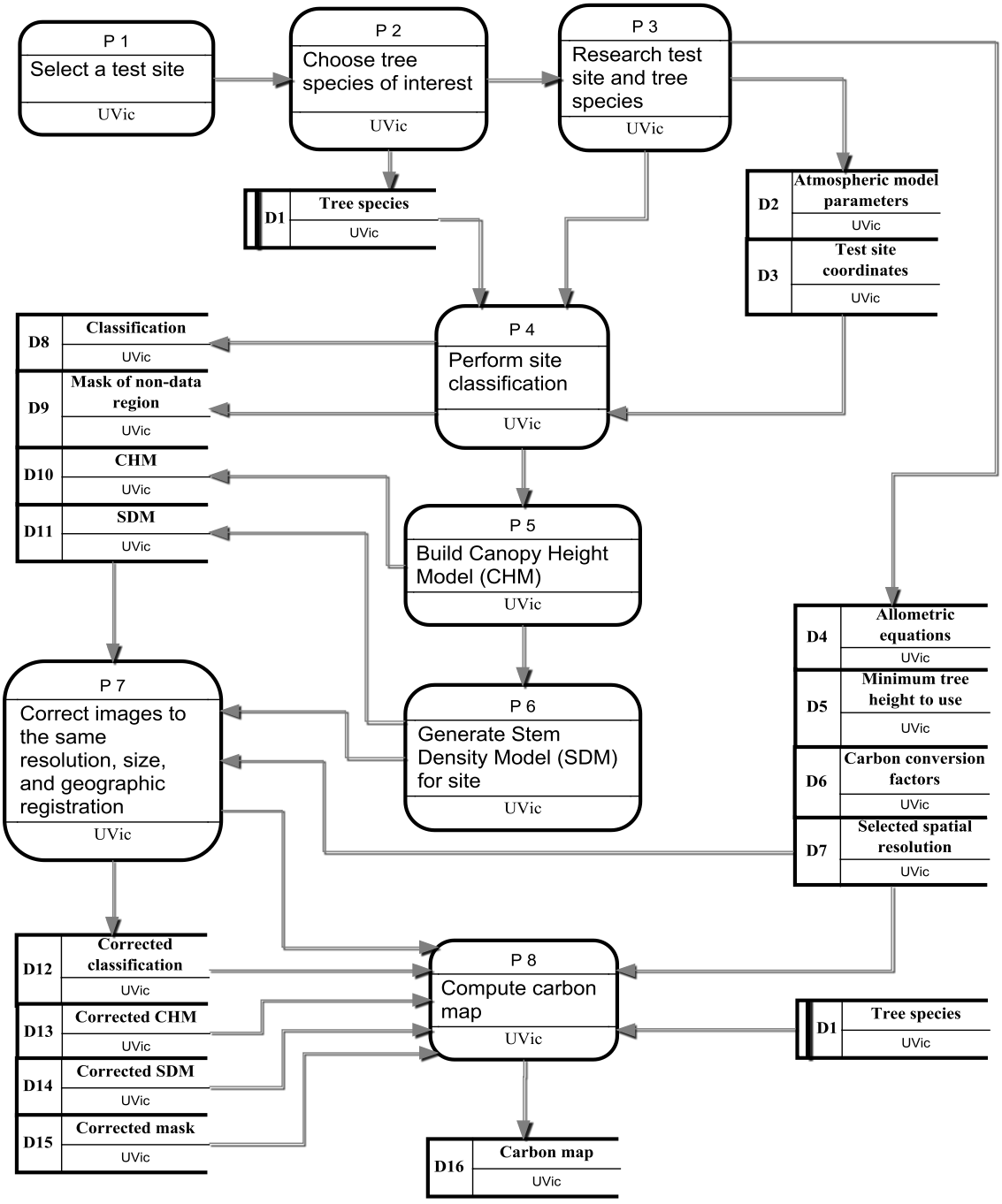

P4 Acquire Site Classification

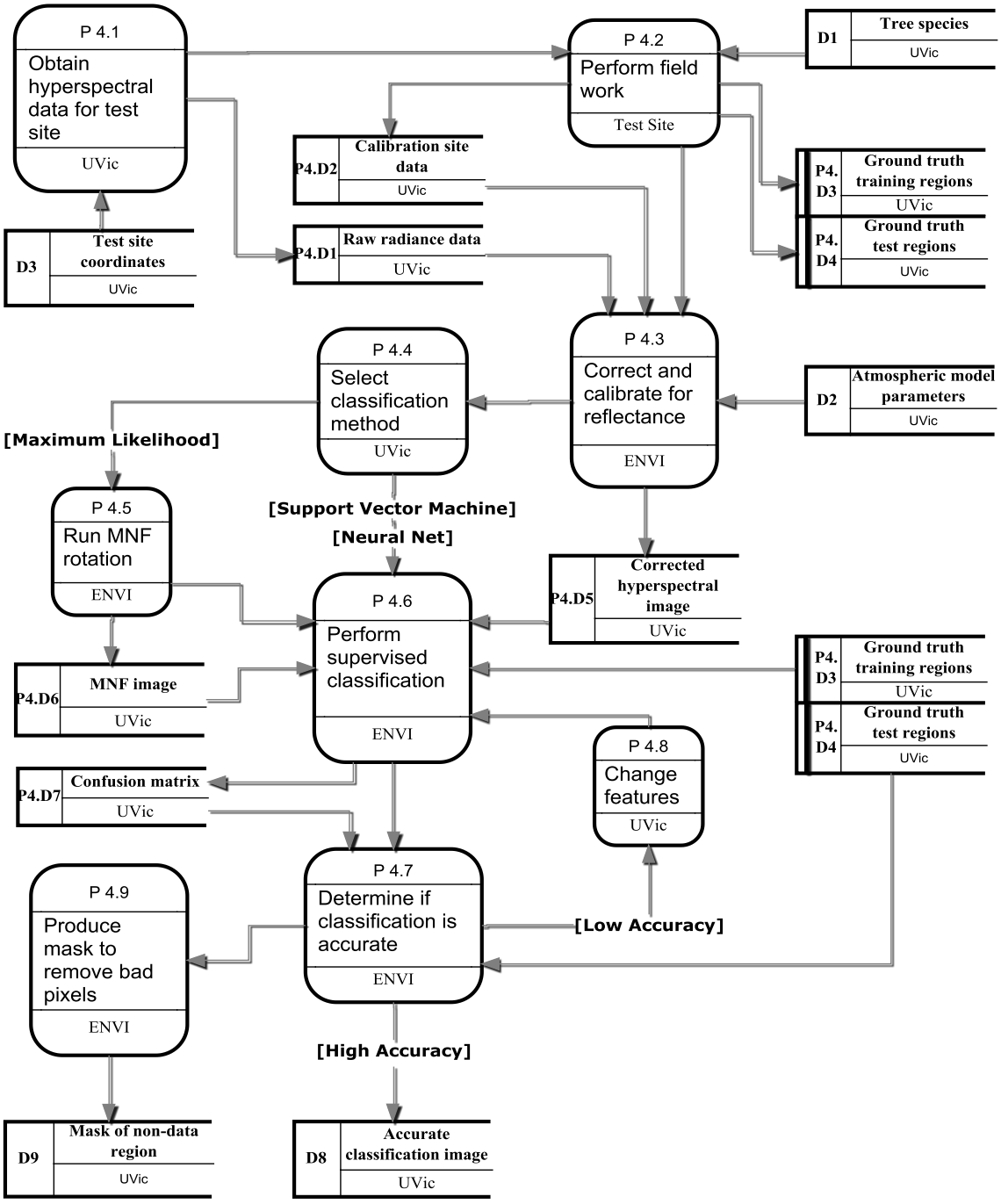

P5 Acquire Canopy Height Model (CHM)

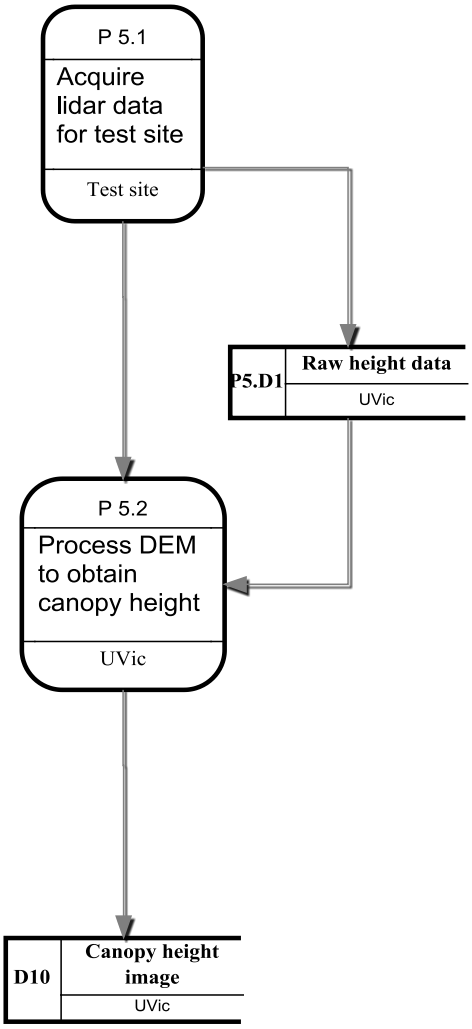

P6 Acquire Stem Density Model (SDM)

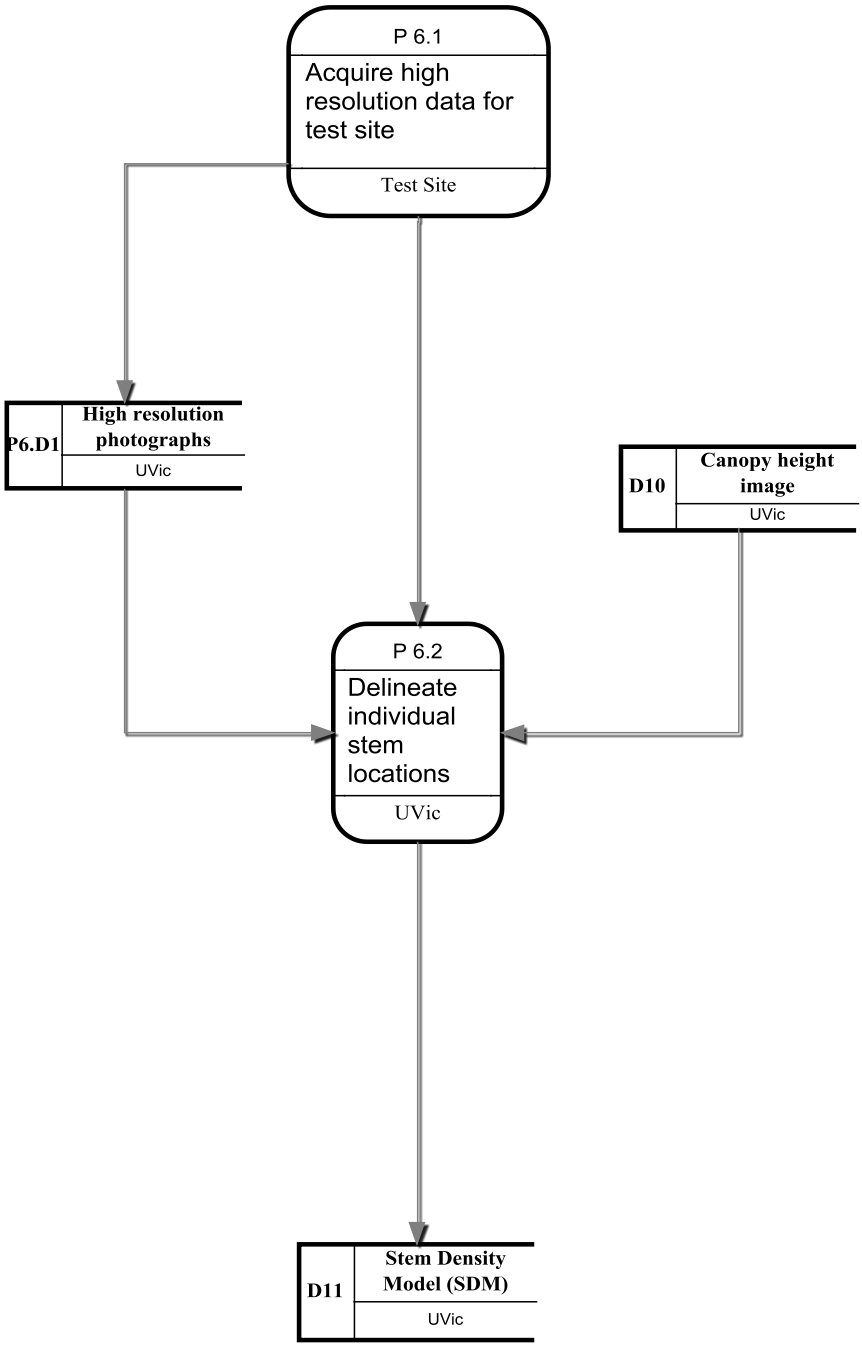

P7 Correct Images to the Same Resolution, Size, and Geographic Registration

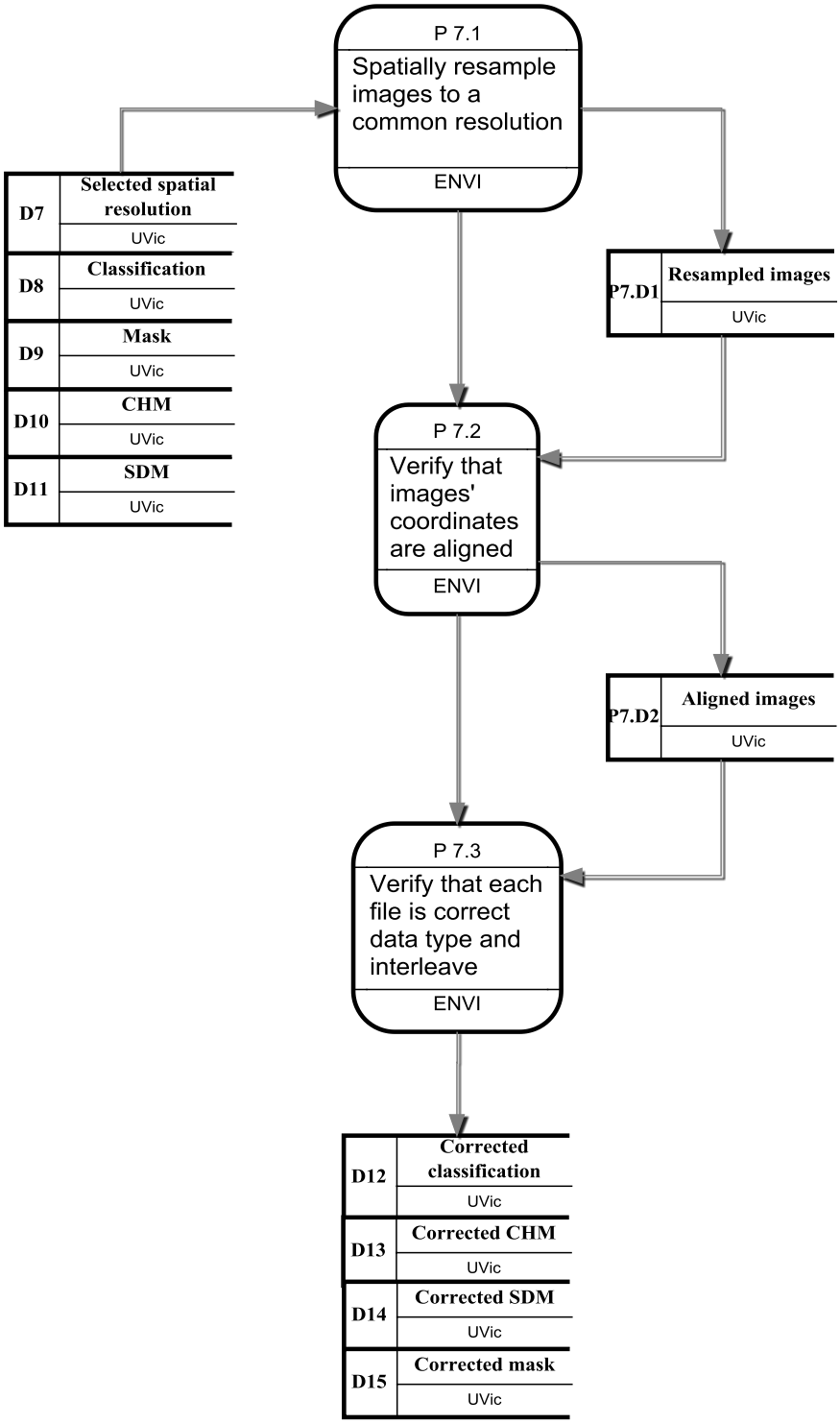

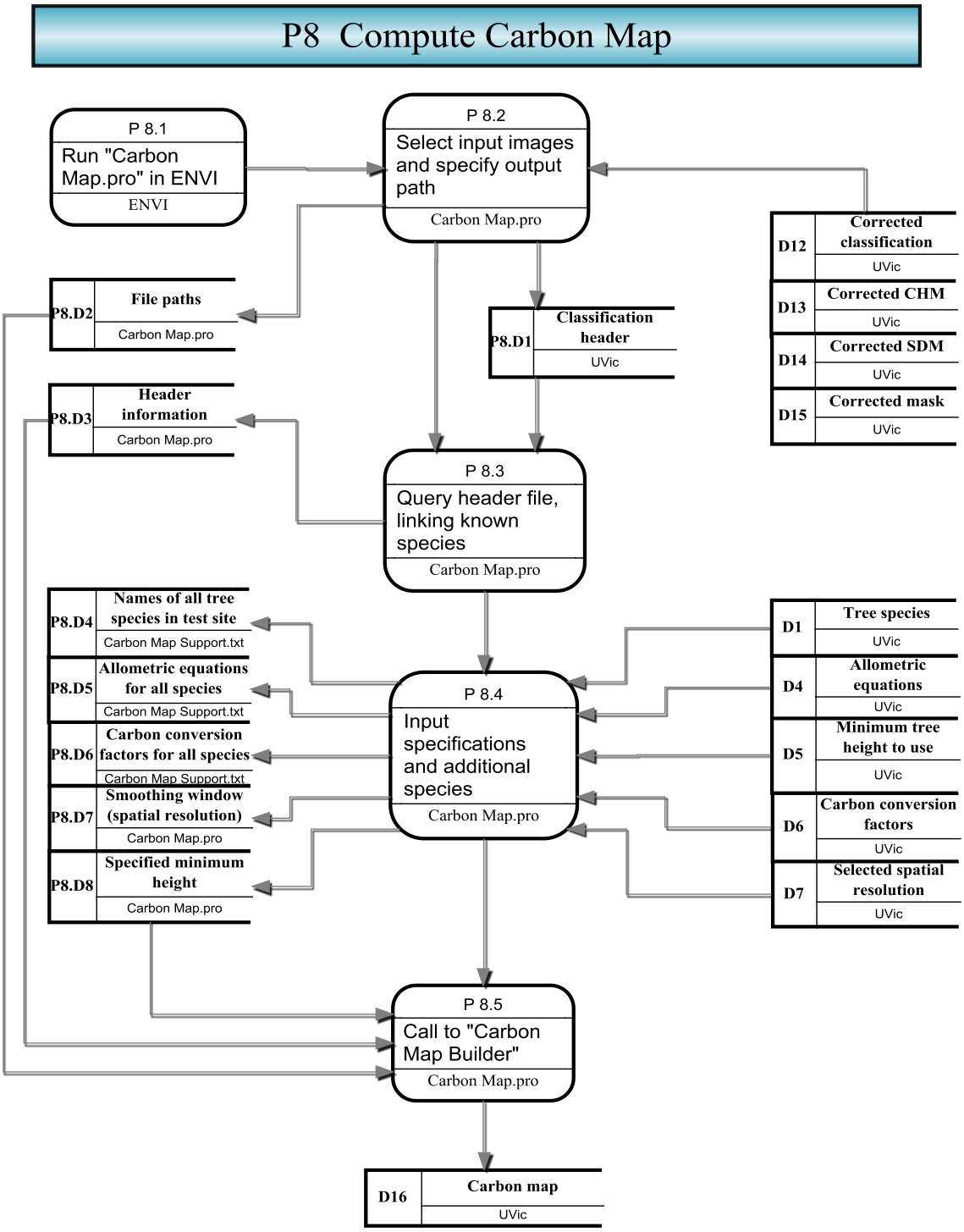
P8 Compute Carbon Map
P 8.1
Run "Carbon Map.pro" in ENVI
ENVI
P 8.2
Select input images and specify output path
Carbon Map.pro
P8.D2
File paths
Carbon Map.pro
P8.D1
Classification header
UVic
D12
Corrected classification
UVic
D13
Corrected CHM
UVic
D14
Corrected SDM
UVic
D15
Corrected mask
UVic
P8.D3
Header information
Carbon Map.pro
P 8.3
Query header file, linking known species
Carbon Map.pro
P8.D4
Names of all tree species in test site
Carbon Map Support.txt
P8.D5
Allometric equations for all species
Carbon Map Support.txt
P8.D6
Carbon conversion factors for all species
Carbon Map Support.txt
P8.D7
Smoothing window (spatial resolution)
Carbon Map.pro
P8.D8
Specified minimum height
Carbon Map.pro
P 8.4
Input specifications and additional species
Carbon Map.pro
D1
Tree species
UVic
D4
Allometric equations
UVic
D5
Minimum tree height to use
UVic
D6
Carbon conversion factors
UVic
D7
Selected spatial resolution
UVic
P 8.5
Call to "Carbon Map Builder"
Carbon Map.pro
D16
Carbon map
UVic

P8.5 Call to Carbon Map Builder

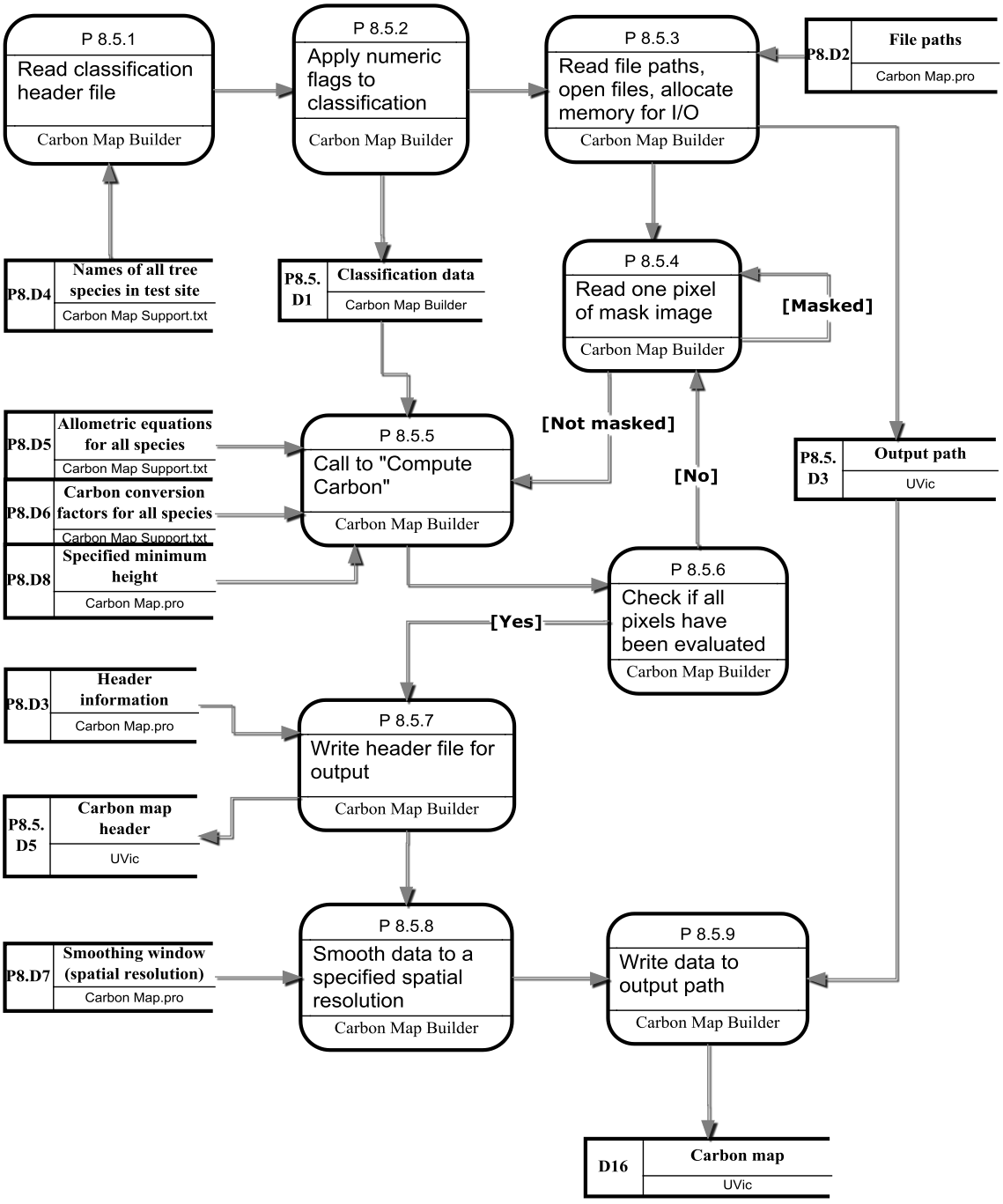

P8.5.5 Call to Compute Carbon